Geology of central Libya Montes, Mars: Aqueous alteration history from mineralogical and morphological mapping

D. Tirsch[1*], J.L. Bishop[2,3], ~~J. Voigt[1]~~, L.L. Tornabene[4], G. Erkeling[5], and R. Jaumann[1,6]

[1] Institute of Planetary Research, German Aerospace Center (DLR), Rutherfordstrasse 2, 12489 Berlin, Germany (*corresponding author: Daniela.Tirsch@dlr.de, +49-30-67055448).

[2] Carl Sagan Center, The SETI Institute, Mountain View, CA 94043, USA.

[3] Exobiology Branch, NASA-Ames Research Center, Moffett Field, CA 94035, USA.

[4] University of Western Ontario, London, ON, Canada.

[5] German National Library of Science and Technology (TIB), Leibniz Information Centre for Science and Technology, Hannover, Germany.

[6] Institute of Geological Sciences, Freie Universitaet Berlin, 12249 Berlin, Germany.

Abstract

We analyze the emplacement chronology and aqueous alteration history of distinctive mineral assemblages and related geomorphic units near Hashir and Bradbury impact craters located within the Libya Montes, which are part of the southern rim of the Isidis Basin on Mars. We derive our results from a spectro-morphological mapping project that combines spectral detections from CRISM near-infrared imagery with geomorphology and topography from HRSC, CTX, and HiRISE imagery. Through this combination of data sets, we were able to use the morphology associated with specific mineral detections to extrapolate the possible extent of the units hosting these compositions. We characterize multiple units consistent with formation through volcanic, impact, hydrothermal, lacustrine and evaporative processes. Altered pyroxene-bearing basement rocks are unconformably overlain by an olivine-rich unit, which is in turn covered by a pyroxene-bearing capping unit. Aqueously altered outcrops identified here include nontronite, saponite, beidellite, opal, and dolomite. The diversity of mineral assemblages suggests that the nature of aqueous alteration at Libya Montes varied in space and time. This mineralogy together with geologic features shows a transition from Noachian aged impact-induced hydrothermal alteration and the alteration of Noachian bedrock by neutral to slightly basic waters via Hesperian aged volcanic emplacements and evaporative processes in lacustrine environments followed by Amazonian resurfacing in the form of aeolian erosion.

Keywords

Mars, geology, reflectance spectroscopy, geomorphological mapping, remote sensing, aqueous alteration, hydrothermal alteration

1. **Introduction**

The Libya Montes region, located at the southern rim of the Isidis impact basin, is an excellent example of the diverse geological processes that have shaped this part of the Martian surface over time (e.g., Crumpler and Tanaka, 2003; Jaumann et al., 2010). Evidence of fluvial, lacustrine, aeolian, volcanic, impact/basin-forming events and hydrothermal processes, which span most of the geologic time on Mars, can be found in close association with one another. These landforms at Libya Montes are related to both relatively unaltered materials and aqueously altered sedimentary deposits and local rocks. Libya Montes provides a geologically diverse setting with multiple spectral observations useful for deciphering the complex geological and aqueous alteration history of this region of Mars with high value for contributing to the global picture of the evolution and climatic history of the planet.

Previous studies have documented extensive modification of the Libya Montes region and its wider surroundings by impact, volcanic, tectonic, aeolian and fluvial processes (Greeley and Guest, 1987; Crumpler and Tanaka, 2003; Erkeling et al., 2010b; Jaumann et al., 2010). To the north, the Libya Montes region hosts dense valley networks that modified terrain dating from the Noachian period (Crumpler and Tanaka, 2003; Mustard et al., 2007; Tornabene et al., 2008; Erkeling et al., 2010b; Jaumann et al., 2010; Bishop et al., 2013b). Ivanov et al. (2012) describe a transition from an impact-dominated period (~3.8 Ga) to an episode dominated by volcanic and fluvial/glacial activities (~3.8-2.8 Ga). More recently, Ivanov et al. (2014) suggested that mafic surface units across the southern Isidis region may have been exposed by mud volcanism. Surface exposures of olivine and pyroxene at Libya Montes resemble those of Nili Fossae to the northwest of Isidis Basin (c.f., Tornabene et al., 2008; Mustard et al., 2009). The olivine-rich unit has been interpreted as an impact melt from Isidis (Mustard et al., 2007), as a nearly global layer from a mega-impact event (Edwards and Christensen, 2011), as volcanic by-products from Syrtis Major (Tornabene et al., 2008) or as more ancient basaltic lavas not from the Syrtis Major region (Hoefen et al., 2003; Hamilton and Christensen, 2005).

Spectral determinations of surface composition are generally limited to the west/southwest regions as dust cover is shown to increase towards the north, east and southeast (see dashed line Figure 1), where it obscures the underlying spectral properties of the surface (Murphy et al., 2007; Tornabene et al., 2008). In this study, we focus on a region where thinner dust coverage allows for spectral analyses. It is located between 2.3-3.8° N latitude and 84.3-86.3° E longitude and comprises the impact craters Hashir and Dulovo in the western part as well as Bradbury crater in the eastern part of this region. We use descriptions such as "*Hashir region*" and "*Bradbury region*" hereafter to distinguish between the western and eastern parts of the central Libya Montes study region (Figure 1). We use "central" as a descriptive name for the whole study region because the site comprises the mouth region of the *Middle Libya Montes Valley System* (named by Crumpler and Tanaka (2003)) which is located between the *Western* and the *Eastern Valley Systems* (see Figure 1 left; c.f., Jaumann et al., 2010).

➔ Figure 1 **(outline of study region) about here**

1.1. **Context from Previous Studies**

Bishop et al. (2013b), presented previously a regional scale map of the wider Libya Montes and South Isidis region with larger-scale geologic units appropriate for this mapping project. The units coincide in parts with the regional morphologic units used in our work. As a result of this study, next to the regionally common olivine- and pyroxene-bearing units, different species of Fe/Mg-rich phyllosilicates were identified at different sites at the Hashir region and in an area a little further to the west (Bishop et al. (2013b). They were interpreted to represent parts of altered ancient bedrock excavated by erosion and impact events. The Al-smectite beidellite was detected at two sites at the Hashir region and suggested to have resulted from hydrothermal alteration of diagenetic processes. Also carbonates were found north of Hashir crater, always associated with olivine and Fe/Mg-smectites. The Bradbury crater region was also studied earlier and was the focus of Al-smectite detections (Bishop et al., 2011; Erkeling et al., 2012). Bishop et al. (2011) identified these bright outcrops as beidellite due to the Al-OH band at 2.19 μm together with water bands near 1.4 and 1.9 μm, compared with related bands for Al-OH in montmorillonite at 2.21 μm and Si-OH in hydrated silica/opal at 2.21 μm that are found elsewhere on Mars (e.g., Mustard et al., 2008). Erkeling et al. (2012) characterized the fan-shaped deposits (interpreted to be a delta) and dated the action of fluvial and lacustrine processes in the region. Later, the authors refined the analyses of the three fan-shaped deposits in Bradbury crater and reconstructed different stages of depositional events occurring up to (~<3.6 Ga) (Erkeling et al., 2012; Erkeling et al., 2016). They also reported on new detections of Fe/Mg-smectites at Bradbury crater and suggested evidence for the long-term availability of liquid water and aqueous alteration.

1.2. **The Aim of this Study**

In addition to these previous studies, we will refine, combine and compare the geological setting of the Hashir and the Bradbury regions in order to provide a comprehensive view of the entire central Libya Montes region. Our investigation is intended to complement previous studies by bringing distinct landforms and their deposits into context with each other and with their associated spectral units. By doing this and by combination with the results of the previous studies, we can deduce an overall time line of emplacement events and alteration history for the Libya Montes region. Hence, we begin with a more detailed morphologic and spectral mapping investigation of small-scale features in order to shed light on the local stratigraphy of the aqueous minerals and their interrelationships with their geologic context.

We lead the current geological interpretations from a mineralogical perspective identifying distinct mineralogical units in spectral parameter products. We have verified out extracted spectra through comparison with lab-measured mineral spectra, to understand and contextualize our specific mineralogical observations. In addition we explore the morphology from high-resolution meter to decameter-scale satellite imagery to extrapolate the probable extent of where particular mineral compositions are also likely to occur. We use the term spectro-morphological mapping to describe this technique.

The objectives of this paper are: (i) differentiate the various units that make up the Libya Montes region on a finer scale than previous studies, (ii) to describe the mineral stratigraphy and deduce the chronology of the development of geologic units and specific minerals, (iii) to determine the relationships between aqueous minerals and the surrounding geologic units at central Libya Montes, and (iv) to further refine our knowledge of the geologic history of the central Libya Montes region.

2. **Methods**

2.1. **Image and terrain data processing**

Mars Reconnaissance Orbiter (MRO) Context Camera (CTX) (Malin et al., 2007) and High Resolution Imaging Science Experiment (HiRISE) (McEwen et al., 2007) images of the region were downloaded from the Imaging Node of NASA's Planetary Data System (PDS), map projected using ISIS software tools, and further processed, mosaicked, and trimmed by means of programs and tools developed at the German Aerospace Center (DLR), running in the VICAR development environments. Mars Express High Resolution Stereo Camera (HRSC) (Neukum et al., 2004; Jaumann et al., 2007) nadir images and digital terrain models (DTMs) were derived and processed at the DLR (Scholten et al., 2005; Gwinner et al., 2009; Gwinner et al., 2010) as well as mosaicked and trimmed with respective DLR-software tools. The resulting datasets are 160 by 136 km-sized CTX (6 m per pixel) and HRSC (12.5 m per pixel) image mosaics as well as an HRSC-DTM (50 m per pixel) mosaic covering the entire study region. HiRISE images (25 cm per pixel) were selected individually for locations of particular interest and downloaded from the PDS. Their processing involved correction of map information, i.e., modification of the center latitude tag into a standard parallel tag. Without that correction the longitude offset of

HiRISE images would be computed falsely leading to a misplacement of the data. The datasets were prepared in equirectangular projection, respectively.

The HiRISE Digital Terrain Models (DTMs) that have been used in this study were kindly provided by the University of Arizona (see acknowledgments) and produced by the methods described by *Kirk et al.* (2008). Stereo coverage is required for the derivation of the 3D information such that the same location is imaged from two separate orbits. The MRO spacecraft rolls produce stereo convergence angles ranging from 15° to 30°, and provide proper parallax for highly variable (rugged) and smooth terrains, respectively. If significant jitter is present in one or both images, the image geometry is first corrected as described in *McEwen et al.* (2010) before producing the DTM and associated products.

2.2. **Spectral data processing and analysis**

The mineralogical composition of discrete morphological units in the study region was analyzed be means of CRISM full resolution targeted (FRT) and half-resolution short or long (HRS/HRL) mode images with version TRR3 (targeted reduced record) calibration (Murchie et al., 2009; Bishop et al., 2013b). These hyperspectral images generally span ~10 km and have ~18 m/pixel (FRT) or 36 m/pixel (HRS/HRL) spatial resolution. The images were processed using the CRISM Analysis Tool (CAT) versions 7.2 and 7.3 for ENVI following standard procedures (Murchie et al., 2007; Murchie et al., 2009). First order variations in illumination were corrected by dividing the I/F image (containing radiance over solar flux) by the cosine of the incidence angle (the angle between incidence solar radiation and the sloped surface, where the surface slope was derived from MOLA gridded topography at 128 pixels/degree). Atmospheric molecular opacity effects were minimized in the long-wavelength (L-images; 1.0 – 3.9 µm) images by dividing by a scaled atmospheric transmission spectrum over Olympus Mons using the McGuire et al. (2009) technique. A denoising algorithm (Parente, 2008) was applied to the L-images in order to remove spikes and stripes. The images were georeferenced and draped over HRSC terrain models in order to better visualize the relative positions and stratigraphic relationships of the various spectral units within the local topography. 3D surface views of CRISM data were created using HRSC elevation data for selected images in order to illustrate where the spectra were collected.

CRISM spectral data extend from 0.4 to 3.9 µm, but were evaluated intensively in the 1-2.65 µm-region because this spectral range is specifically sensitive to hydrated and hydroxylated silicates, carbonates and sulfates. Spectra were collected for small regions of interest (e.g. 5x5 or 11x11 pixels) depending on the size of the outcrop and ratioed to similarly-sized spectrally neutral areas acquired in the same column of the detector in order to minimize instrument artifacts and enhance the spectral features from the surface minerals. CRISM compositional maps were prepared using parameters developed previously (Pelkey et al., 2007; Viviano-Beck et al., 2014). Many compositional maps were created for this study using the parameters i) R: 2500 nm, G: 1500 nm, B: 1208 nm for a standard false color view, ii) R: D2300, G: OLINDEX, B:

LCPINDEX to map the major geologic outcrops, and iii) various combinations of parameters for CAR (carbonate), PAL (Al-phyllosilicate), and PFM (Fe/Mg-phyllosilicate) developed by Viviano-Beck et al. (2014) for identification of specific aqueous outcrops. Map-projected Targeted Reduced Data Record (MTRDR) hyperspectral image cubes (Seelos et al., 2012; Bishop et al., 2013b) were included in our analysis when available for our study region. The MTRDR images include both the VNIR and IR detectors of the CRISM instrument, providing spectra over the full range collected by CRISM and with improved spatial and spectral quality (Seelos et al., 2016).

2.3. **Data combination and exploitation**

All datasets were combined and overlain onto each other in a Geographic Information System (GIS) project by means of the ArcGIS software version 10.3 by ESRI. Marginal spatial offsets between the Mars Express data (HRSC) and the Mars Reconnaissance Orbiter data (CTX, HiRISE, and CRISM) were minimized by through georeferencing using HRSC as the reference dataset. Three-dimensional perspective views of the region were created by means of the ArcScene environment of ArcGIS using HRSC topography as the reference surface for all superposed datasets. The vertical exaggeration factor of all perspective views is set to 2. Geological cross sections were constructed using the 3D Analyst tool in ArcMap, then exported to Microsoft Excel for graph creation and marking of the geologic contacts and later delivered to Adobe Photoshop and Adobe Illustrator for colorizing and labelling.

→ Table 1 **(input data) about here or at the end of the paper**

2.4. Spectro-morphological mapping

Mapping was performed in the ArcMap environment of ArcGIS with a mapping scale of 1:20,000. The dataset used as the basis for this working step is shown in Figure 2. It combines the mineralogical information from CRISM parameter products with features observed in CTX image data. The mineralogical composition of the surface units was deduced from the color coding of the CRISM parameter products. Using the parameter combination R: D2300, G: OLINDEX, B: LCPINDEX, phyllosilicate-rich units appear in reddish to orange colors, olivine-rich units in green tones, and pyroxene-bearing units appear in blue. Yellow regions indicate a mixture of olivine-bearing materials with phyllosilicate components and pinkish regions comprise phyllosilicates and pyroxenes (see color wheel shown in Figure 2). This color code provided the basis for unit assignment. Additionally, image cube-derived ratioed reflectance spectra of individual units were used to validate the parameter product classifications. In order to distinguish between certain subunits from each other, further CRISM parameter combinations were used. For example low-calcium pyroxenes (LCP) versus high-calcium pyroxenes (HCP) were discriminated using CRISM's Map-Projected Targeted Reduced Data Records (MTRDR) parameter combination R: HCP, G: OLV and B: LCP. In these images LCP appears in magenta and HCP in reddish tones. Carbonates can be better identified using the parameter combination R: BD2299, G: BD2500 and B: BD2190. Since carbonates occur intermixed with other phyllosilicate-bearing materials they appear in yellow in these images.

CTX texture was used to interpret the unit's morphology and extent at a scale of 1:20,000 in places where CRISM data are not available. It is important to note that the morphologic units do not always correlate one-to-one with the spectral units. For that reason it is not possible to deduce every unit's surficial extent from image data. This particularly applies for the phyllosilicate- and carbonate-bearing units, as these hydrated minerals are often part of aqueously altered parent rock units. However, the extent of the pyroxene-bearing caprock and bedrock units, for instance, can certainly be reproduced by subsuming the uniform unit's morphology into our identification and mapping criteria.

This mapping procedure combines identification of distinct morphological units in association with their major mineralogical components. Consequently, unit labels comprise morphological and mineralogical information (e.g., Bpx = pyroxene-bearing bedrock, olivine-rich layered unit = LUol, phyllosilicate-rich outcrop = Ops) rather than age and geology (e.g., Nm = Noachian massif (Crumpler and Tanaka, 2003)), which better meets the mapping goals of this study.

➔ Figure 2 **(CRISM mineral maps onto CTX mosaic) about here**

3. **Results**

3.1. **Regional morphologic units**

Ancient highland rocks in the study region were mapped as pyroxene-bearing bedrock (Bpx). In our CRISM parameter products, this bedrock appears in deep blue colors intermixed in places with red spots indicating that the ancient rocks are predominantly high in low-calcium pyroxene and are partially altered. They are high in elevation, exhibiting ~2000 m of relief over rugged slopes of up to ~29° ~~of~~ with sharp ridged crests. This unit also comprises all impact craters larger than 5 km. On the lower inner flanks of Bradbury crater but also in other parts of the highlands, the ancient basaltic bedrock appears to be intensely fluvially dissected. In the CRISM parameters, these surfaces do not differ significantly in color from the Bpx, however, morphologically this is clearly a distinct unit from the bedrocks. Thus, they were mapped as a separate unit named pyroxene-bearing fluvially dissected bedrock units (DBpx). They feature narrow parallel valleys that are partially degraded and incise deeply into the rocks.

An olivine-rich layered unit (LUol) occurs predominantly at the transitional terrains between Libya Montes and Isidis Planitia. It appears in green colors in CRISM parameter data and crops out from underneath a pyroxene-bearing caprock unit (Cpx). The olivine-rich unit shows grooves and yardang-like elongated structures aligned in a south to north direction that are intermixed with fields of small bright ripple-like bedforms resembling transverse aeolian ridges (TARs, Balme et al., 2008), whose crest-ridges are predominantly oriented in east-west directions (Figure 3). This mixture of bedrock and sandy bed forms variegates on the scale of 10's to 100's of meters.

The Cpx unit superposes the LUol unit and covers mostly the northern parts of our study region. This caprock unit spreads into the Isidis Basin where it merges into a knobby, pyroxene-bearing basin-filling unit (cf., Tornabene et al., 2008; Erkeling et al., 2012). At the border to the Isidis Basin, there is a distinct and jagged geologic boundary between the LUol and the plains-covering Cpx unit (Figure 3 a, d). Measurements in HiRISE DTM at this boundary show that this capping unit is up to 25 m in thickness (**Error! Reference source not found.**). Between Hashir crater and Isidis Basin, Cpx is only present as discontinuous patches, possibly left by aeolian erosional processes. In the CRISM parameter products, this unit has been identified by its blue color, which is slightly brighter than the blue of the Bpx unit. The caprock unit features a smoother surface (relative to the LUol) on the scale of CTX images with scattered smaller craters, predominantly in the size of a few 10s of meters.

➔ Figure 3 **(LUol surface features) about here**

➔ Figure 4 **(Geol. Contact and Cpx thickness) about here**

Besides these spatially extensive units we also identified local bedforms and longitudinal morphological features in the study region. These landforms comprise numerous small parallel channels, longitudinal valleys (partially featuring remnants of interior channels) and three fan-shaped deposits (see Figure 5). The latter deposits are located within the Bradbury region and were analyzed in detail by Erkeling et al. (2015), Erkeling et al. (2016) and Bramble et al. (2017a) (see Sec. 4.5. for further discussion). In the CRISM parameter products, these bedforms appear in dark blue colors intermixed with green and reddish spots that appear to represent a mixture of the compositions of

Libya Montes materials. We mapped these deposits as basaltic fan deposits (FDb) in the present project. Most parallel channels lead down the flanks of Bradbury into the crater's interior where they terminate at two sediment fans at the crater center (see lower right in Figure 5). Within the Hashir region, two major longitudinal valleys systems are identified. They originate in the Libya Montes highlands and lead into the plains to the north (see west of Hashir crater in Figure 5). One valley terminates at a heavily eroded, unnamed 8-km-impact crater. It is at this location, where we detected some of the most spatially extensive occurrences of Fe/Mg-clays in our study region. The other longitudinal valley system passes Hashir crater and runs into the plain dominated by the olivine-rich layered unit and which also features various outcrops of smectites and carbonate signatures. All of these landforms show evidence of erosional and depositional processes associated with flowing water.

Phyllosilicate-rich outcrops (Ops) are exposed at numerous sites across the study region. This unit includes Fe/Mg-rich phyllosilicates, Al-smectites and in some cases carbonates mixed with Fe/Mg-smectites generally appearing in red, orange, and pinkish colors in CRISM spectral parameter products. These exposures are most likely either related to features that crop out from the subsurface (e.g., at the central peak of Hashir crater), are directly associated with the Libya Montes bedrock materials (e.g., along the walls of the mountainous massif), or are associated with fluvial or lacustrine sedimentary deposits (e.g., at the fan-shaped deposit at the breach in Bradbury's northern crater rim). A detailed discussion of those units follows in sections 3.2 and 4.

Dark fine-grained sediments have been deposited as large sand dunes (forming predominantly barchans to elongated barchan planforms) on the floor of Dulovo crater. These characteristic aeolian bedforms appear in a dark green color in the CRISM parameter maps and show spectra typical for a mixture of pyroxene and olivine. Hence we mapped this material as pyroxene- and olivine-rich sands (Solpx). These dark basaltic dunes are compositionally comparable to the bulk of the large dark dunes on Mars, which are interpreted to have formed of ancient volcanic ash (Tirsch et al., 2011; Tirsch et al., 2012). This unit is also observed along the wall of Dulovo crater where it is exposed as an olivine-bearing sandy horizon. At many places on Mars, such dark sediment layers are presumed to be local sources for the intra-crater dune sands (Tirsch and Jaumann, 2012; Tirsch et al., 2013).

The result of this coordinated morphological and mineralogical analysis is shown in Figure 3. It reflects the variety of geological processes and events along the transition zone between the Libya Montes and the Isidis impact basin.

➔ Figure 5 **(morphological mapping) about here**

➔ **Error! Reference source not found. (mapping units) about here**

3.2. **Spectral characteristics and local morphology of aqueous alteration minerals**

HiRISE images provide additional insights into the morphologic diversity and the context of stratigraphic relationships associated with the aqueous mineral spectral units. Fe/Mg-smectites, which are detected around the locations where subsurface units are exposed to the surface (sites labelled as a, b, e, and f in Figure 5 and Figure 6), have a rough and hummocky texture in HiRISE images and usually show no layering. Fe/Mg-clays were mapped using the 2.3-µm band parameter and thus appear red in the CRISM parameter products. We found spectral variability in these types of phyllosilicates indicating the presence of an iron-bearing smectite (nontronite, spectral bands at 1.43, 1.91, 2.29, and 2.41 µm), and a magnesium-bearing smectite (saponite, spectral bands at 1.39, 1.91, 2.31, and 2.38 µm) or a mixture of the two forms of smectite termed Fe/Mg-smectite, although the bands near 1.4 µm are often not visible. These detections build on previous work at the Libya Montes region (Bishop et al., 2013b) to the west of the current study site, where variations were also observed in the Fe and Mg content of the smectite-bearing unit.

Al-smectites exposed at the Hashir crater region are associated with massif units but do not possess distinct contacts with the circumjacent rocks. They appear as distinctly brighter tones in HiRISE images (Figure 6c) that smoothly dissolve into the darker tones of the basement. Within the Bradbury region, they occur more distinctly and are associated with very bright layers within the fan-shaped deposit at a breach in the northern rim of Bradbury crater (Figure 6d) (Bishop et al., 2013b; Tirsch et al., 2015; Erkeling et al., 2016; Tirsch et al., 2016). Al smectites were mapped using the 2.2-µm band parameter, but also appear as green tones in our CRISM mineral maps due to weak Fe^{2+}-absorption signals near 1 µm that are likely resulting from some the basaltic parent material. Ratioed CRISM spectra confirm the presence of these minerals in all exposures with clear absorption bands at 1.41, 1.91, and 2.19 µm (spectrum c and d in

Figure 6 bottom), a signature consistent with beidellite rather than montmorillionite which is characterized by a 2.21 absorption feature in addition to the 1.4 and 1.9 µm features (Bishop et al., 2011; Bishop et al., 2013b).

Within one fan-shaped deposit at the Bradbury region, we noticed a variation in the aqueous mineral signatures (Figure 7): A larger mineral outcrop near the front of the northern fan deposit (outcrop 1; Figure 7a, b, and c) has a strong and distinctive beidellite signature with the typical 1.4- and 2.19-µm bands. We identified this signature along a discrete layer that crops out along the margins of the fan-shaped deposit. HiRISE close-ups reveal a polygonal pattern on the surface of this layer in places where larger parts are exposed to the subsurface (Figure 7c). Another smaller outcrop at the rear eastern margin of the fan deposit (outcrop 2; Figure 7a, b, and d) is more consistent with opal as inferred from the broader bands at 1.40 - 1.41 µm and 2.20 - 2.23 µm as well as a possible band at 2.28 µm. These opaline-silica-bearing outcrops are distributed in scattered bright patches along a small canyon wall but do also align with some discrete bright layers on the floor of this small canyon (Figure 7d). The spectral signatures of these smaller, bright altered spots are difficult to resolve, likely because they comprise only part of each pixel (Figure 7). A further spectral signature of a thin (a few 1x1 CRISM pixels) bright layer along a nob in the middle of this smaller opal-bearing outcrop could be consistent with hydrated calcium chloride (Figure 8). It shows absorption bands at 1.44, 1.99, 2.11, 2.37 and 2.48 µm that are indicative of chloride salt minerals such as sinjarite ($CaCl_2 \cdot 2H_2O$). Sinjarite has an additional feature near 2.58 µm that is not observed in the CRISM spectra of this bright layer; however, calcium chloride hexahydrate ($CaCl_2 \cdot 6H_2O$) does not include this feature. A shoulder feature is observed near 2.37 µm in the spectrum of sinjarite and a stronger band here is present in the spectrum of hydrated calcium perchlorate ($Ca(ClO_4)_2 \bullet 4H_2O$). Therefore, we suggest that a mixture of these CaCl-bearing salts could be present. Additional spectra of perchlorates and chlorides are available in Bishop et al. (2014), Bishop et al. (2016), Hanley et al. (2014), and Hanley et al. (2015).

At the Hashir region as well as at the Bradbury region, we detected carbonate-bearing outcrops (see Figure 5, Figure 11 and Figure 13). At both sites, these carbonates are intermixed with Fe/Mg-smectites. At the Hashir region, these carbonates are contained in an altered unit that is overlain by the LUol unit and is exposed from the subsurface in a few places (Figure 6e). At the Bradbury region, they appear along the eroded highland flanks of the ancient bedrock (Figure 6f). In both cases the carbonate-bearing rocks represent altered ancient bedrock and likely formed together with the Fe/Mg-smectite. Their spectra comprise carbonate bands near 2.30-2.32 and 2.52-2.54 µm, in addition to OH bands observed near 2.30 and 2.39 µm in the spectra of units dominated by Fe/Mg-smectite. An increase in band depth at 2.53 µm could be consistent with Fe- or Ca-rich carbonates whereas a carbonate band center at 2.30 µm is characteristic of Mg-rich carbonate. However, the band centered at 2.3 µm is likely influenced by overlapping bands due to Fe/Mg-smectites near 2.29 µm and carbonate at longer wavelengths, as seen in mixture spectra (Bishop et al., 2013a). The feature near 2.5 µm is broader than observed for pure carbonates and may reflect a mixture of carbonate and phyllosilicate signatures. Previous analyses of carbonate-bearing regions at Libya Montes, e.g., at the heavily eroded, unnamed 8-km-impact crater west of Hashir (Figure 5) and in the geological similar context north of Hashir, showed this to be most consistent with the spectrum of dolomite, a carbonate containing Mg, Fe, and Ca (Bishop et al., 2013b). Laboratory spectra of smectites and carbonates are compared with a nontronite-bearing spectrum from Hasher crater and a carbonate-smectite mixture spectrum from Bradbury crater (Figure 4). Spectrum f with the strongest carbonate features includes bands near 1.39, 1.91, 2.31 and 2.39 µm that are consistent with saponite and features near 2.32 and 2.53 µm that are consistent with dolomite.

➔ Figure 6 **(HiRISE morph, CRISM params + spectra) about here**

➔ Figure 7 **(Types of aqueous minerals within fan delta) about here**

➔ Figure 8 **(Calcium chloride) about here**

4. **Discussion: Stratigraphy of units and geologic history**

4.1. **Pyroxene-bearing Bedrock**

The rugged mountainous bedrock (Bpx) of the Libya Montes massif is the stratigraphically lowest unit because it is overlain by all the other morphological units in the study area. It is of Noachian age (3.9 to 3.7 Ga (Bishop et al., 2013b)) and therefore not only the oldest unit of the study region, but also represents some of the most ancient highland rocks exposed on Mars (Greeley and Guest, 1987). It comprises the Noachian massif (Nm) and parts of the Noachian/Hesperian fluted and dissected (NHf) units as mapped by Crumpler and Tanaka (2003) and later refined by Bishop et al.

(2013b). Erkeling et al. (2012) distinguished this unit in Noachian cratered (Nc) and Noachian mountainous (Nm) terrain. These rocks likely represent the uplifted and faulted pre-impact target rocks that are now remnants of the old Isidis Basin crater rim-terrace complex and correlates with the impact age of 3.9 Ga (Werner, 2005; Ritzer and Hauck, 2009). The basaltic composition, comprising low olivine and higher LCP concentrations, is comparable with the basement rock found elsewhere on Mars, e.g., in Nili Fossae (Amador and Bandfield, 2016), Northeast Syrtis Major (Bramble et al., 2017b), in Valles Mariners (Viviano-Beck et al., 2017) or the southern Isidis region (Tornabene et al., 2008; Bishop et al., 2013b). Again similar to these basement rocks, the Bpx unit comprises patches of hydrated mineral phases (see Sec. 4.4 and 4.5) supporting aqueous and/or hydrothermal alteration of the parent rocks (cf., Bishop et al., 2013b). The fluvially dissected parts of the bedrock unit (DBpx) are comparable with the Noachian dissected unit (Nd) mapped by Erkeling et al. (2012). The narrow, parallel, and sometimes dendritic structure of the incised channels points to precipitation-induced surface runoff. Waters formerly draining through the numerous small parallel valleys into Bradbury crater's interior (Figure 5), led to the development of two alluvial fan deposits in local depressions inside the crater. Erkeling et al. (2015) and Erleking et al. (2018) dated the formation time of the parallel valleys at the inner flanks of Bradbury crater between ~3.7 and ~3.8 Ga constraining the surface runoff events to Late Noachian/Early Hesperian times.

4.2. **Olivine-rich Layered Unit**

The olivine-rich layered unit (LUol) has been generally deposited in topographic lows where it embays the pre-existing Libya Montes terrain. It is in turn embayed by the Isidis plains-covering material (Cpx) to the north of our study region (cf. Figure 15 in Tornabene et al. (2008)). It seems to conform with local slopes as it is emplaced on the flanks of uplifted materials. This is where HiRISE images reveal an internal banding of this unit with several strata of varying thickness (Figure 9). Particularly, this can be seen at sites a, b, and e (cf. Figure 5 and Figure 6) where the Fe/Mg-phyllosilicates crop out from the subsurface. A close-up view based on HiRISE imagery shows the layers both embay and unconformably overlie the pyroxene- and phyllosilicate-bearing central uplift of Hashir crater, but also dip away from the central uplift in all directions (Figure 9f). Measurements in HiRISE-DTMs reveal layer thicknesses between ~28 and ~77 meters, whereas most layers are thinner than ~45 meters (Figure 9c).

➔ Figure 9 **(OL layer thickness profile) about here**

Banding in an olivine-rich unit has also been discovered at Northeast Syrtis Major by Bramble et al. (2017b). Similar to our study results, this northern olivine-rich unit is always located underneath a pyroxene-bearing capping unit (Mustard et al., 2007; Bramble et al., 2017b), which might be an indicator that the olivine- and pyroxene-bearing units (LUol and Cpx) are of the same or related origin (see further discussion in Section 4.3.). Likewise, spectral mapping with TES and THEMIS data by Tornabene et al. (2008) revealed an olivine-rich basaltic unit that is often associated with a pyroxene-bearing, olivine-poor, semi-resistant cap unit, which shows crude layering in high-resolution images. According to this study, this unit was not only detected at the Nili Fossae region, it can be furthermore traced from the Libya Montes region up to the Isidis basin, where it is covered by the pyroxene-bearing basin filling unit and only appears in impact crater ejecta that excavated the olivine-rich basaltic unit from beneath the plains. Due to its olivine-rich composition, this layered unit is suggested to represent impact melt from the giant Isidis event (Mustard et al., 2007), olivine-rich basalts from volcanic processes (Hamilton and Christensen, 2005; Tornabene et al., 2008), or represents ancient crustal rock that are exposed to the surface in the course of the Isidis impact. The layering of the LUol as well as the fact that it appears to follow the topography are indicative of a flow, which rules out the crustal rock hypothesis and points to a volcanic or impact melt origin. Recently, a focused study on the morphometric properties of the layers of the circum-Isidis olivine-rich unit by Kremer et al. (2018) indicates that the unit decreases in thickness with distance from Nili Patera, and that the unit most likely represents olivine-rich ash-fall deposits originating from Syrtis Major. Regardless, the various observations give rise to the suspicion that the both the northern and southern units are related to each other and that they were likely generated by the same event or process.

The grooves and yardang-like, elongated structures as well as the numerous transverse aeolian ridges on the surface of the LUol unit indicate aeolian modification in the form of abrasion, scouring and accumulation (Figure 3). The orientation of these linear features implies a prevailing erosive wind direction from south to north that is consistent with the alignment of the TARs perpendicular to the wind path. Also the wind streaks behind obstacles at the southern border of Isidis Planitia confirm winds blowing towards norther direction. The whole region between Dulovo, Hashir and Bradbury craters might be a zone of katabatic winds blowing from the Libya Montes downslope into Isidis Planitia, which frequently can occur at the peripheral regions of mountain ranges especially in cold climate regions (Oliver and Fairbridge, 2005; Vihma et al., 2011). Tornabene et al. (2008) reported that this area provides some of the highest TES and THEMIS thermal inertia values on Mars suggesting a mix of bedrock and the development of a course lag unit at the transition between the Isidis and the Libya Montes. The authors also believe that the lag deposit might result from the action of high katabatic winds imposing on the Montes, which create relatively high erosion. In our interpretation, the intense action of the wind does not account for a sedimentary origin of the entire olivine-rich unit, as discussed but not favored by Tornabene et al. (2008). However, it does explain how this unit has been extensively shaped and also which process likely led to the erosion of the pyroxene-rich cap unit that formerly covered the LUol across the study region. Age dating of the LUol unit at the Hashir region conducted by Bishop et al. (2013b) resulted in an absolute model age of 3.78 Ga and a resurfacing age of 816 Ma. We propose that this resurfacing has been driven by the aeolian erosion by katabatic winds as discussed above. The age is consistent with a deposition of this unit well after the Isidis Basin formation (~3.9 Ga (Ritzer and Hauck, 2009; Werner, 2009)). The age of the unit is inconsistent with an impact-melt interpretation suggested by Mustard et al. (2007) and Mustard et al. (2009); the age is more consistent with the unit being derived as both early- and late-stage volcanic by-products produced by low degrees of partial melting of the Martian mantle as a hot spot initiates and subsides (Tornabene et al., 2008). Also the theory of (Kremer et al., 2018) is conceivable suggesting this unit to represent air-fall deposits from Syrtis Major because of the absence of vents capable of feeding picritic magma in the nearby terrains. However, if the cooling of the melt sheet generated by the Isidis Basin was on the order of a 100 million years vs. 10 or so (Abramov and Kring, 2005) it admittedly leaves these two hypotheses for the origin of the olivine-bearing unit found in the Isidis/Nili Fossae region open to debate. In turn, the occurrence of the LUol unit on the floor of Hashir and Bradbury craters speaks against the impact melt hypothesis and strengthens the volcanic origin theories (lava flow or air fall deposits) because the unit must have been deposited there well after the formation of these two craters which certainly postdate the Isidis impact because they are superposed onto the Isidis rim complex.

4.3. **Pyroxene-bearing Caprock**

The pyroxene-bearing caprock (Cpx) unit lies stratigraphically and topographically above the olivine-rich layered (LUol) unit (Figure 4). By virtue of its extent along the outer margin of the Isidis Basin, Erkeling et al. (2012) termed this unit "Isidis Exterior Plains". This extensive unit in Isidis Planitia has been interpreted to represent either vast lava depositions, presumed to have originated from the Syrtis Major province (Mustard et al., 2007; Tornabene et al., 2008; Jaumann et al., 2010; Ehlmann and Mustard, 2012), indurated mud flows emplaced by mud volcanism (Ivanov et al., 2014) or fan materials deposited at the terminus of valley networks (Crumpler and Tanaka, 2003). It correlates with the semi-resistant and olivine-poor basaltic caprock unit identified by Tornabene et al. (2008) that overlies the olivine-rich unit and extends across the Isidis plains. In contrast to the low-calcium pyroxene bearing bedrock unit, this caprock contains high-calcium pyroxenes that is consistent with basaltic lavas (Figure 10). This transition from older low-calcium pyroxene rocks to younger high-calcium ones on Mars may be merely explained by the thermal evolution of the planet over time. Mars would have had higher production rates of crustal materials early in Martian geologic history that would have been capable of producing low-calcium pyroxene-rich Noachian rocks as petrological expressions of earlier/hotter volcanism rather than being associated with a mantle-overturning event following the crystallization of a magma ocean (Baratoux et al., 2013).

➔ Figure 10 **(Hashir MTRDR) about here**

Due to its composition and appearance, we favor the interpretation of Mustard et al. (2007) and Tornabene et al. (2008) that the caprock unit could be attributed to remnants of volcanic deposits generated from later stages of the evolution of the plume associated with Syrtis Major (Fawdon et al., 2015; Fawdon, 2016). As the primary focus of this study is on the aqueous minerals, we will not delve into further detail on the origin of this unit. The reader is referred to the references herein, especially to Tornabene et al. (2008), for a comprehensive discussion of the possible origins of this unit. Since the olivine-rich unit is always associated with the pyroxene-bearing caprock throughout our mapping region (e.g., Figure 5), they are most likely related to each other. Hence, the olivine-rich unit could be also volcanic in origin rather than represent differentiated impact melt. A very similar pyroxene-bearing capping unit has been reported elsewhere on Mars, for example in Mawrth Vallis and Oxia Planum (e.g., Loizeau et al., 2007; Bishop et al., 2008; Wray et al., 2008; Loizeau et al., 2010; Loizeau et al., 2015). It was interpreted to represent remnants of volcanogenic ash deposits once covering the whole region before is has been partly eroded (Loizeau et al., 2015).

4.4. **Aqueous alteration minerals at the Hashir region**

Fe/Mg-smectites at the Hashir region crop out from the subsurface north of Hashir crater and from underneath a heavily eroded unnamed impact crater floor. They are exposed along the walls of Dulovo crater and form the central peak of Hashir crater (Figure 2, Figure 11 and Figure 12) suggesting the alteration is either part of the pre-impact target surface or part of the impact process, i.e. hydrothermal. In most cases, the clays are generally identified as occurring stratigraphically below the olivine-rich layered unit. Hence, they are older than the LUol and Cpx units as there is no evidence for overturn since there deposition. Due to the widespread occurrence of these phyllosilicate-rich outcrops, local lacustrine processes or igneous-induced hydrothermal processes are less likely formation mechanisms (Cannon et al., 2017). These phyllosilicates may have evolved instead from pervasive near surface alteration through impact-induced low-temperature hydrothermal processes in ancient bedrock material

(Bishop et al., 2018). For instance the central peak of Hashir crater shows that old, altered basement rocks were lifted to the surface in the course of the impact. Hashir crater itself with only about 16 kilometers in diameter is too small to be responsible for the hydrothermal processes that possibly led to the formation of clay minerals (Osinski et al., 2013; Tornabene et al., 2013). Hence, these minerals likely formed by hydrothermal weathering in the course of the Isidis impact and are thus very old. However, the Hashir impact was most likely responsible for the lifting of these hydrated minerals in the form of the central peak. The infilling of Hashir crater with the olivine-rich layered unit can be constrained to 3.77 Ga because the crater fill unit itself is of this age (see Bishop et al., 2013b). Following these constraints, we can conclude that the smectite formation at this site can be dated to a time at the end of the Noachian between 3.9 Ga (Isidis impact) and 3.77 Ga (olivine layer emplacement). It cannot be ruled out that the water draining through the longitudinal fluvial channels into the areas where we detected hydrated minerals took part in the aqueous alteration processes or that the clay minerals detected here are detrital in origin. However, image data show that most hydrous minerals crop out from well below the subsurface and are not consistent with formation from surface runoff water. Also, cold surface water would not favor formation of the observed smectites (Fairén et al., 2011) as it drastically slows down the alteration which would thus require much longer time scales. This in turn would require a long-term availability of liquid water at this site. However, the fluvial activity in these channels occurred at some point, or points, within a 200 Ma period with the longitudinal valley systems dated to about ~3.7 to 3.5 Ga (Erkeling et al., 2010a). We do not believe that cold water over this time frame would have been sufficient to produce the observed altered units.

Since the Al-smectites in the Hashir region occur as isolated patches within the bedrock unit and not as distinct stratigraphic units (Figure 11), they seem to represent in situ alteration of inhomogeneous ancient basement rocks. A possible formation mechanism would be isolated leaching of the pre-existing Fe/Mg-phyllosilicates leading to the loss of Fe- and Mg-ions and the transition to Al-smectites (Ehlmann et al., 2008b; Bramble et al., 2017b). However, that process does lead to Al-smectites like kaolinite, for example, but not to beidellite which is the dominant Al-smectite at all detection sites (Ehlmann et al., 2008b). Hence, the beidellite is more likely to have formed from low temperature hydrothermal alteration (Grauby et al., 1993) or burial diagenesis of the bedrock materials at this site because beidellite forms at elevated temperatures compared to montmorillionite (Huertas, 2000; Guisseau et al., 2007; Bishop et al., 2011; Bishop et al., 2013b). However, formation of beidellite rather than illite or chlorite indicates that diagenesis progressed only partially (Robin et al., 2015). Thus, diagenesis at Libya Montes occurred over shorter time periods or at lower temperatures compared to diagenesis leading to illite and chlorite. Both of these latter minerals are common in the Nili Fossae region (e.g., Ehlmann et al., 2009) indicating more progressive diagenesis or hydrothermal alteration occurred at the northwest rim of the Isidis Basin.

The dolomite detected in the Hashir region is intermixed with Fe/Mg-smectites and occurs in contact with olivine as it crops out from underneath the LUol (Figure 11). This mineral mixture appears to be the result of alteration of Noachian bedrock by neutral to slightly basic waters, which forms Fe/Mg-phyllosilicates and in some cases carbonates as well (Bishop et al., 2013b). The dolomite in the Libya Montes region is always found together with Fe/Mg-smectite and is thus thought to have formed as the ancient basalt altered. The composition of these altered rocks is likely affected by temperature and fluid chemistry at the time of alteration.

Mg-carbonate detections were reported for the northwestern edge of Isidis Planitia at Nili Fossae (Ehlmann et al., 2008a; Ehlmann et al., 2008b); however, these carbonates have a different chemistry and occur in different mineral assemblages. At the Nili Fossae locations, possible formation mechanisms for the observed Mg-carbonates include aqueous alteration of olivine at the surface with subsequent burial by mafic caprock or the subsurface metasomatic alteration along the contact between Fe/Mg-phyllosilicates and high-temperature olivine-bearing rocks (Ehlmann et al., 2008b; Ehlmann and Mustard, 2012). Carbonates at the Nili Fossae site are associated with serpentine and chlorite as well as Fe/Mg-smectite, while only Fe/Mg-smectite is observed in the Libya Montes region. Magnesite could have also formed at Nili Fossae through reaction of olivine to form serpentine (Ehlmann et al., 2010; Viviano et al., 2013).

➔ Figure 11 **(Hashir minerals) about here**

➔ Figure 12 **(geologic sketch Hashir) about here**

4.5. **Aqueous alteration minerals at the Bradbury region**

Fe/Mg-smectites at Bradbury region were detected at two different geological settings: they are exposed along the walls of the ancient Libya Montes bedrock and they crop out from the western fan-shaped deposit (9 x 7.4 km) at the center of Bradbury crater (Figure 5). The Fe/Mg-smectites detected along the walls of the ancient Libya Montes bedrock (Figure 13) likely resulted from low-temperature hydrothermal alteration of the basaltic parent rock, possibly due to the Isidis impact, similarly to those found at the Hashir region. However, these may have formed differently from the Fe/Mg-phyllosilicates observed elsewhere in the circum-Isidis region that include saponite, chlorite, serpentine and possibly other Mg-rich phyllosilicates not observed at Libya Montes (e.g., Mustard et al., 2007; Ehlmann et al., 2009; Mustard et al., 2009; Brown et al., 2010; Viviano et al., 2013; Bramble et al., 2017b). Hydrothermal alteration in subsurface environments was proposed to explain formation of Fe/Mg-phyllosilicate mixtures of smectite, chlorite, and/or serpentine (Ehlmann et al., 2011) that require higher temperatures than Fe/Mg-smectites.

Furthermore, the scattered occurrence of these altered minerals all along the lower-lying highland units supports this interpretation (Figure 5). The Fe/Mg-smectites at the western fan-shaped deposit in central Bradbury (Figure 5) are likely allochthonus because they occur scattered at different elevations and within different stratigraphic lobes of the deposit (Erkeling et al., 2016; Erleking et al., 2018). Thus, they might represent remnants of eroded altered highland material that has been transported through the parallel valleys and deposited at different parts of the fan. Also, there is no evidence for any process indicating in-situ alteration of pristine fan deposit material after deposition in the lobe.

Carbonates (likely dolomite) intermixed with Fe/Mg-smectites crop out at the base of the bedrock unit and show the strongest signature where marked in the image (Figure 13). Like at the Hashir region, they occur in contact with olivine-bearing rocks. Hence also here, the carbonate formation could have been driven by hydrothermal processes taking place underneath the olivine-rich unit or the interaction of hydrous CO_2-rich fluids with olivine.

➔ Figure 13 **(Bradbury fan delta minerals) about here**

The Al-smectites beidellite is exposed at several layers of the fan-shaped deposit that is ~5 x 3 kilometers in size and located in a depression that breaches Bradbury crater's northern rim (called "northern fan deposit", Figure 5). Before we examine the minerals here in detail, we will briefly discuss the nature of this sedimentary fan deposit in which the beidellite was detected.

The fan-deposit at Bradbury's northern crater rim

In previous studies (Erkeling et al., 2012; Erkeling et al., 2015; Erkeling et al., 2016; Tirsch et al., 2016), this bedform was interpreted to be a delta or deltaic deposit, implying a former lacustrine environment. Likewise, the eastern, smallest fan deposit (~2 x 1.3 km in size) is located within a small crater that superposes Bradbury crater, featuring an inlet and an outlet channel, and is thus interpreted to be a small open basin paleolake by Erkeling et al. (2012). However, Bramble et al. (2017a) argue that the northern fan-shaped deposit does not show any clear evidence for continuous bedding nor changes in bedding geometry or dip angles that are typical for delta deposits. Although it shows clear layering, the dip angles lie constantly at ~7°, which is more indicative of alluvial or debris deposits rather than deltas (Bramble et al., 2017a). The authors also analyzed the western and the eastern fan-shaped deposits at Bradbury's interior and found that they do not exhibit resolvable layering, but are composed of decameter-scale light-toned units with dark-toned fractures overlain by a dark-toned top unit with a rough surface morphology, presumably indicating that these fan-shaped deposits also represent alluvial deposits. Did Bradbury crater ever host a standing body of water or did it experience intense alluvial and fluvial processes? We propose that both occurred. The western and the eastern fan deposits in the central part of Bradbury crater (Figure 5), which feature a network of branching distributary channels, point to alluvial deposition environments (Boggs, 2006). In contrast, the northern deposit at Bradbury's rim breach appears to have been built by a different depositional regime. The higher elevated, upstream part of the deposit with its inverted channel morphology shows features typical for alluvial fans (Figure 14). The inverted channels point to the former existence of subaerial fluvial channels, that have been filled and cemented and were subject to differential erosional events stripping away the less resistant valley walls leaving only the channel fill as topographic high (e.g., Williams et al., 2009; Burr et al., 2010; Newsom et al., 2010; Davis et al., 2016). In contrast, the lower elevation portion of this fan-shaped deposit is located in a confined depression with a distinct, almost crescent-shaped margin towards the downstream direction. This depression might have been carved by a former glacier that terminated at the crescents margin. Hence, it could represent a former pro-glacial lake. However, we do not find any further surviving glacial landforms in the surrounding areas to support this latter hypothesis. Alternatively, this crescent shape could be a remnant of a smaller impact crater that cut Bradbury craters's northern rim and carved the depression for the later water body. Along this terminal margin, several undisturbed horizontal layers are exposed to the surface. Inside this depression, the Al-smectites occur as undisturbed, almost horizontal layers (Figure 14). These accumulations point to a low energy depositional environment as is typical for standing bodies of water. Hence, the sediments at this site might represent subaqueous delta front deposits at the interface between the active fan and a standing body of water (Figure 14). In this scenario, the small, perhaps short-lived pond was fed by ephemeral waters that carved the channels upstream of the alluvial fan. According to these observations, we suggest this bedform be called a fan delta rather than a pure delta or alluvial fan. Fan deltas form where an alluvial fan is deposited into a standing body of water, where the delivered sediments built not only the subaerial alluvial fan but also a subaqueous delta front (Figure 14) (Nemec and Steel, 1988; Boggs, 2006; Dury et al., 2009).

➔ Figure 14 **(Fan Delta) about here**

Since the Al-smectites at Bradbury crater are restricted to this pond site and they are exposed in undisturbed layers along a similar elevation, it seems reasonable that they could have been formed by in-situ alteration of the subaqueous delta front deposits that accumulated in the small lacustrine pond. These phyllosilicates could have formed in situ as montmorillonite and then later altered to beidellite through diagenesis following emplacement of the caprock. Another option is that beidellite formed directly in a pool of very warm water (possibly as high as 100°C) because beidellite forms at elevated temperatures (e.g., Guisseau et al., 2007; Bishop et al., 2011; Bishop et al., 2013b). However, it seems less likely that a standing body of such hot water could have formed here. Alternatively to the in-situ development scenario, the Al-smectites could be allochtonous. In that case, they could have been eroded from altered Libya Montes basement rocks, transported in ephemeral runoff events and subsequently deposited at the alluvial deposit. In this scenario, just like at the Hashir region, the Al-smectites most likely resulted from hydrothermal environments possibly related to impact cratering in the catchment area of the fan delta. The mineral occurrence in neat layers could then have resulted from grainsize fractionation and preferential erosion.

In contrast, the opal-bearing deposit (Figure 7) detected at the subaerial alluvial fan (Figure 14) might have formed through evaporative processes in a hydrothermal or lacustrine system in the course of the aqueous weathering of mafic rocks. The thin bright layer with the unusual spectral signatures attributed to Ca-chlorides reinforces an evaporative formation from brines. A scenario that supports the presence of beidellite, opal and Ca-chlorides in nearby pools at this site could have begun with crystallization in a lacustrine, evaporative environment, followed by mild diagenesis. Authigenic montmorillonite, opal and Ca-chloride salts could have formed in these sediments as they were emplaced. Later, when the delta region was buried, the montmorillonite would have been converted to beidellite through mild diagenesis, while the opal and Cl salts remained. Both early and late halite were found in a study dating terrestrial sediments, which showed that some of the original halite was unaffected by diagenesis, while some of the halite was reprecipitated during diagenesis in pore spaces of the other minerals (Schoenherr et al., 2009). Possibly then mild diagenesis could have sufficiently concentrated the Ca-chloride salts in one location, increasing their abundance to just above the detection limit. Formation of beidellite rather than illite or chlorite indicates that diagenesis progressed only partially (Robin et al., 2015). Future imaging spectrometers with increased spatial resolution in orbit at Mars could enable characterization of such small sedimentary outcrops in more detail.

➔ Figure 15 **(Bradbury fan delta cross section) about here**

➔ Figure 16 **(geologic sketch Bradbury) about here**

5. **Summary and Conclusion**

This study documented aqueous alteration across the central Libya Montes region including outcrops near Hashir and Bradbury impact craters. We employed a mapping technique that combines spectral detections from CRISM near-infrared imagery with geomorphology and topography from HRSC, CTX, and HiRISE imagery. We characterized a variety of units that formed through volcanic, impact, hydrothermal, lacustrine and evaporative processes. These are summarized here and in Figure 17.

➔ **Figure 17 (Stratigraphic chronology) about here.**

- We already learned from previous studies (Tornabene et al., 2008; Bishop et al., 2013b; Tornabene et al., 2013) that impact-induced hydrothermal processes in the course of the Isidis impact event led to the aqueous alteration of the Noachian aged LCP-bearing bedrock resulting in the formation of Fe/Mg-smectites. We continue characterization of these units toward the east and conclude that subsequent volcanic processes resulted in the emplacement of an olivine-rich layered unit (LUol), which is most likely associated with the HCP-bearing caprock unit (Cpx) throughout the study region. We constrain the hydrothermal alteration to about 3.9 Ga (Isidis impact, (Werner, 2005; Ritzer and Hauck, 2009)) to 3.77 Ga (olivine layer emplacement, (Bishop et al., 2013c)).
- This age of the olivine-rich layered unit is consistent with a volcanic origin rather than an impact melt origin (because it is too young to result from the Isidis impact) and strengthens our volcanic interpretation. Moreover, the deposition of the LUol and Cpx units within Hashir and Bradbury craters speaks for an emplacement of these units well after the Isidis event, because the craters are superposed on the ancient Isidis rim and thus postdate the basin formation.

- We confirm the existence of both Fe/Mg-smectites and carbonates (Bishop et al., 2013b) in the Hashir region and revealed additional occurrences at the Bradbury site. We further conclude that the appearance of this mineral mixture hints at alternating environmental conditions, varying from reducing to oxidizing conditions as atmospheric CO_2 content has a strong influence on the formation of Fe/Mg-phyllosilicates and/or carbonates (Viennet et al., 2017).
- In contrast to the Mg-rich carbonates found at Nili Fossae and North Isidis, the dolomites found at Libya Montes likely resulted from the alteration of Noachian bedrock by neutral to slightly basic waters. Although they occur in association with the olivine-rich layered unit, dolomite is unlikely a weathering product of this olivine-rich material. We propose instead that the dolomite formed from Noachian bedrock and that the emplacement of hot lavas (i.e. the LUol) and therefore the induction of heat on top of the already phyllosilicate-bearing basement rocks supported the subsequent alteration to carbonates. Thus, we integrate the age of the carbonate formation to a time after the beginning deposition of the LUol unit.
- We refined the interpretation of the northern fan-shaped deposit at Bradbury crater and conclude that it is a fan delta rather than a delta or a pure alluvial fan (cf., Erkeling et al., 2016; Bramble et al., 2017a) incorporating both alluvial deposition and deposition into a standing body of water.
- Associated with the opal-bearing unit at the fan delta (cf., Erkeling et al., 2016), we first identified possible ca-chloride occurrences, most likely a mixture of CaCl-

bearing salts. These minerals would be consistent with evaporative formation conditions in a lacustrine environment at this site. Thus, they can be dated to a time during or shortly after the fan delta formation.

- We suggest that Al-rich smectites within the Bradbury region may have resulted from hydrothermal alteration or burial diagenesis of the bedrock materials as proposed for the Al-rich smectites at the Hashir region (Bishop et al., 2013b). A possible scenario is that the Al-smectites at the northern fan delta were eroded from the mountains and deposited in the fan deposit. In this case, their relative age would be constrained to a time after the Bradbury impact and before the deposition of the northern fan delta. They would then be stratigraphically much younger than the Fe/Mg-smectites, which was also proposed for many different sites on Mars before (e.g., Ehlmann et al., 2009; Loizeau et al., 2012; Bishop et al., 2013b; Carter et al., 2015). A new scenario that we propose here is that montmorillonite, opal and Ca chlorides were all precipitated about the same time in the pool of the fan delta. Subsequent mild diagenesis would have altered the montmorillonite to beidellite, left the opal intact, and concentrated the CaCl salts.

Acknowledgments

We thank the MarsExpress/HRSC as well as the MRO/CTX, CRISM and HiRISE experiment teams for successful planning and acquisition of the data. The work was supported by visiting scientist funding from the Helmholtz Foundation and Humboldt Foundation, NASA's Planetary Geology and Geophysics program and the NASA Astrobiology Institute. We acknowledge the efforts of the producers of the HiRISE DTMs namely Leocadie Feza Haguma (University of Arizona, DTFED_043264_1835_042763_1835_A01), Sarah Mattson (University of Arizona, DTEEC_007727_1830_008808_1830_A01 and DTEEC_016034_1835_017089_1835_A01), Joel Mueting (University of Arizona, DTEEC_002756_1830_002822_1830_A01). Our special thanks go to Yang Liu (LPI) and one anonymous reviewer whose suggestions significantly improved this manuscript.

Figures

5.1. **Fig. 1**

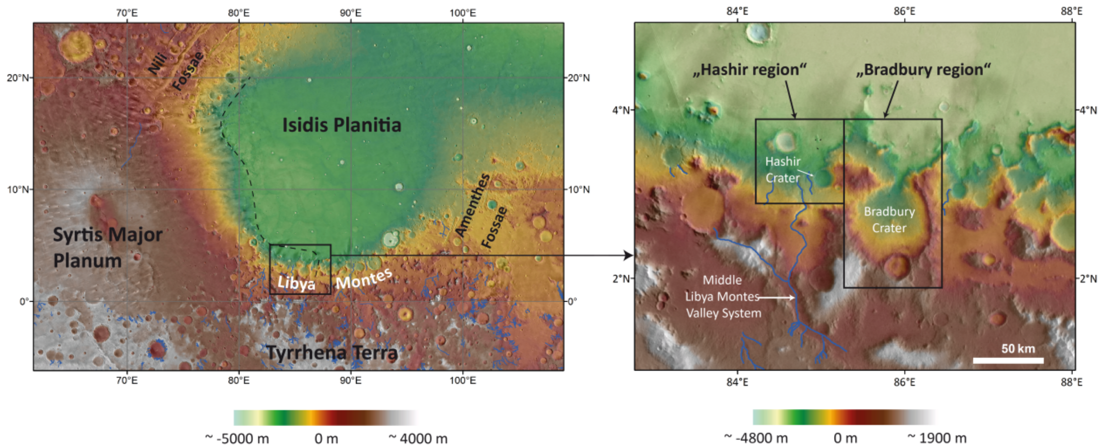

Figure 1: Overview map showing the location of the Libya Montes study region on Mars. Blue lines mark Martian valley networks mapped by Hynek et al. (2010). Shape files downloaded from (Ivanov, 2001); USGS (2016). Black dashed line represents approximate boundary of high to low dust coverage (after Fig. 1b and 2 in Tornabene et al. (2008)). Only west and south of this line, the dust coverage is low enough to allow spectral analyses of the surface. **Left**: Context map of the southern Isidis area. MOLA elevation map superposed on Viking orbiter image mosaic. **Right**: Close-up with labeled names of study regions.

5.2. **Fig. 2**

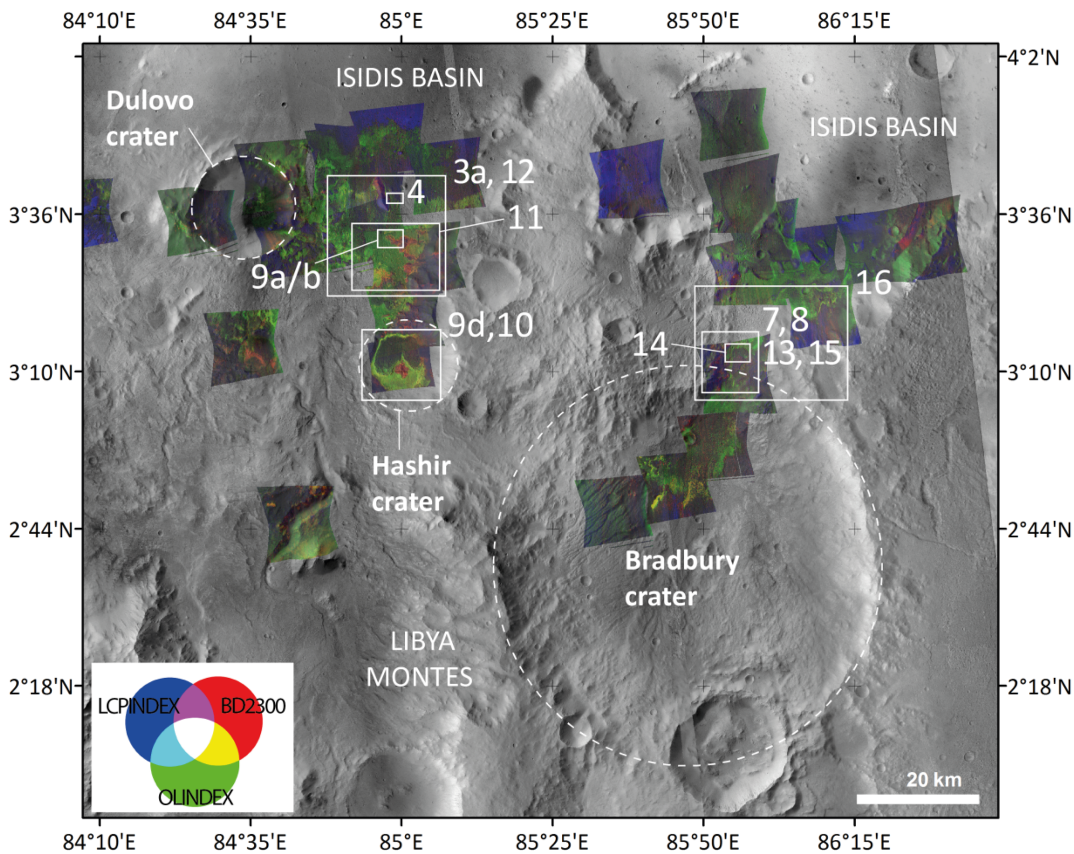

Figure 2: CRISM minerals maps and a CTX image mosaic built the basis for the spectro-morphological mapping (CRISM IR parameter products with R: D2300, G: OLINDEX, B: LCPINDEX; gaps in CTX coverage were filled with HRSC nadir imagery). An additive color mixing wheel is shown in lower left corner to visualize how colors for mineral mixtures evolve. White boxes show the approximate locations of the individual figures shown in this work.

5.3. **Fig. 3**

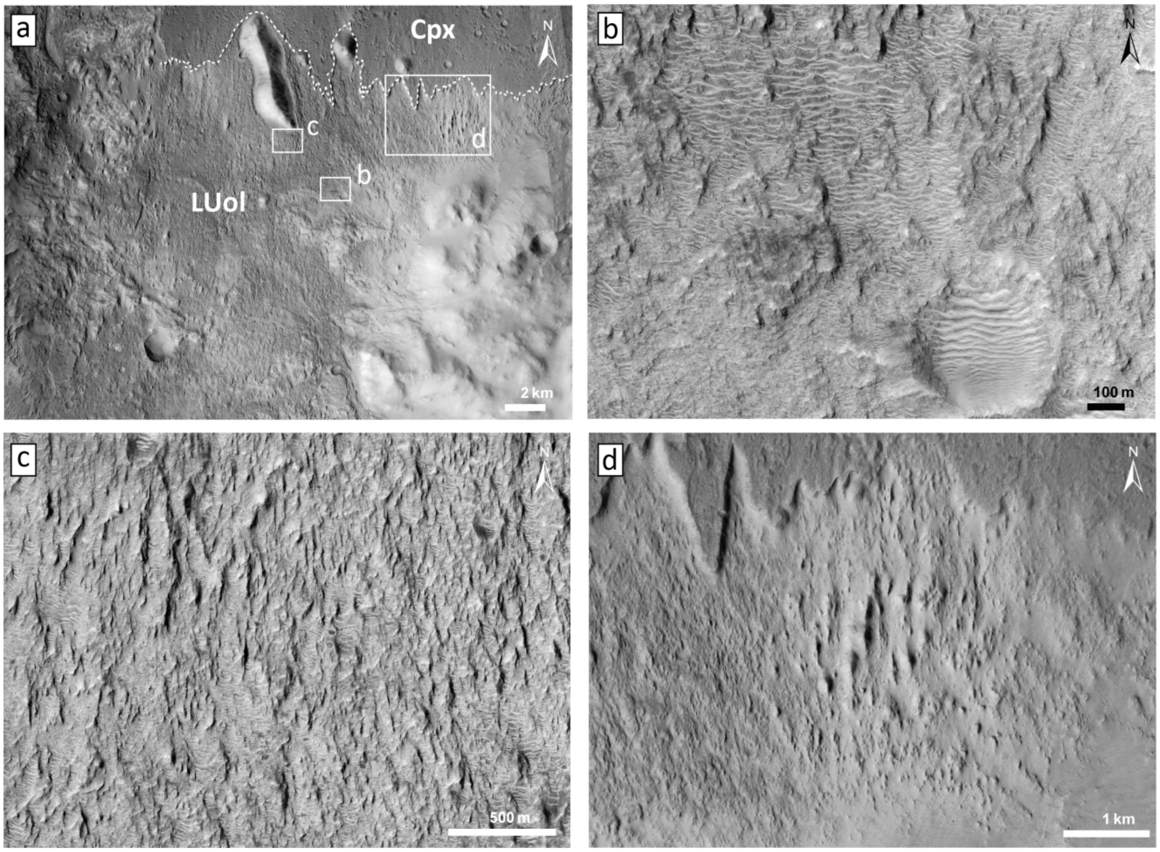

Figure 3: Morphological surface features of the olivine-rich layered unit (LUol). **(a)**: CTX context image showing the unit's exposure at the Hashir region. See Figure 2 for location of panel a. White boxes designate locations of panels b, c, and d. Dashed line traces the jagged geologic boundary between units Cpx (pyroxene-rich caprock) and LUol at the border to Isidis Planitia. **(b)**: HiRISE view of transverse aeolian rigdes in local lows spread across the LUol surface. **(c):** HiRISE view of fluted and grooved surface of LUol. **(d):** CTX view of yardang-like, elongated, linear structures shaped from the erosion of LUol.

5.4. **Fig. 4**

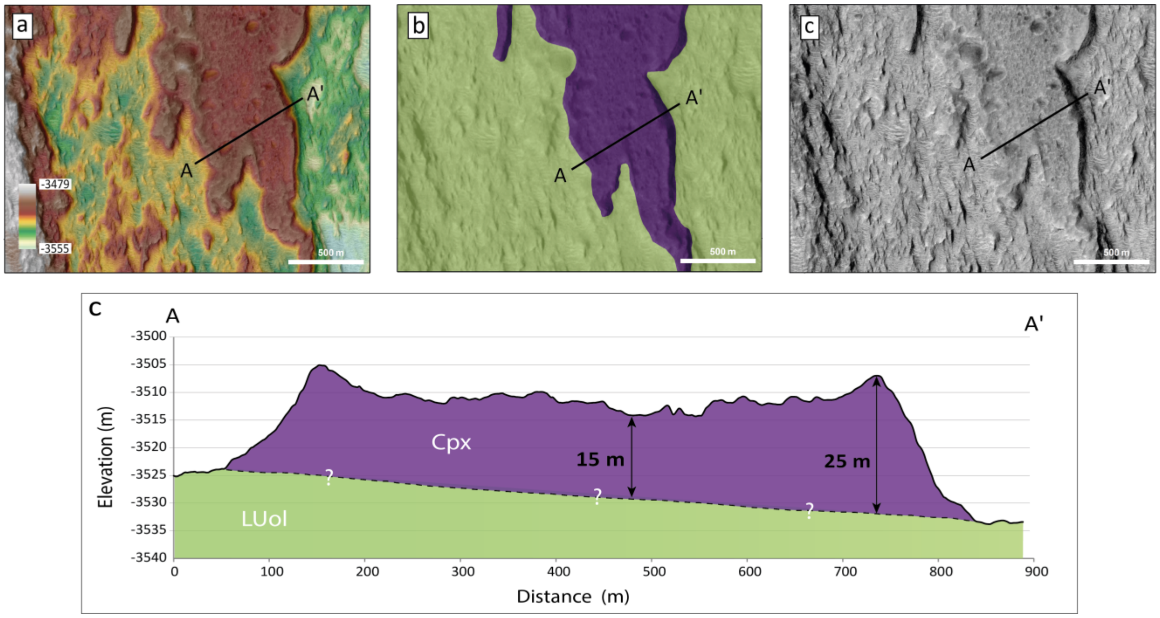

Figure 4: Geologic contact between olivine-rich layered unit (LUol) and pyroxene-bearing caprock (Cpx) at the transition to the Isidis Basin at the Hashir region. (**a**) HiRISE image and color-coded HiRISE DTM (DEETD_043264_1835_04763_1835) with profile line associated with panel (c). (**b**): Same as panel (a), but with HiRISE overlain by spectro-morphological mapping. (**c**): Same as panel (a) and (b), showing pure HiRISE red image. **(d):** Geologic profile A-A' derived from HiRISE DTM. Measured thickness of Cpx varies between 15 to 25 m at this site.

5.5. **Fig. 5**

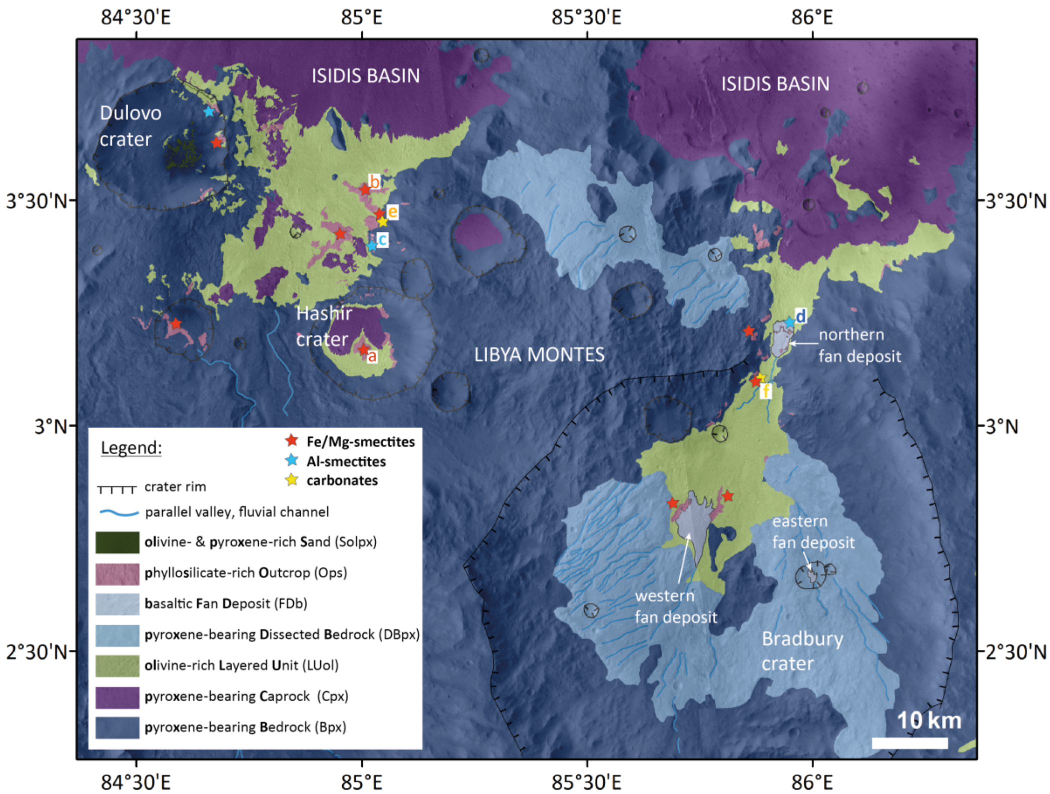

Figure 5: Mapping of the Libya Montes study region as inferred from spectral and image data. Mapping basis: CRISM mineral maps (cf. Figure 2), CTX image mosaic and HRSC topography. Colored-coded stars mark locations where the specific mineralogy of the Ops unit has been determined by detailed spectral analyses. Letters a - f indicate locations of individual mineral outcrops and spectra shown in Figure 6.

5.6. **Fig. 6**

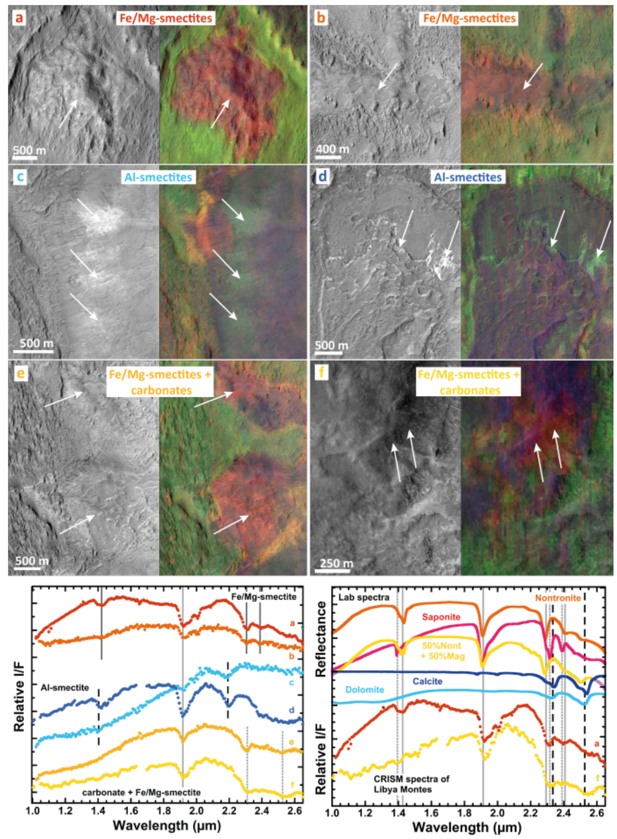

Figure 6: **Top**: Morphology of different phyllosilicate-bearing outcrops at Libya Montes reflecting a heterogeneous formation history (**Left:** HiRISE red image close-ups: a) PSP_002756_1830; b) ESP_017089_1835; c) ESP_16522_1835; d) PSP_007727_1830), f) composition of CTX G21_026583_1830_XN_03N274W and HiRISE PSP_007727_1830; **Right:** CRISM parameter maps overlain onto CTX and HiRISE imagery, R: D2300, G: OLINDEX, B: LCPINDEX, see color mixing wheel in Figure 2 for mineral mixtures). Locations marked on Figure 5 by letters a - f. Annotation colors correspond to spectra in bottom image. **Bottom Left**: Ratioed CRISM NIR-spectra of aqueous minerals detected at the study site. Letters a - f correspond to the minerals in the top image and to locations marked on Figure 5. **Bottom Right**: Lab spectra of nontronite (sampor, JB175), saponite (SapCa-1, USGS), a 50/50 mixture of nontronite (Nau-1) and magnesite (JB953), calcite (JB1458), and dolomite (JB1461) compared with spectra of units a and f.

5.7. **Fig. 7**

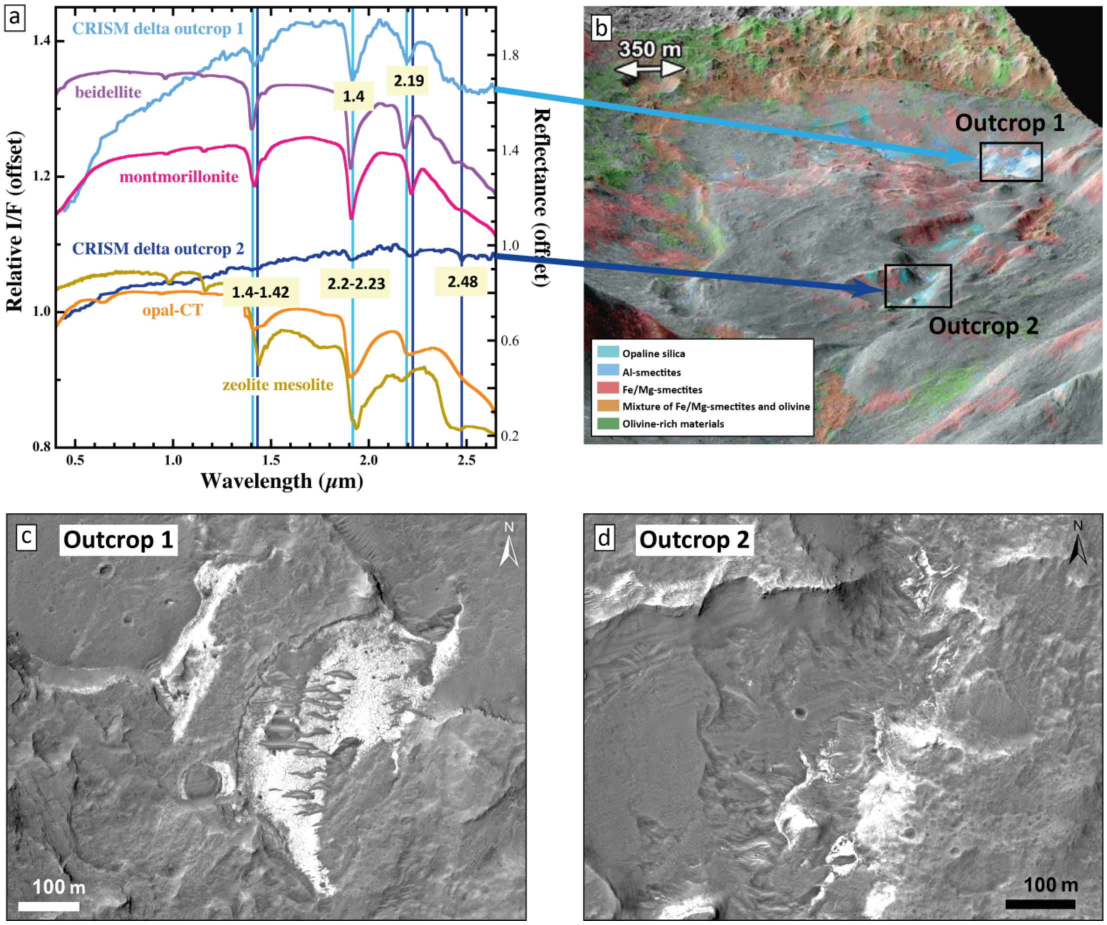

Figure 7: Two types of aqueous minerals within the fan delta at Bradbury crater. Outcrop 1 is consistent with the Al-smectite beidellite. Outcrop 2 has weaker bands and appears to contain opal. (**a**): CRISM near-infrared I/F spectra compared with relevant library mineral spectra. (**b**): Perspective view of the fan delta prepared with CRISM IR-RGB composite onto CTX imagery and HRSC topography. North is up. Image width is about 10 km. **(c):** HiRISE close-up of outcrop 1 revealing a polygonal fraction pattern in the bright Al-smectite-bearing deposit (cf., Erkeling et al., 2012). (**d**): HiRISE close-up of outcrop 2 showing that these opal-containing units are scattered in patches along a small canyon wall but do also align with some discrete bright layers on the floor of this small canyon.

5.8. **Fig. 8**

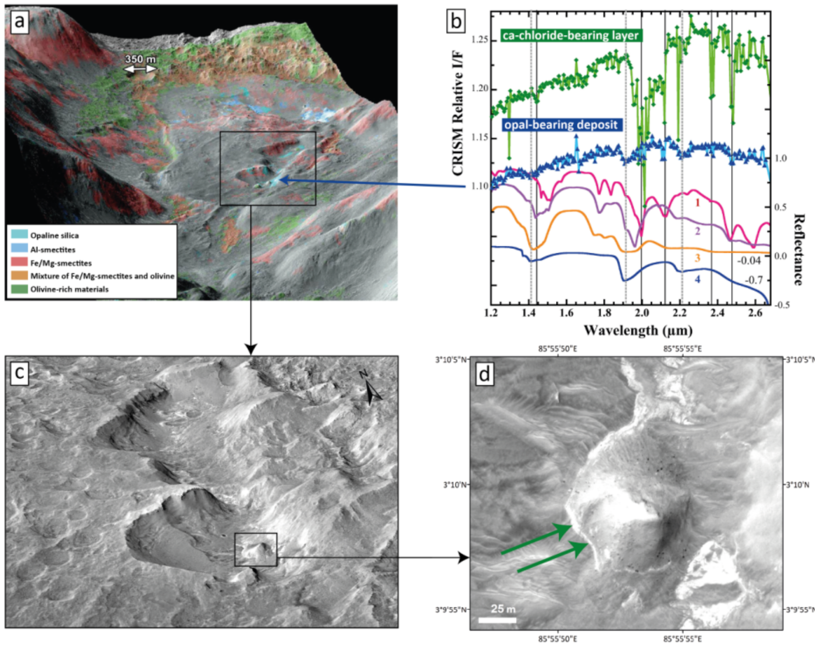

Figure 8: Calcium-chloride detected within the opal-bearing outcrop within the fan delta at the Bradbury region. (a): HiRISE perspective view of the entire fan-shaped deposit colored with CRISM spectral summary parameters R(D2300), G(OLINDEX3), B(BD2190). Vertical exaggeration is set to 3. Box indicates location of panel (c). Arrow indicates position of nob shown in panel (d) and origin of spectra in panel (b). (HiRISE red image PSP_007727_1830 onto HiRISE DTM DTEEC_007727_1830_008808_1830_A01) (b): CRISM relative I/F spectra of the opal-bearing outcrop (blue) and the bright, thin ridge (green) within nob above opal-bearing outcrop compared to reflectance spectra of lab minerals (1=CaCl2•2H2O (JB1630), 2= CaCl2•6H2O (JB1631), 3=Ca(ClO4)2•4H2O (JB984), 4=opal-CT (JB874). Features near 1.44, 1.99, 2.12, 2.37, and 2.48 μm (solid lines are similar to features found in spectra of Ca-chloride-bearing salts and features near 1.41, 2.21, and 2.21 μm (broken lines) are characteristic of opal. (**c**): HiRISE perspective view of the closer area showing the location of the nob inside a longitudinal depression. Box indicates location of panel (d). North is to the upper left. Image width is about 1.3 km. (HiRISE red image PSP_007727_1830 onto HiRISE DTM DTEEC_007727_1830_008808_1830_A01). (**d**): HiRISE close-up of nob showing the thin bright layer of Ca-chloride-bearing material (arrows).

5.9. **Fig. 9**

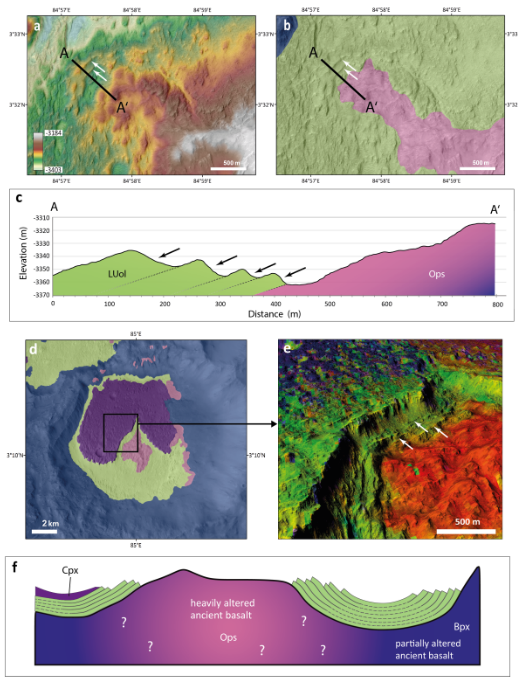

Figure 9: Imagery and sketches showing the lamination (black and white arrows) of the olivine-rich layered unit (LUol) that superposes phyllosilicate-rich outcrops (Ops). (**a**): Geologic contact of the two units north of Hashir crater. HiRISE image overlain by a color-coded HiRISE DTM (DTEED_043264_1835_042763_1835) with profile line associated with panel (c). (**b**): Same as panel (a), but with HiRISE overlain by spectro-morphological mapping and profile line. (**c**): Geological profile A-A' derived from HiRISE DTM. Measured layer thicknesses range between ~77 and ~28 m at this site. (**d**): Mapping of LUol and Ops onto CTX imagery in Hashir crater. Black box indicates location of panel (e). (**e**): Perspective view of the central peak of Hashir crater overlain by LUol showing tilted layers cropping out (combination of CRISM spectral summary parameter (R: D2300, G: OLINDEX, B: LCP), HiRISE red channel and stereo-derived DTM DTEEC_002756_1830_002822_1830_A01). North is up. Vertical enhancement is set to 3. (**f**): Simplified sketch clarifying the regional topographic relationships of the individual units (see Figure 5 for units legend).

5.10. **Fig. 10**

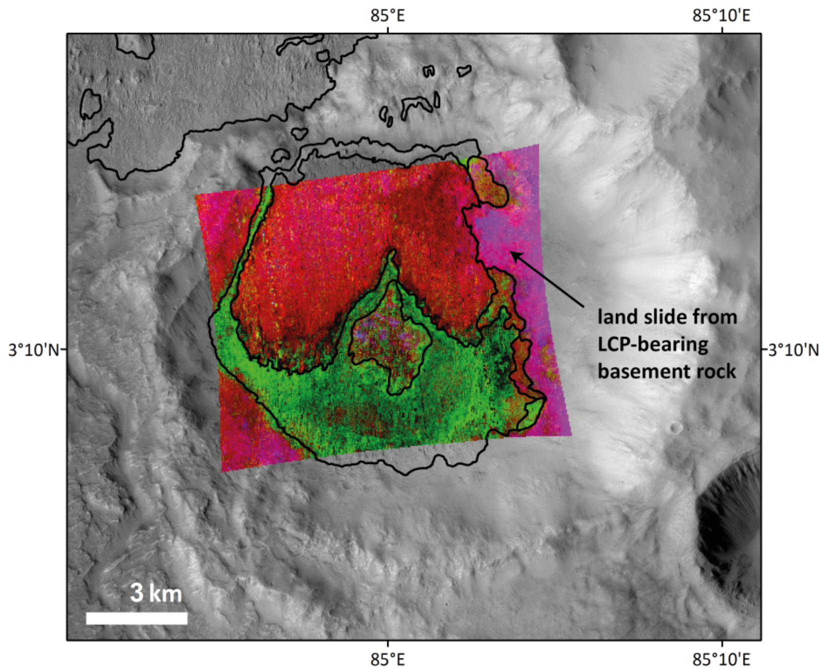

Figure 10: CRISM map of Hashir crater showing the spectral difference between the HCP-bearing caprock material (Cpx, red) that covers the LUol unit onto the crater floor (green) and the LCP-bearing basement rock (Bpx, magenta) of the Libya Montes massif to the east (right) (CRISM MTRDR spectral parameter map of HRS0000478 with R: HCPINDEX, G: OLINDEX, B: LCPINDEX overlain onto CTX imagery). Black solid lines correspond to outlines of mapping units.

5.11. **Fig. 11**

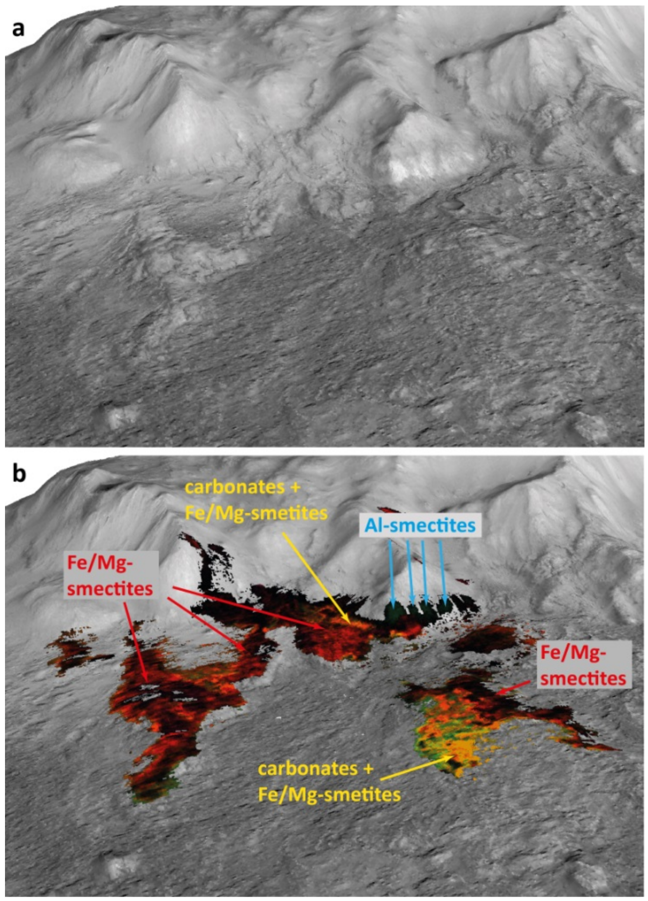

Figure 11: Location of mineral outcrops at the Hashir region as mapped from CRISM IR parameter products. Fe/Mg-smectites are shown in red, carbonates intermixed with Fe/Mg-smectites are shown in yellow and Al-smectites (beidellite in this case) are shown in blue. (**a**): Perspective view with mosaicked CTX imagery overlain onto HRSC topography. (**b**): CRISM spectral parameter map of FRT0000A819 (R: D2300, G: OLINDEX, B: LCPINDEX, see color mixing wheel in Figure 2 for mineral mixtures) overlain onto CTX imagery and HRSC topography. Perspective view with CTX imagery overlain onto HRSC topography. North is to the left, image width is about 12 km.

5.12. **Fig. 12**

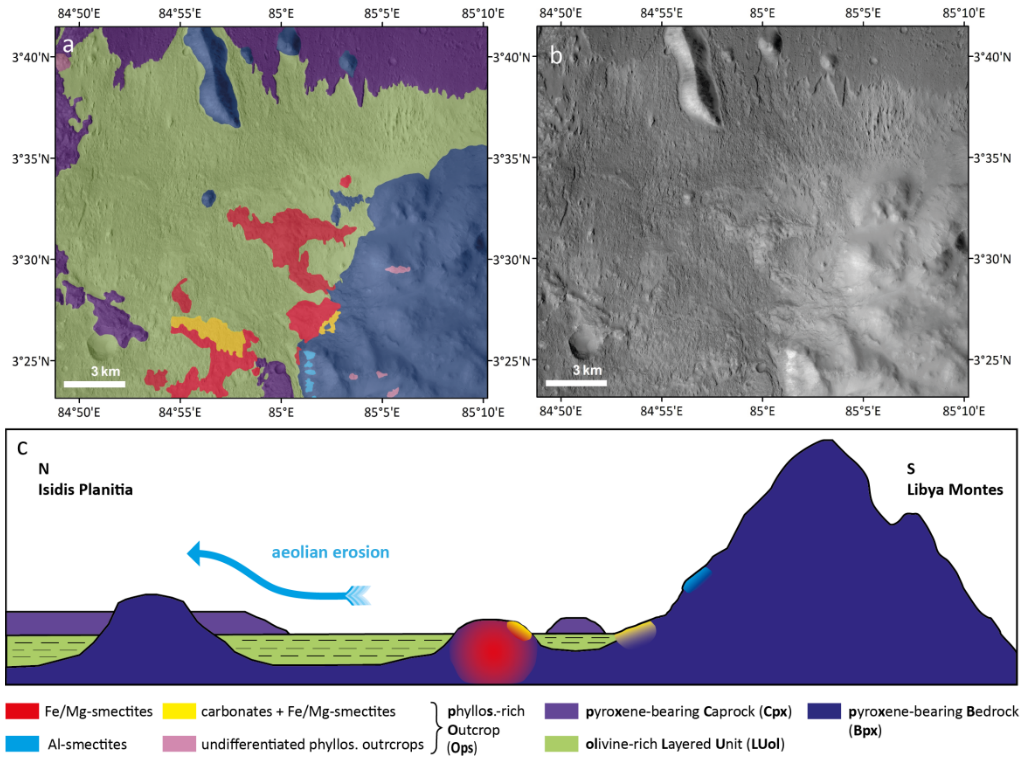

Figure 12: Geologic relationship of the individual mapping units at the Hashir region. (**a + b**): Morphological mapping and CTX view of the eastern region. (**c**): Simplified sketch (no real cross section) signifying the interpreted geological relationships of the units.

5.13. **Fig. 13**

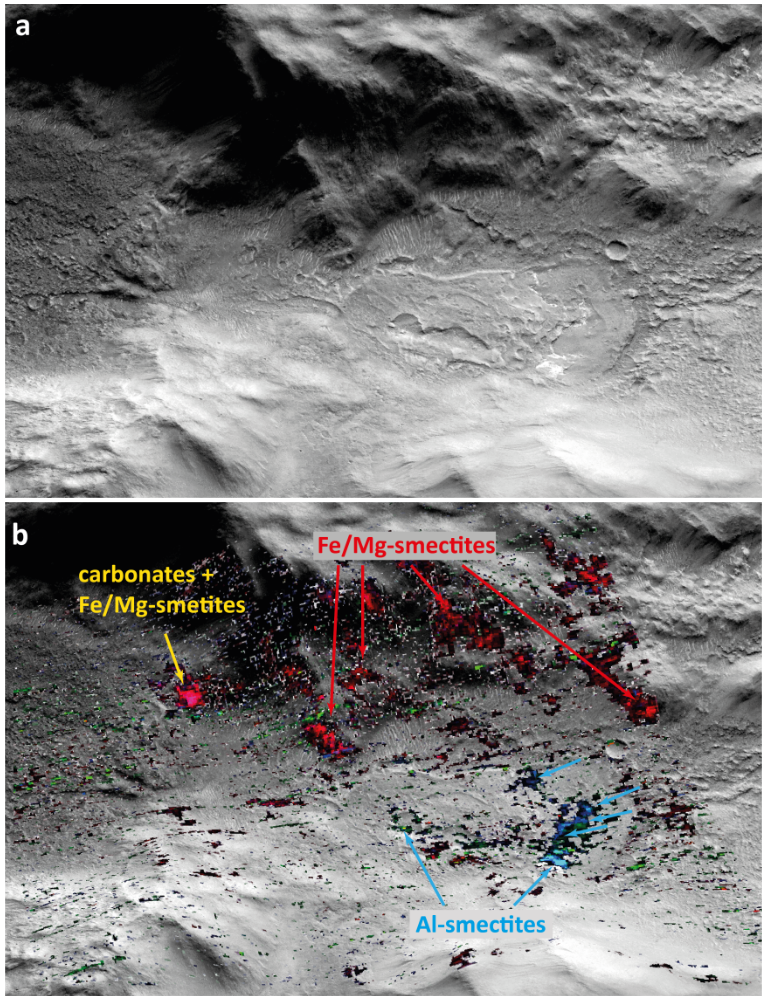

Figure 13: Location of mineral outcrops at the Bradbury region as mapped from CRISM IR parameter products. Fe/Mg-smectites are shown in red, carbonates intermixed with Fe/Mg-smectites are shown in yellow and Al-smectites (beidellite in this case) are shown in blue. (**a**): Perspective view with mosaicked CTX imagery overlain onto HRSC topography. (**b**): CRISM spectral parameter map of FRT0000BC0CB (R: D2300, G: OLINDEX, B: LCPINDEX) overlain onto CTX imagery and HRSC topography. North is to the right; image width is about 13.5 km. The fan-shaped deposit is about 5 km long and 3 km wide at its broadest part.

5.14. **Fig. 14**

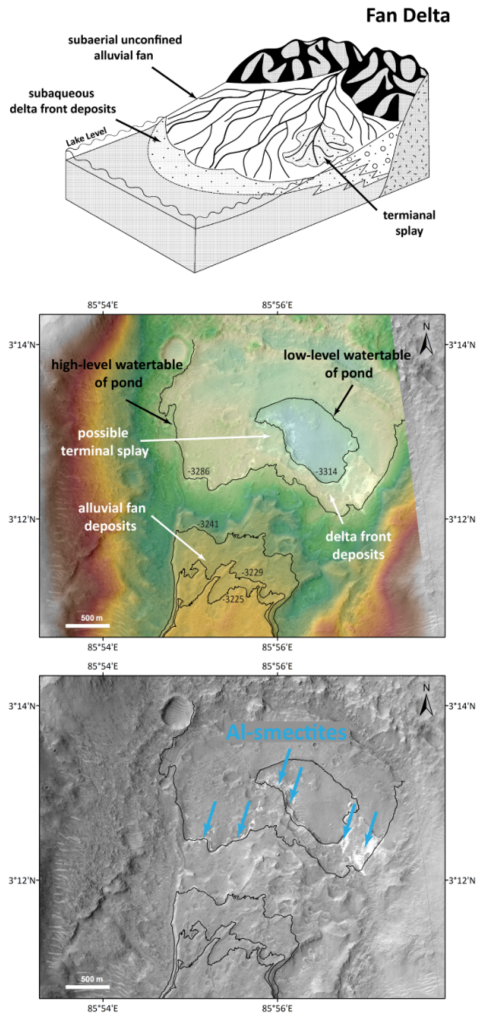

Figure 14: **Top**: Schematic sketch of a fan delta (after Nemec and Steel (1988) and Boggs (2006), modified). **Middle**: Fan delta at Bradbury crater with labelled morphological units, possible lake level stands and contour lines. HiRISE image and color-coded DTM DTEEC_007727_1830_008808_1830). **Bottom**: Fan delta at Bradbury crater showing the location of the Al-smectites (HiRISE image with same contour lines as middle panel).

5.15. **Fig. 15**

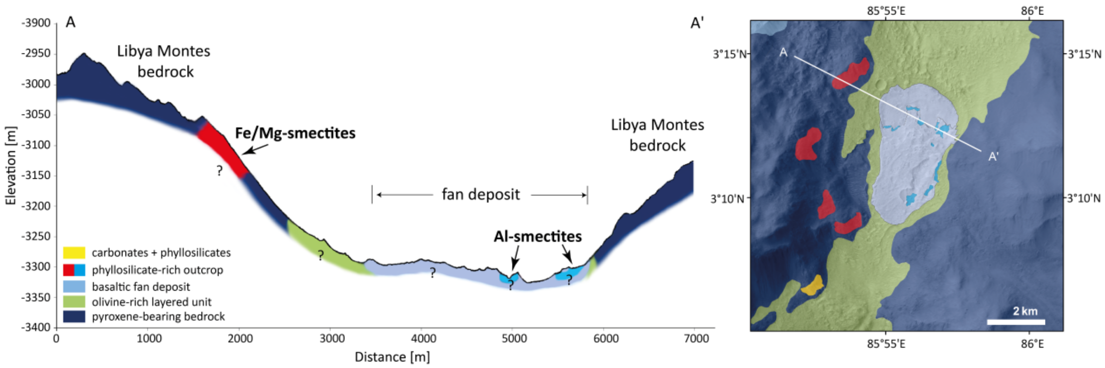

Figure 15: **Left**: Interpretive geologic cross section through the fan delta at Bradbury crater from northwest (A) to southeast (A') visualizing the topographic position of hydrated mineral outcrops. Fe/Mg-smectites are exposed along the walls of the ancient pyroxene-rich bedrock. Al-smectites crop out from the fan delta in the topographically lowest regions. Topographic data derived from HiRISE DTM DTEEC_016034_1835_017089_1835_A01. **Right**: CTX overlain by mapping and profile line.

5.16. **Fig. 16**

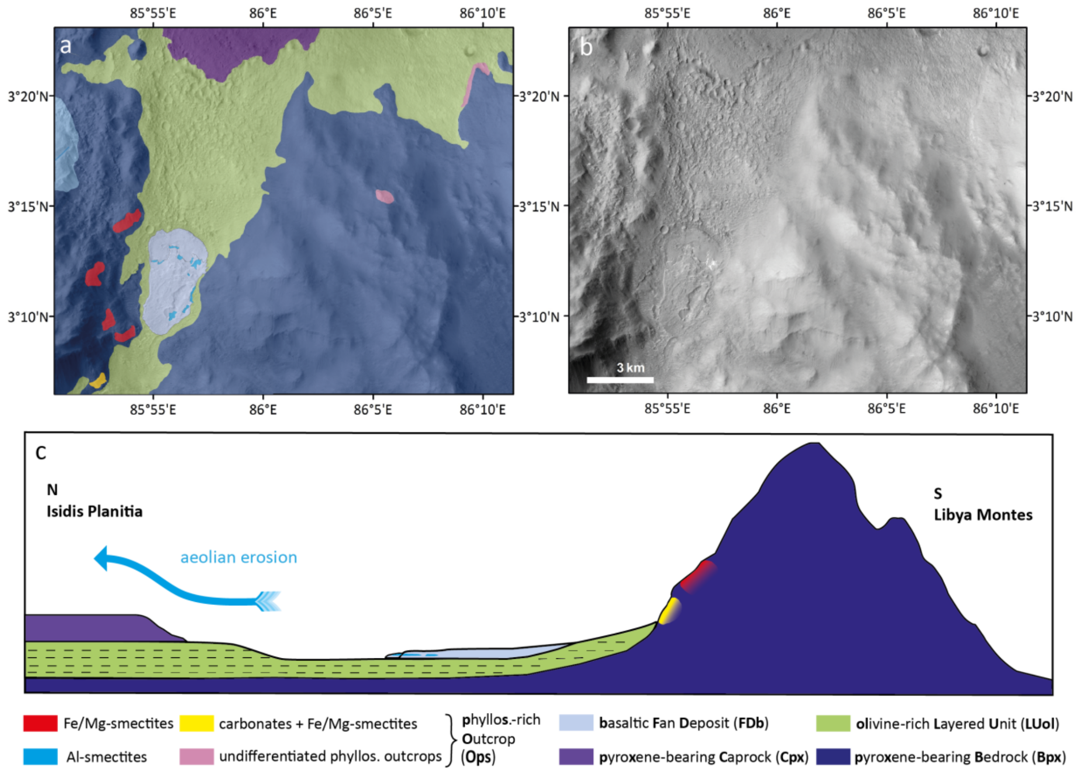

Figure 16: Geologic relationship of the individual mapping units at the Bradbury region. (**a + b**): Morphological mapping and CTX view of the Bradbury region. (**c**): Simplified cartoon (no real cross section) showing the interpreted geologic setting of this region.

5.17. **Fig. 17**

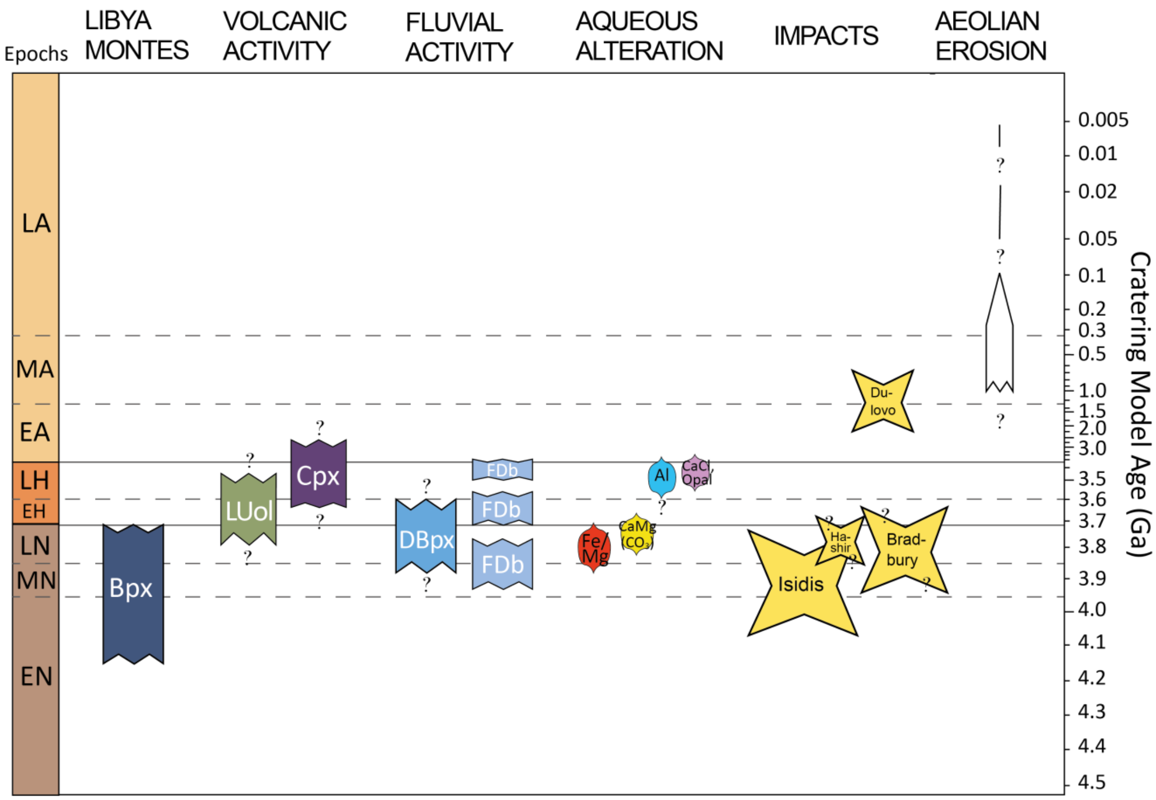

Figure 17: Sequence and relative timing of geological events in the study region. Martian epoch boundaries calculated by Michael (2013) following the Neukum chronology system (Hartmann and Neukum, 2001; Ivanov, 2001) derived from reference crater densities (Tanaka, 1986; Tanaka et al., 2005; Werner and Tanaka, 2011). Relative ages of individual emplacement, impact, erosion, and alteration events are based on the conclusions made in this study and were completed by results from Bishop et al. (2013b), Erleking et al. (2018) and Ritzer and Hauck (2009).

Tables

Table 1: List of remote sensing data used in this study.

Sensor	Image ID	Image type	Acquisition Date	Latitude	Longitude
HRSC	h0047_0000	nd + dtm	2004-01-24	-10.0826	81.9993
HRSC	h0922_0000	nd + dtm	2004-10-07	2.16756	81.3282
HRSC	h0933_0000	nd + dtm	2004-10-11	2.67795	80.2944
HRSC	h0944_0009	nd + dtm	2004-10-14	0.786927	79.2526
HRSC	h1226_0000	nd + dtm	2005-01-01	6.71835	89.681
HRSC	h2162_0002	nd + dtm	2005-09-20	2.02247	85.8429
HRSC	h2206_0002	nd + dtm	2005-10-02	1.69022	82.7402
HRSC	h3285_0000	nd + dtm	2006-07-31	-0.072572	84.4921
HRSC	h5072_0000	nd + dtm	2007-15-14	10.6031	85.3749
HRSC	h5144_0000	nd + dtm	2008-01-03	11.9235	84.7089
HRSC	h5162_0000	nd + dtm	2008-01-08	12.1713	83.7834
HRSC	h5180_0000	nd + dtm	2008-13-01	12.2356	82.849
HRSC	h7396_0001	nd + dtm	2009-10-08	-1.01902	87.7522
HRSC	h7421_0001	nd + dtm	2009-10-15	-856198	86.2331
HRSC	ha460_0000	nd + dtm	2012-03-17	-7.34795	89.5928
CRISM	FRT00003B63	S + L	2007-002	3.589735	84.11816
CRISM	FRT00007F47	S + L	2007-272	3.71798	84.89209
CRISM	FRT000085D7	S + L	2007-295	3.340555	86.168895
CRISM	FRT00008CA3	S + L	2007-351	3.51597	86.317135
CRISM	FRT00009657	S + L	2008-013	3.470215	86.118605
CRISM	FRT00009A01	S + L	2008-025	3.5397	86.455995
CRISM	FRT0000A542	S + L	2008-069	3.74187	84.85148
CRISM	FRT0000A819	S + L	2008-108	3.45631	85.013215
CRISM	FRT0000B0CB	S + L	2008-164	3.160725	85.935855
CRISM	FRT0000BC7D	S + L	2008-209	3.704	85.129355
CRISM	FRT0000CE72	S + L	2008-286	3.69723	84.65529
CRISM	FRT0001647D	S + L	2010-034	3.306055	85.01772
CRISM	FRT0001754F	S + L	2010-079	3.47304	85.074285
CRISM	FRT0001802B	S + L	2010-106	3.52736	84.701335
CRISM	FRT00018800	S + L	2010-123	3.227855	84.569695
CRISM	FRT00019568	S + L	2010-167	2.73913	84.71896

CRISM	FRT0001E2F2	S + L	2011-139	2.84276	85.767195
CRISM	FRT0001EB06	S + L	2011-172	3.57387	84.446425
CRISM	FRT0001ECEC	S + L	2011-183	2.77942	85.595785
CRISM	FRT0001FDD7	S + L	2011-239	3.455755	85.96124
CRISM	FRT00020397	S + L	2011-255	3.540045	86.009395
CRISM	FRT00020BC6	S + L	2011-288	3.697325	85.63859
CRISM	FRT00021CD0	S + L	2011-343	3.658455	85.9515
CRISM	FRT000235CA	S + L	2011-061	3.805415	84.974545
CRISM	FRT000240DF	S + L	2012-008	2.967615	85.87767
CRISM	FRT00024284	S + L	2012-094	3.541745	84.8743
CRISM	FRT0002459B	S + L	2012-105	3.84613	85.91712
CRISM	FRT00024AE2	S + L	2012-121	3.612025	84.920365
CRISM	HRS000047D8 (TRR3 and MTRDR)	S + L	2007-058	3.187655	85.007905
CRISM	HRS00011AD0	S + L	2009-080	3.635415	85.333595
CRISM	HRS0001EC08	S + L	2011-178	3.628915	85.91098
CTX	B22_018368_1824_XN_02N275W		2010-06-27	2.48	84.75
CTX	G11_022548_1828_XN_02N274W		2011-05-19	2.84	85.76
CTX	G14_023682_1827_XN_02N274W		2011-08-15	2.79	85.91
CTX	P02_001833_1827_XN_02N275W		2006-12-17	2.77	84.46
CTX	P04_002545_1839_XI_03N274W		2007-02-10	3.95	85.40
CTX	P04_002756_1826_XI_02N275W		2007-02-27	2.60	85.07
CTX	P05_002822_1822_XI_02N275W		2007-03-04	2.40	85.07
CTX	P12_005802_1819_XN_01N273W		2007-10-22	1.99	86.33
CTX	P13_006158_1821_XN_02N273W		2007-11-19	2.16	86.48
CTX	P14_006580_1822_XN_02N275W		2007-12-22	2.26	84.39
CTX	P16_007226_1809_XN_00N274W		2008-02-10	0.90	85.69
CTX	P17_007727_1814_XN_01N273W		2008-03-20	1.53	86.12
CTX	P20_008874_1822_XN_02N276W		2008-06-17	2.25	84.09
CTX	P20_009019_1829_XN_02N275W		2008-06-29	2.98	84.70
HiRISE	DTEEC_002756_1830_002800_1830_A01	DTM		see input images	
HiRISE	DTEEC_007727_1830_008808_1830_A01	DTM		see input images	
HiRISE	DTEEC_016034_1835_017089_1835_A01	DTM		see input images	
HiRISE	DTEED_043264_1835_042763_1835_A01	DTM		see input images	
HiRISE	PSP_002822_1830	red + color	2007-03-04	2.9746	83.3671
HiRISE	ESP_017089_1835	red + color	2007-03-20	3.4124	84.6476

HiRISE	ESP_022337_1830	red + color	2011-05-03	2.8146	85.8892
HiRISE	ESP_022548_1830	red + color	2011-05-19	2.7989	85.5075
HiRISE	PSP_002756_1830	red + color	2007-02-27	3.2064	85.2318
HiRISE	PSP_007727_1830	red + color	2008-03-20	3.0933	85.4498
HIRSIE	ESP_016522_1835	red + color	2010-02-03	3.2208	84.3871
HIRISE	ESP_016034_1835	red + color	2009-12-27	3.7173	87.1385

Table 2: Geomorphological mapping units of this study.

Symbol	Unit Name	Description	Interpretation
Bpx	**p**yro**x**ene-bearing **B**edrock	sharp mountain ridges with high topography differences and steep and rugged slopes	high mountainous massif, remnants of Isidis impact rim
DBpx	**p**yro**x**ene-bearing **D**issected **B**edrock	surfaces that are dissected by narrow parallel valleys that are partially degraded and incise deeply into the rocks	fluvially eroded highland terrains; part of Bpx
LUol	**ol**ivine-rich **L**ayered **U**nit	strongly eroded, layered unit featuring grooves; superposed onto Bpx and below Cpx	volcanic origin; probably from Syrtis Major (lava flows or air fall deposits)
Cpx	**p**yro**x**ene-bearing **C**aprock	surface smoother than LUol but with numerous small craters; widespread capping unit superposing LUol, patchy to the south	volcanic origin; probably from later stages of Syrtis Major activity
FDb	**b**asaltic **F**an **D**eposit	sedimentary fan-shaped deposits at the Bradbury region	two alluvial fans and one fan delta
Ops	**p**hyllo**s**ilicate-rich **O**utcrop	Fe/Mg-smectites, Al-smectites and carbonates at various locations	aqueously altered basements rocks
Solpx	**ol**ivine- and **p**yro**x**ene-rich	sand piles on the floor of Dulovo crater and a	dark aeolian sediments

Sand	dark linear feature cropping out at the crater wall; high olivine- and pyroxene signature	accumulated as sand dunes and its local sediment source exposed at the crater wall

References

Abramov, O., Kring, D.A., 2005. Impact-induced hydrothermal activity on early Mars. Journal of Geophysical Research (Planets), 110, 10.1029/2005JE002453.

Amador, E.S., Bandfield, J.L., 2016. Elevated bulk-silica exposures and evidence for multiple aqueous alteration episodes in Nili Fossae, Mars. Icarus, 276, 39-51, doi: 10.1016/j.icarus.2016.04.015.

Balme, M., Berman, D.C., Bourke, M.C., Zimbelman, J.R., 2008. Transverse Aeolian Ridges (TARs) on Mars. Geomorphology, 101, 703-720.

Baratoux, D., Toplis, M.J., Monnereau, M., Sautter, V., 2013. The petrological expression of early Mars volcanism. Journal of Geophysical Research: Planets, 118, 59-64, doi: 10.1029/2012JE004234.

Bishop, J.L., Noe Dobrea, E.Z., McKeown, N.K., Parente, M., Ehlmann, B.L., Michalski, J.R., Milliken, R.E., Poulet, F., Swayze, G.A., Mustard, J.F., Murchie, S.L., Bibring, J.-P., 2008. Phyllosilicate Diversity and Past Aqueous Activity Revealed at Mawrth Vallis, Mars. Science, 321, 830-833, doi: 10.1126/science.1159699.

Bishop, J.L., Gates, W.P., Makarewicz, H.D., McKeown, N.K., Hiroi, T., 2011. Reflectance Spectroscopy of Beidellites and their Importance for Mars. Clays and Clay Minerals, 59, 378-399, doi: 10.1346/ccmn.2011.0590403.

Bishop, J.L., Perry, K.A., Darby Dyar, M., Bristow, T.F., Blake, D.F., Brown, A.J., Peel, S.E., 2013a. Coordinated spectral and XRD analyses of magnesite-nontronite-forsterite mixtures and implications for carbonates on Mars. Journal of Geophysical Research (Planets), 118, 635-650.

Bishop, J.L., Tirsch, D., Tornabene, L.L., Jaumann, R., McEwen, A.S., McGuire, P.C., Ody, A., Poulet, F., Clark, R.N., Parente, M., McKeown, N.K., Mustard, J.F., Murchie, S.L., Voigt, J., Aydin, Z., Bamberg, M., Petau, A., Michael, G., Seelos, F., Hash, C., Swayze, G., Neukum, G., 2013b. Mineralogy and morphology of geologic units at Libya Montes, Mars: Ancient aqueously derived outcrops, mafic flows, fluvial features and impacts. Journal of Geophysical Research (Planets), 118, 487-513, doi: 10.1029/2012JE004151.

Bishop, J.L., Tirsch, D., Tornabene, L.L., Jaumann, R., McEwen, A.S., McGuire, P.C., Ody, A., Poulet, F., Clark, R.N., Parente, M., McKeown, N.K., Mustard, J.F., Murchie, S.L., Voigt, J., Aydin, Z., Bamberg, M., Petau, A., Michael, G., Seelos, F.P., Hash, C.D., Swayze, G.A., Neukum, G., 2013c. Mineralogy and morphology of geologic units at Libya Montes, Mars: Ancient aqueously derived outcrops, mafic flows, fluvial features, and impacts. Journal of Geophysical Research (Planets), 118, 487-513.

Bishop, J.L., Quinn, R., Darby Dyar, M., 2014. Spectral and thermal properties of perchlorate salts and implications for Mars. American Mineralogist, 99, 1580-1592, doi: 10.2138/am.2014.4707.

Bishop, J.L., Davila, A., Hanley, J., Roush, T.L., 2016. Dehydration-Rehydration Experiments with Cl Salts Mixed into Mars Analog Materials and the Effects on their VNIR Spectral Properties, Lunar and Planetary Science Conference Abstracts, p. 1645.

Bishop, J.L., Fairén, A.G., Michalski, J.R., Gago-Duport, L., Baker, L.L., Velbel, M.A., Gross, C., Rampe, E.B., 2018. Surface clay formation during short-term warmer and wetter conditions on a largely cold ancient Mars. Nature Astronomy, doi: 10.1038/s41550-017-0377-9.
Boggs, S., 2006. Principles of Sedimentology and Stratigraphy, 4 ed. Pearson Prentice Hall, New Jersey.
Bramble, M.S., Goudge, T.A., Milliken, R.E., Mustard, J.F., 2017a. Testing the Deltaic Origin of Fan Deposits at Bradbury Crater, Mars, Lunar and Planetary Science Conference.
Bramble, M.S., Mustard, J.F., Salvatore, M.R., 2017b. The geological history of Northeast Syrtis Major, Mars. Icarus, 293, 66-93, doi: 10.1016/j.icarus.2017.03.030.
Brown, A.J., Hook, S.J., Baldridge, A.M., Crowley, J.K., Bridges, N.T., Thomson, B.J., Marion, G.M., de Souza Filho, C.R., Bishop, J.L., 2010. Hydrothermal formation of Clay-Carbonate alteration assemblages in the Nili Fossae region of Mars. Earth and Planetary Science Letters, 297, 174-182, doi: 10.1016/j.epsl.2010.06.018.
Burr, D.M., Williams, R.M.E., Wendell, K.D., Chojnacki, M., Emery, J.P., 2010. Inverted fluvial features in the Aeolis/Zephyria Plana region, Mars: Formation mechanism and initial paleodischarge estimates. Journal of Geophysical Research: Planets, 115, doi: 10.1029/2009JE003496.
Cannon, K.M., Parman, S.W., Mustard, J.F., 2017. Primordial clays on Mars formed beneath a steam or supercritical atmosphere. Nature, 552, 88, doi: 10.1038/nature24657.
Carter, J., Loizeau, D., Mangold, N., Poulet, F., Bibring, J.-P., 2015. Widespread surface weathering on early Mars: A case for a warmer and wetter climate. Icarus, 248, 373-382, 10.1016/j.icarus.2014.11.011.
Crumpler, L.S., Tanaka, K.L., 2003. Geology and MER target site characteristics along the southern rim of Isidis Planitia, Mars. Journal of Geophysical Research(Planets), 108, 8080, doi: 10.1029/2002JE002040.
Davis, J.M., Balme, M., Grindrod, P.M., Williams, R.M.E., Gupta, S., 2016. Extensive Noachian fluvial systems in Arabia Terra: Implications for early Martian climate. Geology, 44, 847-850, doi: 10.1130/G38247.1.
Dury, G.H., Ritter, D.F., Schumm, S.A., Lustig, L.K., 2009. River: Classification of Deltas, Encyclopedia Britannica. Scholastic, Pittsburgh.
Edwards, C.S., Christensen, P.R., 2011. Evidence for a Widespread Olivine-Rich Layer on Mars: Identification of a Global Impact Ejecta Deposit?, 42nd Lunar Planet. Sci. Conf., The Woodlands, TX, p. abs. #1608.
Ehlmann, B.L., Mustard, J.F., Murchie, S.L., Poulet, F., Bishop, J.L., Brown, A.J., Calvin, W.M., Clark, R.N., Des Marais, D.J., Milliken, R.E., Roach, L.H., Roush, T.L., Swayze, G.A., Wray, J.J., 2008a. Orbital Identification of Carbonate-Bearing Rocks on Mars. Science, 322, 1828-1832.
Ehlmann, B.L., Mustard, J.F., Swayze, G.A., Wray, J.J., Barnouin-Jha, O.S., Bishop, J.L., Des Marais, D.J., Poulet, F., Roach, L.H., Milliken, R.E., Clark, R.N., Murchie, S.L., and the MRO CRISM Team, 2008b. Phyllosilicates, Zeolites, and Carbonate

Near Nili Fossae, Mars: Evidence for Distinct Environments of Aqueous Alteration, LPI Contributions, pp. 33-34.

Ehlmann, B.L., Mustard, J.F., Swayze, G.A., Clark, R.N., Bishop, J.L., Poulet, F., Des Marais, D.J., Roach, L.H., Milliken, R.E., Wray, J.J., Barnouin-Jha, O.S., Murchie, S.L., 2009. Identification of hydrated silicate minerals on Mars using MRO-CRISM: Geologic context near Nili Fossae and implications for aqueous alteration. Journal of Geophysical Research (Planets), 114, 10.1029/2009JE003339.

Ehlmann, B.L., Mustard, J.F., Murchie, S.L., 2010. Geologic setting of serpentine deposits on Mars. Geophysical Research Letters, 37, doi: 10.1029/2010GL042596.

Ehlmann, B.L., Mustard, J.F., Murchie, S.L., Bibring, J.-P., Meunier, A., Fraeman, A.A., Langevin, Y., 2011. Subsurface water and clay mineral formation during the early history of Mars. Nature, 479, 53-60, 10.1038/nature10582.

Ehlmann, B.L., Mustard, J.F., 2012. An in-situ record of major environmental transitions on early Mars at Northeast Syrtis Major. Geophysical Research Letters, 39, L11202, doi: 10.1029/2012gl051594.

Erkeling, G., Reiss, D., Hiesinger, H., Jaumann, R., 2010a. Morphologic, stratigraphic and morphometric investigations of valley networks in eastern Libya Montes, Mars: Implications for the Noachian / Hesperian climate change. Earth and Planetary Science Letters, 294, 291-305, 10.1016/j.epsl.2009.08.008.

Erkeling, G., Reiss, D., Hiesinger, H., Jaumann, R., 2010b. Morphologic, stratigraphic and morphometric investigations of valley networks in eastern Libya Montes, Mars: Implications for the Noachian/Hesperian climate change. Earth and Planetary Sci. Lett., 294, 291-305, doi:10.1016/j.epsl.2009.08.008

Erkeling, G., Reiss, D., Hiesinger, H., Poulet, F., Carter, J., Ivanov, M.A., Hauber, E., Jaumann, R., 2012. Valleys, paleolakes and possible shorelines at the Libya Montes/Isidis boundary: Implications for the hydrologic evolution of Mars. Icarus, 219, 393-413, doi: 10.1016/j.icarus.2012.03.012.

Erkeling, G., Ivanov, M.A., Reiss, D., Hiesinger, H., Bishop, J.L., Tirsch, D., Jaumann, R., Tornabene, L.L., Ruesch, O., 2015. Valleys, Fan-Shaped Deposits and Associated Phyllosilicates of a Paleolake Site at Libya Montes, Mars: Evidence of Complex Hydrologic Activity, Lunar and Planetary Science Conference, p. 1779.

Erkeling, G., Ivanov, M.A., Tirsch, D., Reiss, D., Bishop, J.L., Tornabene, L.L., Hiesinger, H., Jaumann, R., 2016. Bradbury Crater, Mars: Morphology, Morphometry, Mineralogy, and Chronostratigraphy, Lunar and Planetary Science Conference, p. 1451.

Erleking, G., Ivanov, M.A., Reiss, D., Bishop, J.L., Tirsch, D., Tornabene, L.L., Hiesinger, H., Hauber, E., Jaumann, R., 2018. Aqueous geologic record of Bradbury Crater, Mars. (manuscript in preperation).

Fairén, A.G., Davila, A.F., Gago-Duport, L., Haqq-Misra, J.D., Gil, C., McKay, C.P., Kasting, J.F., 2011. Cold glacial oceans would have inhibited phyllosilicate sedimentation on early Mars. Nature Geoscience, 4, 667-670.

Fawdon, P., Skok, J.R., Balme, M.R., Vye-Brown, C.L., Rothery, D.A., Jordan, C.J., 2015. The geological history of Nili Patera, Mars. Journal of Geophysical Research: Planets, 120, 951-977, doi: 10.1002/2015JE004795.

Fawdon, P., 2016. The Volcanic Evolution of Syrtis Major Planum, Mars, PhD Thesis, The Open University.

Grauby, O., Petit, S., Decarreau, A., Baronnet, A., 1993. The beidellite-saponite series: an experimental approach (English Title: The beidellite-saponite series: an experimental approach). European Journal of Mineralogy, 5, 623-636.

Greeley, R., Guest, J.E., 1987. Geologic map of the eastern equatorial region of Mars, IMAP; USGS Miscellaneous Investigations Series Map I-1802-B, 1:15,000,000.

Guisseau, D., Patrier, P., Beaufort, D., Girard, J.-P., Inoue, A., Sanjuan, B., Petit, S., Lens, A., Genter, A., 2007. Significance of the depth-related transition montmorillonite-beidellite in the geothermal field of Bouillante (Guadeloupe, Lesser antilles). American Mineralogist, 92, 1800-1813, doi: 10.2138/am.2007.2398.

Gwinner, K., Scholten, F., Spiegel, M., Schmidt, R., Giese, B., Oberst, J., Heipke, C., Jaumann, R., Neukum, G., 2009. Derivation and Validation of High-Resolution Digital Terrain Models from Mars Express HRSC Data. Photogrammetric Engineering & Remote Sensing, 75, 1127-1142.

Gwinner, K., Scholten, F., Preusker, F., Elgner, S., Roatsch, T., Spiegel, M., Schmidt, R., Oberst, J., Jaumann, R., Heipke, C., 2010. Topography of Mars from global mapping by HRSC high-resolution digital terrain models and orthoimages: Characteristics and performance. Earth and Planetary Science Letters, 294, 506-519, doi: 10.1016/j.epsl.2009.11.007.

Hamilton, V.E., Christensen, P.R., 2005. Evidence for extensive, olivine-rich bedrock on Mars. Geology, 33, 433-436, doi: 10.1130/g21258.1.

Hanley, J., Dalton, J.B., Chevrier, V.F., Jamieson, C.S., Barrows, R.S., 2014. Reflectance spectra of hydrated chlorine salts: The effect of temperature with implications for Europa. Journal of Geophysical Research: Planets, 119, 2370-2377, doi: 10.1002/2013JE004565.

Hanley, J., Chevrier, V.F., Barrows, R.S., Swaffer, C., Altheide, T.S., 2015. Near- and mid-infrared reflectance spectra of hydrated oxychlorine salts with implications for Mars. Journal of Geophysical Research: Planets, 120, 1415-1426, doi: 10.1002/2013JE004575.

Hartmann, W.K., Neukum, G., 2001. Cratering chronology and the evolution of Mars. Space Science Reviews, 96, 165-194.

Hoefen, T.M., Clark, R.N., Bandfield, J.L., Smith, M.D., Pearl, J.C., Christensen, P.R., 2003. Discovery of olivine in the Nili Fossae region of Mars. Science, 302, 627-630.

Huertas, F.J., 2000. Experimental study of the hydrothermal formation of smectite in the beidellite-saponite series. American Journal of Science, 300, 504-527, doi: 10.2475/ajs.300.6.504.

Hynek, B.M., Beach, M., Hoke, M.R.T., 2010. Updated global map of Martian valley networks and implications for climate and hydrologic processes. Journal of Geophysical Research (Planets), 115, 9008, 10.1029/2009JE003548.

Ivanov, B.A., 2001. Mars/Moon cratering rate ratio estimates. Chronology and Evolution of Mars, 96, 87-104.

Ivanov, M.A., Hiesinger, H., Erkeling, G., Hielscher, F.J., Reiss, D., 2012. Major episodes of geologic history of Isidis Planitia on Mars. Icarus, 218, 24-46, doi: 10.1016/j.icarus.2011.11.029.

Ivanov, M.A., Hiesinger, H., Erkeling, G., Reiss, D., 2014. Mud volcanism and morphology of impact craters in Utopia Planitia on Mars: Evidence for the ancient ocean. Icarus, 228, 121-140, doi: 10.1016/j.icarus.2013.09.018.

Jaumann, R., Neukum, G., Behnke, T., Duxbury, T.C., Eichentopf, K., Flohrer, J., Gasselt, S.v., Giese, B., Gwinner, K., Hauber, E., Hoffmann, H., Hoffmeister, A., Köhler, U., Matz, K.-D., McCord, T.B., Mertens, V., Oberst, J., Pischel, R., Reiss, D., Ress, E., Roatsch, T., Saiger, P., Saiger, F., Scholten, F., Schwarz, G., Stephan, K., Wählisch, M., the HRSC Co-Investigator Team, 2007. The high-resolution stereo camera (HRSC) experiment on Mars Express: Instrument aspects and experiment conduct from interplanetary cruise through the nominal mission. Planetary and Space Science, 55, 928-952.

Jaumann, R., Nass, A., Tirsch, D., Reiss, D., Neukum, G., 2010. The Western Libya Montes Valley System on Mars: Evidence for episodic and multi-genetic erosion events during the Martian history. Earth and Planetary Science Letters, 294, 272-290, doi: 10.1016/j.epsl.2009.09.026.

Kirk, R.L., Howington-Kraus, E., Rosiek, M.R., Anderson, J.A., Archinal, B.A., Becker, K.J., Cook, D.A., Galuszka, D.M., Geissler, P.E., Hare, T.M., Holmberg, I.M., Keszthelyi, L.P., Redding, B.L., Delamere, W.A., Gallagher, D., Chapel, J.D., Eliason, E.M., King, R., McEwen, A.S., 2008. Ultrahigh resolution topographic mapping of Mars with MRO HiRISE stereo images: Meter-scale slopes of candidate Phoenix landing sites. Journal of Geophysical Research, 113, E00A24, doi: 10.1029/2007JE003000.

Kremer, C.H., Mustard, J.F., Bramble, M.S., 2018. Origin and emplacement of the circum-Isidis olivine-rich unit, Lunar and Planetary Science Concerence Abstacts p. 1545.

Loizeau, D., Mangold, N., Poulet, F., Bibring, J.P., Gendrin, A., Ansan, V., Gomez, C., Gondet, B., Langevin, Y., Masson, P., Neukum, G., 2007. Phyllosilicates in the Mawrth Vallis region of Mars. Journal of Geophysical Research(Planets), 112, doi: 10.1029/2006JE002877.

Loizeau, D., Mangold, N., Poulet, F., Ansan, V., Hauber, E., Bibring, J.P., Gondet, B., Langevin, Y., Masson, P., Neukum, G., 2010. Stratigraphy in the Mawrth Vallis region through OMEGA, HRSC color imagery and DTM. Icarus, 205, 396-418, doi: 10.1016/j.icarus.2009.04.018.

Loizeau, D., Werner, S.C., Mangold, N., Bibring, J.P., Vago, J.L., 2012. Chronology of deposition and alteration in the Mawrth Vallis region, Mars. Planetary and Space Science, 72, 31-43, 10.1016/j.pss.2012.06.023.

Loizeau, D., Mangold, N., Poulet, F., Bibring, J.P., Bishop, J.L., Michalski, J., Quantin, C., 2015. History of the clay-rich unit at Mawrth Vallis, Mars: High-resolution mapping of a candidate landing site. Journal of Geophysical Research: Planets, 120, 1820-1846, doi: 10.1002/2015JE004894.

Malin, M.C., Bell, J.F., Cantor, B.A., Caplinger, M.A., Calvin, W.M., Clancy, R.T., Edgett, K.S., Edwards, L., Haberle, R.M., James, P.B., Lee, S.W., Ravine, M.A., Thomas, P.C., Wolff, M.J., 2007. Context Camera Investigation on board the Mars Reconnaissance Orbiter. Journal of Geophysical Research (Planets), 112, doi: 10.1029/2006JE002808.

McEwen, A.S., Eliason, E.M., Bergstrom, J.W., Bridges, N.T., Hansen, C.J., Delamere, W.A., Grant, J.A., Gulick, V.C., Herkenhoff, K.E., Keszthelyi, L.P., Kirk, R.L., Mellon, M.T., Squyres, S.W., Thomas, N., Weitz, C.M., 2007. Mars Reconnaissance Orbiter's High Resolution Imaging Science Experiment (HiRISE). Journal of Geophysical Research(Planets), 112, E05S02, doi: 10.1029/2005JE002605.

McEwen, A.S., Banks, M.E., Baugh, N., Becker, K., Boyd, A., Bergstrom, J.W., Beyer, R.A., Bortolini, E., Bridges, N.T., Byrne, S., Castalia, B., Chuang, F.C., Crumpler, L.S., Daubar, I., Davatzes, A.K., Deardorff, D.G., DeJong, A., Alan Delamere, W., Dobrea, E.N., Dundas, C.M., Eliason, E.M., Espinoza, Y., Fennema, A., Fishbaugh, K.E., Forrester, T., Geissler, P.E., Grant, J.A., Griffes, J.L., Grotzinger, J.P., Gulick, V.C., Hansen, C.J., Herkenhoff, K.E., Heyd, R., Jaeger, W.L., Jones, D., Kanefsky, B., Keszthelyi, L., King, R., Kirk, R.L., Kolb, K.J., Lasco, J., Lefort, A., Leis, R., Lewis, K.W., Martinez-Alonso, S., Mattson, S., McArthur, G., Mellon, M.T., Metz, J.M., Milazzo, M.P., Milliken, R.E., Motazedian, T., Okubo, C.H., Ortiz, A., Philippoff, A.J., Plassmann, J., Polit, A., Russell, P.S., Schaller, C., Searls, M.L., Spriggs, T., Squyres, S.W., Tarr, S., Thomas, N., Thomson, B.J., Tornabene, L.L., Van Houten, C., Verba, C., Weitz, C.M., Wray, J.J., 2010. The High Resolution Imaging Science Experiment (HiRISE) during MRO's Primary Science Phase (PSP) Icarus, 205, 2-37, doi:10.1016/j.icarus.2009.1004.1023

McGuire, P.C., Bishop, J.L., Brown, A.J., Fraeman, A.A., Marzo, G.A., Morgan, M.F., Murchie, S.L., Mustard, J.F., Parente, M., Pelkey, S.M., Roush, T.L., Seelos, F.P., Smith, M.D., Wendt, L., Wolff, M.J., 2009. An improvement to the volcano-scan algorithm for atmospheric correction of CRISM and OMEGA spectral data. Planetary and Space Science, 57, 809-815, doi: 10.1016/j.pss.2009.03.007.

Michael, G.G., 2013. Planetary surface dating from crater size–frequency distribution measurements: Multiple resurfacing episodes and differential isochron fitting. Icarus, 226, 885-890, 10.1016/j.icarus.2013.07.004.

Murchie, S., Arvidson, R., Bedini, P., Beisser, K., Bibring, J.-P., Bishop, J., Boldt, J., Cavender, P., Choo, T., Clancy, R.T., Darlington, E.H., Des Marais, D., Espiritu, R., Fort, D., Green, R., Guinness, E., Hayes, J., Hash, C., Heffernan, K., Hemmler, J., Heyler, G., Humm, D., Hutcheson, J., Izenberg, N., Lee, R., Lees, J., Lohr, D., Malaret, E., Martin, T., McGovern, J.A., McGuire, P., Morris, R., Mustard, J., Pelkey, S., Rhodes, E., Robinson, M., Roush, T., Schaefer, E., Seagrave, G., Seelos, F., Silverglate, P., Slavney, S., Smith, M., Shyong, W.-J., Strohbehn, K., Taylor, H., Thompson, P., Tossman, B., Wirzburger, M., Wolff, M., 2007. Compact Reconnaissance Imaging Spectrometer for Mars (CRISM) on Mars Reconnaissance Orbiter (MRO). Journal of Geophysical Research (Planets), 112, doi: 10.1029/2006JE002682.

Murchie, S.L., Seelos, F.P., Hash, C.D., Humm, D.C., Malaret, E., McGovern, J.A., Choo, T.H., Seelos, K.D., Buczkowski, D.L., Morgan, M.F., Barnouin-Jha, O.S., Nair, H., Taylor, H.W., Patterson, G.W., Harvel, C.A., Mustard, J.F., Arvidson, R.E., McGuire, P., Smith, M.D., Wolff, M.J., Titus, T.N., Bibring, J.-P., Poulet, F., 2009. Compact Reconnaissance Imaging Spectrometer for Mars investigation and data set from the Mars Reconnaissance Orbiter's primary science phase. Journal of Geophysical Research: Planets, 114, doi: 10.1029/2009je003344.

Murphy, N.W., Jakosky, B.M., Rafkin, S.C., Larsen, K.W., Putzig, N.E., Mellon, M.T., 2007. Thermophysical properties of the Isidis basin, Mars. Journal of Geophysical Research: Planets, 112, doi: 10.1029/2005JE002586.

Mustard, J.F., Poulet, F., Head, J.W., Mangold, N., Bibring, J.P., Pelkey, S.M., Fassett, C.I., Langevin, Y., Neukum, G., 2007. Mineralogy of the Nili Fossae region with OMEGA/Mars Express data: 1. Ancient impact melt in the Isidis Basin and implications for the transition from the Noachian to Hesperian. Journal of Geophysical Research (Planets), 112, doi: 10.1029/2006JE002834.

Mustard, J.F., Murchie, S.L., Pelkey, S.M., Ehlmann, B.L., Milliken, R.E., Grant, J.A., Bibring, J.P., Poulet, F., Bishop, J., Dobrea, E.N., Roach, L., Seelos, F., Arvidson, R.E., Wiseman, S., Green, R., Hash, C., Humm, D., Malaret, E., McGovern, J.A., Seelos, K., Clancy, T., Clark, R., Marais, D.D., Izenberg, N., Knudson, A., Langevin, Y., Martin, T., McGuire, P., Morris, R., Robinson, M., Roush, T., Smith, M., Swayze, G., Taylor, H., Titus, T., Wolff, M., 2008. Hydrated silicate minerals on Mars observed by the Mars Reconnaissance Orbiter CRISM instrument. Nature, 454, 305-309.

Mustard, J.F., Ehlmann, B.L., Murchie, S.L., Poulet, F., Mangold, N., Head, J.W., Bibring, J.-P., Roach, L.H., 2009. Composition, Morphology, and Stratigraphy of Noachian Crust around the Isidis basin. Journal of Geophysical Research (Planets), 114, doi: 10.1029/2009JE003349.

Nemec, W., Steel, R.J., 1988. What is a fan delta and how to recognize it?, In: Nemec, W., Steel, R.J. (Eds.), Fan Deltas: Sedimentology and Tectonic Settings. Blackie and Son.

Neukum, G., Jaumann, R., the HRSC Co-Investigator and Experiment Team, 2004. HRSC: the High Resolution Stereo Camera of Mars Express. ESA Special Publication, SP-1240, 1-19.

Newsom, H.E., Lanza, N.L., Ollila, A.M., Wiseman, S.M., Roush, T.L., Marzo, G.A., Tornabene, L.L., Okubo, C.H., Osterloo, M.M., Hamilton, V.E., Crumpler, L.S., 2010. Inverted channel deposits on the floor of Miyamoto crater, Mars. Icarus, 205, 64-72, doi: 10.1016/j.icarus.2009.03.030.

Oliver, J.E., Fairbridge, R.E., 2005. Mountain and Valley Winds, Encyclopedia of World Climatology. Springer Netherlands, pp. 516-517.

Osinski, G.R., Tornabene, L.L., Banerjee, N.R., Cockell, C.S., Flemming, R., Izawa, M.R.M., McCutcheon, J., Parnell, J., Preston, L.J., Pickersgill, A.E., Pontefract, A., Sapers, H.M., Southam, G., 2013. Impact-generated hydrothermal systems on Earth and Mars. Icarus, 224, 347-363, doi: 10.1016/j.icarus.2012.08.030.

Parente, M., 2008. A New Approach to Denoising CRISM Images, Lunar and Planetary Science Conference Abstacts, p. 2528.

Pelkey, S.M., Mustard, J.F., Murchie, S., Clancy, R.T., Wolff, M., Smith, M., Milliken, R., Bibring, J.P., Gendrin, A., Poulet, F., Langevin, Y., Gondet, B., 2007. CRISM multispectral summary products: Parameterizing mineral diversity on Mars from reflectance. Journal of Geophysical Research(Planets), 112, doi: 10.1029/2006JE002831.

Ritzer, J.A., Hauck, S.A., 2009. Lithospheric structure and tectonics at Isidis Planitia, Mars. Icarus, 201, 528-539, doi: 10.1016/j.icarus.2009.01.025.

Robin, V., Hebert, B., Beaufort, D., Sardini, P., Tertre, E., Regnault, O., Descostes, M., 2015. Occurrence of authigenic beidellite in the Eocene transitional sandy sediments of the Chu-Saryssu basin (South-Central Kazakhstan). Sedimentary Geology, 321, 39-48, doi: 10.1016/j.sedgeo.2015.03.004.

Schoenherr, J., Reuning, L., Kukla, P.A., Littke, R., Urai, J.L., Siemann, M., Rawahi, Z., 2009. Halite cementation and carbonate diagenesis of intra-salt reservoirs from the Late Neoproterozoic to Early Cambrian Ara Group (South Oman Salt Basin). Sedimentology, 56, 567-589, doi: 10.1111/j.1365-3091.2008.00986.x.

Scholten, F., Gwinner, K., Roatsch, T., Matz, K.D., Wählisch, M., Giese, B., Oberst, J., Jaumann, R., Neukum, G., and the HRSC Co-Investigator Team, 2005. Mars Express HRSC Data Processing - Methods and Operational Aspects. Photogrammetric Engineering and Remote Sensing, 71, 1143-1152.

Seelos, F.P., Morgan, M.F., Taylor, H.W., Murchie, S.L., Humm, D.C., Seelos, K.D., Barnouin, O.S., Viviano, C.E., and the CRISM Team, 2012. CRISM Map Projected Targeted Reduced Data Records (MTRDRs) – High Level Analysis and Visualization Data Products, Planetary Data: A workshop for users and software developers, Flagstaff, AZ.

Seelos, F.P., Viviano-Beck, C.E., Morgan, M.F., Romeo, G., Aiello, J.J., Murchie, S.L., 2016. CRISM Hyperspectral Targeted Observation PDS Product Sets — TERs and MTRDRs, Lunar and Planetary Science Conference Abstracts, p. 1783.

Tanaka, K.L., 1986. The stratigraphy of Mars. Journal of Geophysical Research, 91, 139-158.

Tanaka, K.L., Skinner, J.A., Hare, T.M., 2005. Geologic map of the northern plains of Mars, U.S. Geological Survey Sci. Inv. Map 28888.

Tirsch, D., Jaumann, R., Pacifici, A., Poulet, F., 2011. Dark aeolian sediments in Martian craters: Composition and sources. Journal of Geophysical Research (Planets), 116, doi: 10.1029/2009je003562.

Tirsch, D., Craddock, R.A., Platz, T., Maturilli, A., Helbert, J., Jaumann, R., 2012. Spectral and petrologic analyses of basaltic sands in Ka'u Desert (Hawaii) – implications for the dark dunes on Mars. Earth Surface Processes and Landforms, 37, 434-448, doi: 10.1002/esp.2266.

Tirsch, D., Jaumann, R., 2012. On the Sources of Dark Dune Sands on Mars, Third International Planetary Dunes Workshop: Remote Sensing and Data Analysis of Planetary Dunes. LPI Contributions 1673, Flagstaff, Arizona, USA, pp. 93-94.

Tirsch, D., Sowe, M., Kneissl, T., Goeritz, M., Jaumann, R., 2013. New Evidence for Local Dark Aeolian Sediment Sources, European Planetary Science Congress 2013, p. 977.

Tirsch, D., Bishop, J.L., Voigt, J., Tornabene, L.L., Erkeling, G., Hiesinger, H., Jaumann, R., 2015. Diverse Morphology and Mineralogy of Aqueous Outcrops at Libya Montes, Mars, Lunar and Planetary Science Conference, p. 1738.

Tirsch, D., Erkeling, G., Bishop, J.L., Tornabene, L.L., Hiesinger, H., Jaumann, R., 2016. Lacustrine Mineral Deposits and their Geologic Context at Bradbury Crater on Mars, EGU General Assembly Conference Abstracts, p. 7069.

Tornabene, L.L., Moersch, J.E., McSween, H.Y., Hamilton, V.E., Piatek, J.L., Christensen, P.R., 2008. Surface and crater-exposed lithologic units of the Isidis Basin as mapped by coanalysis of THEMIS and TES derived data products. Journal of Geophysical Research (Planets), 113, 10001, doi: 10.1029/2007JE002988.

Tornabene, L.L., Osinski, G.R., McEwen, A.S., Wray, J.J., Craig, M.A., Sapers, H.M., Christensen, P.R., 2013. An impact origin for hydrated silicates on Mars: A synthesis. Journal of Geophysical Research: Planets, 118, 994-1012, doi: 10.1002/jgre.20082.

USGS, 2016. U.S.G.S. Planetary GIS Web Server - PIGWAD: Planetary Interactive G.I.S.-on-the-Web Analyzable Database. https://webgis.wr.usgs.gov/pigwad/down/mars_dl.htm.

Viennet, J.C., Bultel, B., Riu, L., Werner, S.C., 2017. Dioctahedral Phyllosilicates Versus Zeolites and Carbonates Versus Zeolites Competitions as Constraints to Understanding Early Mars Alteration Conditions. Journal of Geophysical Research: Planets, 122, 2328-2343, doi: 10.1002/2017JE005343.

Vihma, T., Tuovinen, E., Savijärvi, H., 2011. Interaction of katabatic winds and near-surface temperatures in the Antarctic. Journal of Geophysical Research: Atmospheres, 116, doi: 10.1029/2010JD014917.

Viviano-Beck, C.E., Seelos, F.P., Murchie, S.L., Kahn, E.G., Seelos, K.D., Taylor, H.W., Taylor, K., Ehlmann, B.L., Wisemann, S.M., Mustard, J.F., Morgan, M.F., 2014. Revised CRISM spectral parameters and summary products based on the currently detected mineral diversity on Mars. Journal of Geophysical Research (Planets), 119, 1403-1431, doi: 10.1002/2014JE004627.

Viviano-Beck, C.E., Murchie, S.L., Beck, A.W., Dohm, J.M., 2017. Compositional and structural constraints on the geologic history of eastern Tharsis Rise, Mars. Icarus, 284, 43-58, doi: 10.1016/j.icarus.2016.09.005.

Viviano, C.E., Moersch, J.E., McSween, H.Y., 2013. Implications for early hydrothermal environments on Mars through the spectral evidence for carbonation and chloritization reactions in the Nili Fossae region. Journal of Geophysical Research: Planets, 118, 1858-1872, doi: 10.1002/jgre.20141.

Werner, S.C., 2005. Major aspects of the chronostratigraphy and geologic evolutionary history of Mars, PhD, Freie Universität Berlin.

Werner, S.C., 2009. The global martian volcanic evolutionary history. Icarus, 201, 44-68, 10.1016/j.icarus.2008.12.019.

Werner, S.C., Tanaka, K.L., 2011. Redefinition of the crater-density and absolute-age boundaries for the chronostratigraphic system of Mars. Icarus, 215, 603-607, https://doi.org/10.1016/j.icarus.2011.07.024.

Williams, R.M.E., Irwin, R.P., Zimbelman, J.R., 2009. Evaluation of paleohydrologic models for terrestrial inverted channels: Implications for application to martian sinuous ridges. Geomorphology, 107, 300-315, doi: 10.1016/j.geomorph.2008.12.015.

Wray, J.J., Ehlmann, B.L., Squyres, S.W., Mustard, J.F., Kirk, R.L., 2008. Compositional stratigraphy of clay-bearing layered deposits at Mawrth Vallis, Mars. Geophysical Research Letters, 35, doi: 10.1029/2008GL034385.

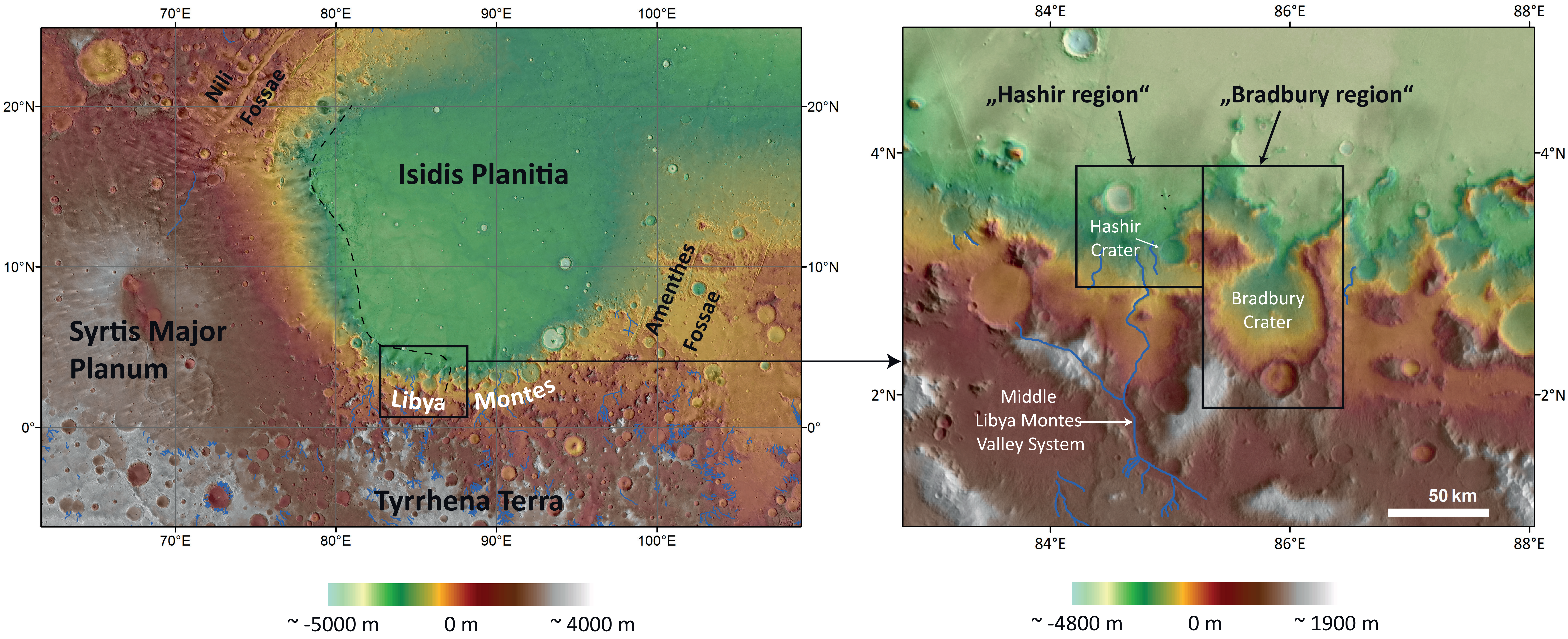

70°E
80°E
90°E
100°E
20°N
10°N
0°
Nili
Fossae
Isidis Planitia
Syrtis Major
Planum
Amenthes
Fossae
Libya
Montes
Tyrrhena Terra
~ -5000 m
0 m
~ 4000 m
84°E
86°E
88°E
4°N
2°N
„Hashir region“
„Bradbury region“
Hashir
Crater
Bradbury
Crater
Middle
Libya Montes
Valley System
50 km
~ -4800 m
0 m
~ 1900 m

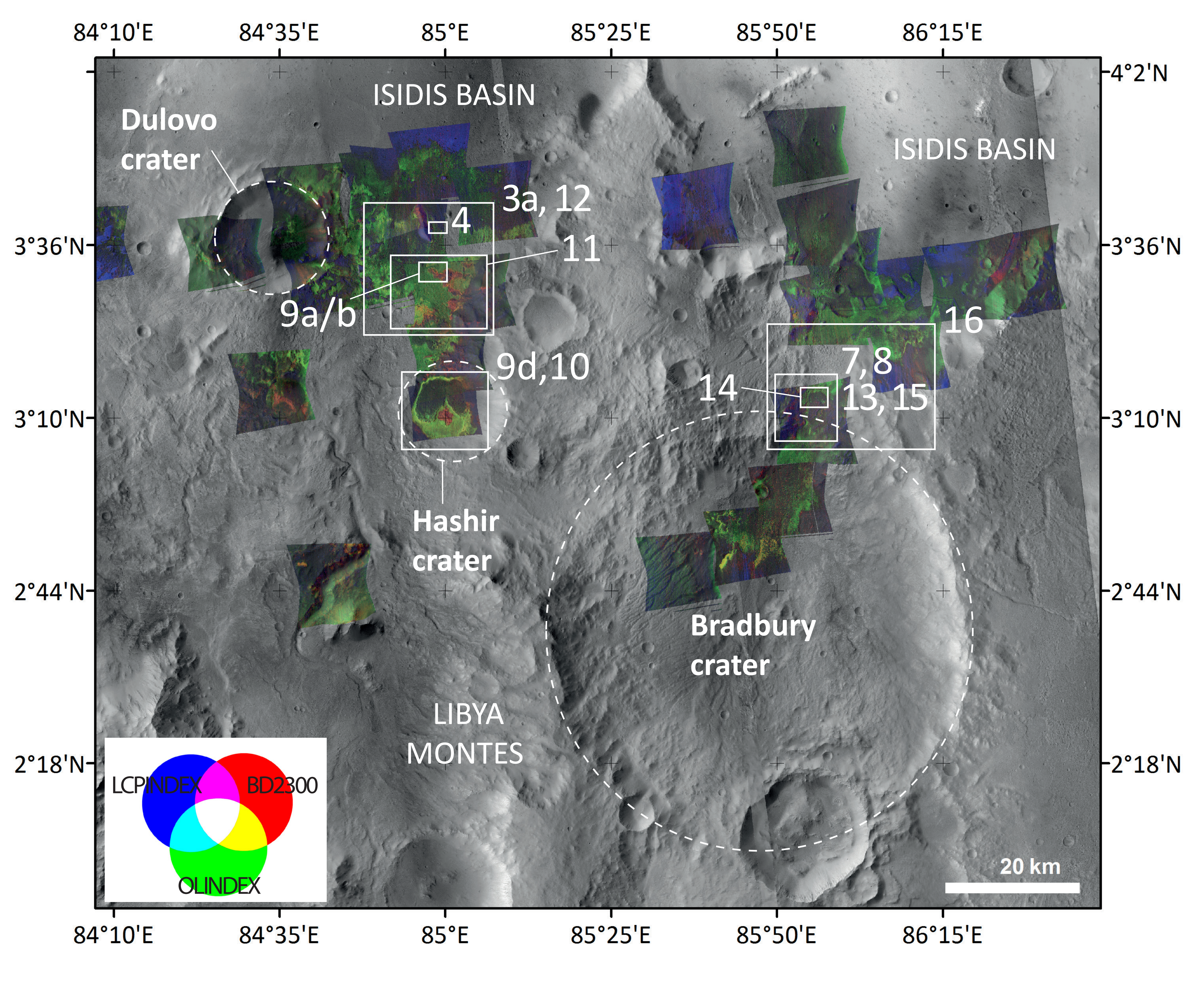
84°10'E
84°35'E
85°E
85°25'E
85°50'E
86°15'E
4°2'N
3°36'N
3°10'N
2°44'N
2°18'N
ISIDIS BASIN
Dulovo crater
ISIDIS BASIN
3a, 12
4
11
9a/b
16
7, 8
9d,10
14
13, 15
Hashir crater
Bradbury crater
LIBYA MONTES
LCPINDEX
BD2300
OLINDEX
20 km

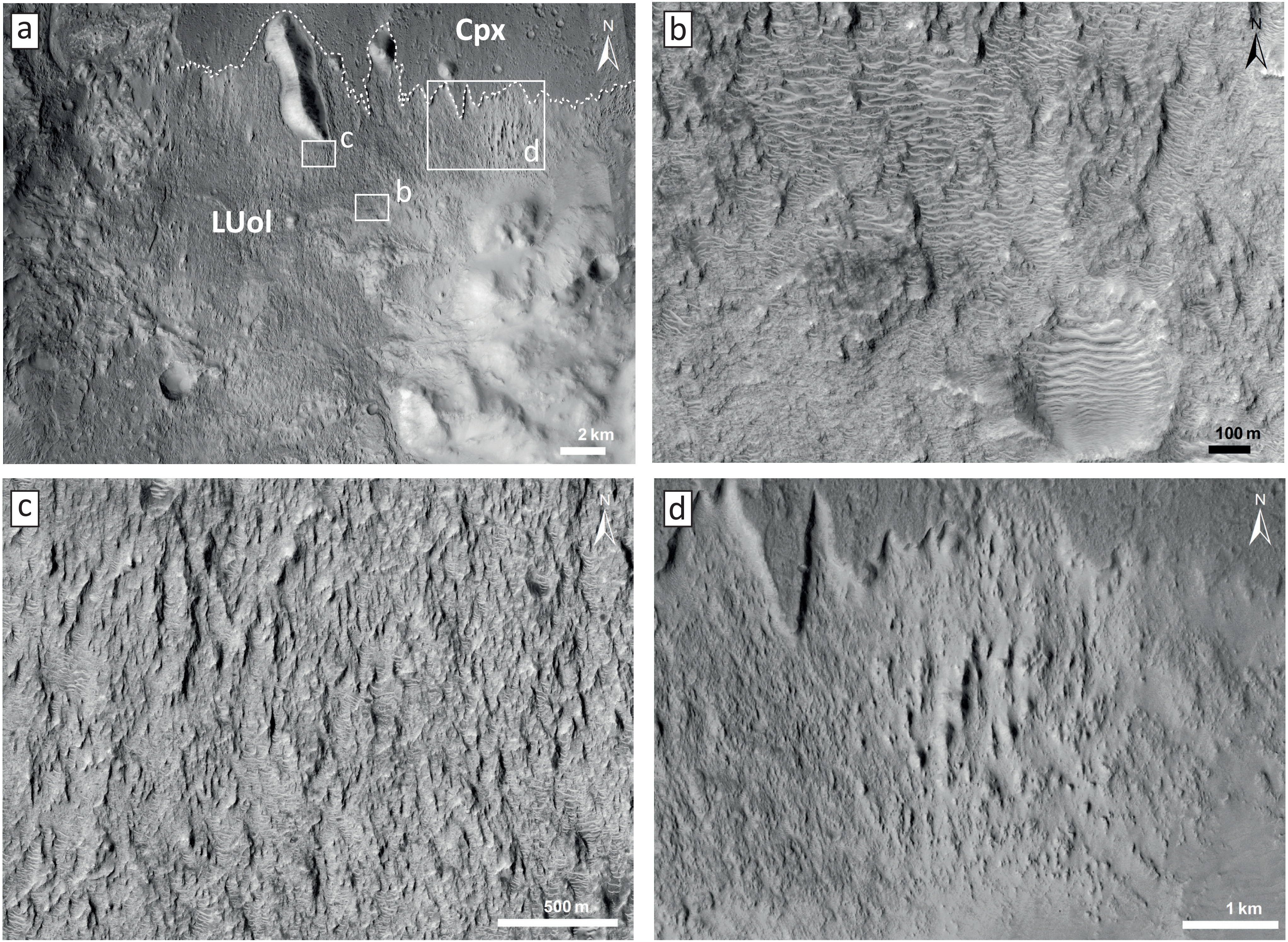
a
Cpx
N
c
d
b
LUol
2 km
b
N
100 m
c
N
500 m
d
N
1 km

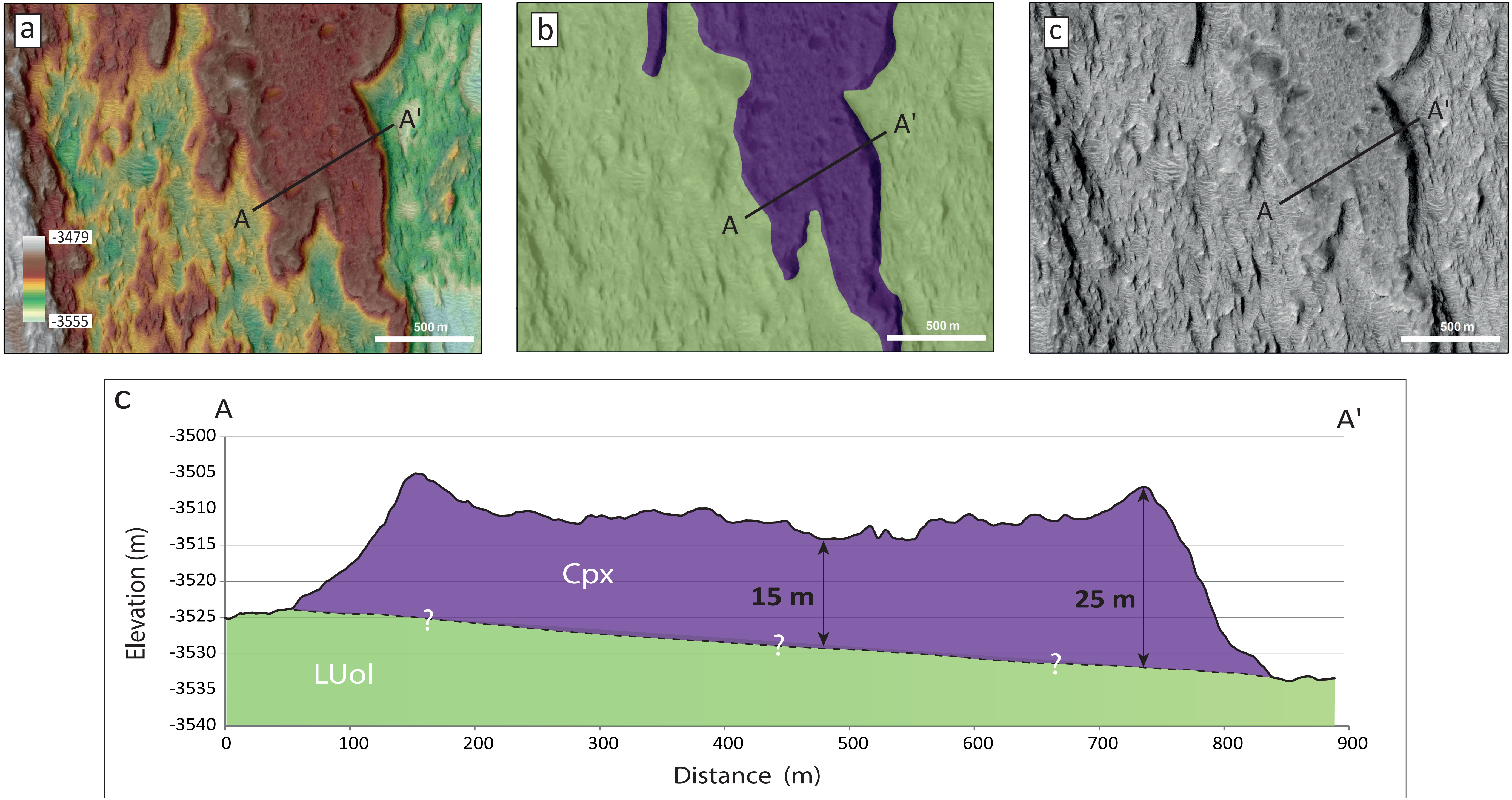

a
A'
A
-3479
-3555
500 m
b
A'
A
500 m
c
A'
A
500 m
c
A
A'
Elevation (m)
-3500
-3505
-3510
-3515
-3520
-3525
-3530
-3535
-3540
Cpx
LUol
15 m
25 m
?
?
?
0
100
200
300
400
500
600
700
800
900
Distance (m)

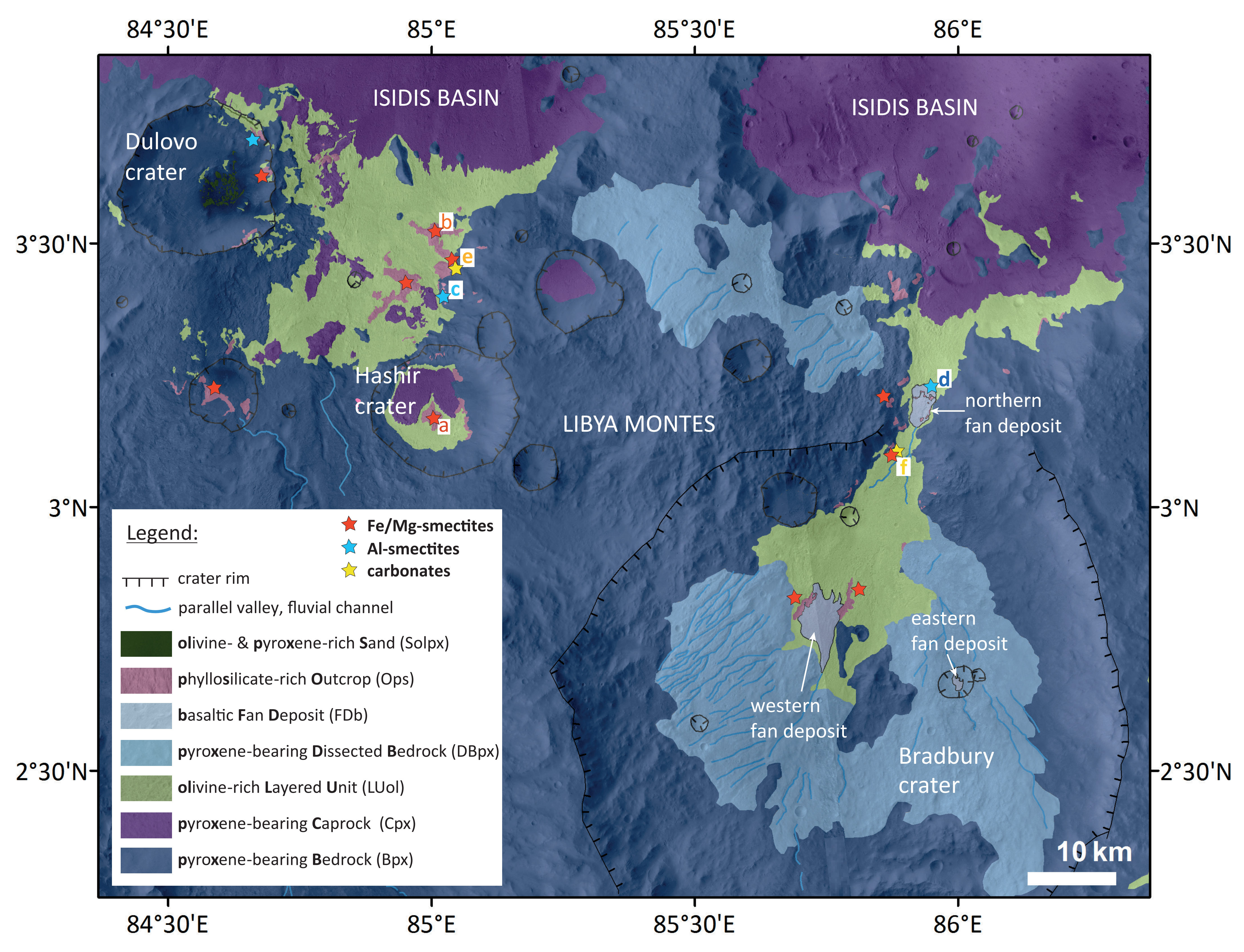
84°30'E
85°E
85°30'E
86°E
3°30'N
3°N
2°30'N
ISIDIS BASIN
ISIDIS BASIN
Dulovo
crater
Hashir
crater
LIBYA MONTES
northern
fan deposit
eastern
fan deposit
western
fan deposit
Bradbury
crater
a
b
c
d
e
f
10 km
Legend:
Fe/Mg-smectites
Al-smectites
carbonates
crater rim
parallel valley, fluvial channel
olivine- & pyroxene-rich Sand (Solpx)
phyllosilicate-rich Outcrop (Ops)
basaltic Fan Deposit (FDb)
pyroxene-bearing Dissected Bedrock (DBpx)
olivine-rich Layered Unit (LUol)
pyroxene-bearing Caprock (Cpx)
pyroxene-bearing Bedrock (Bpx)

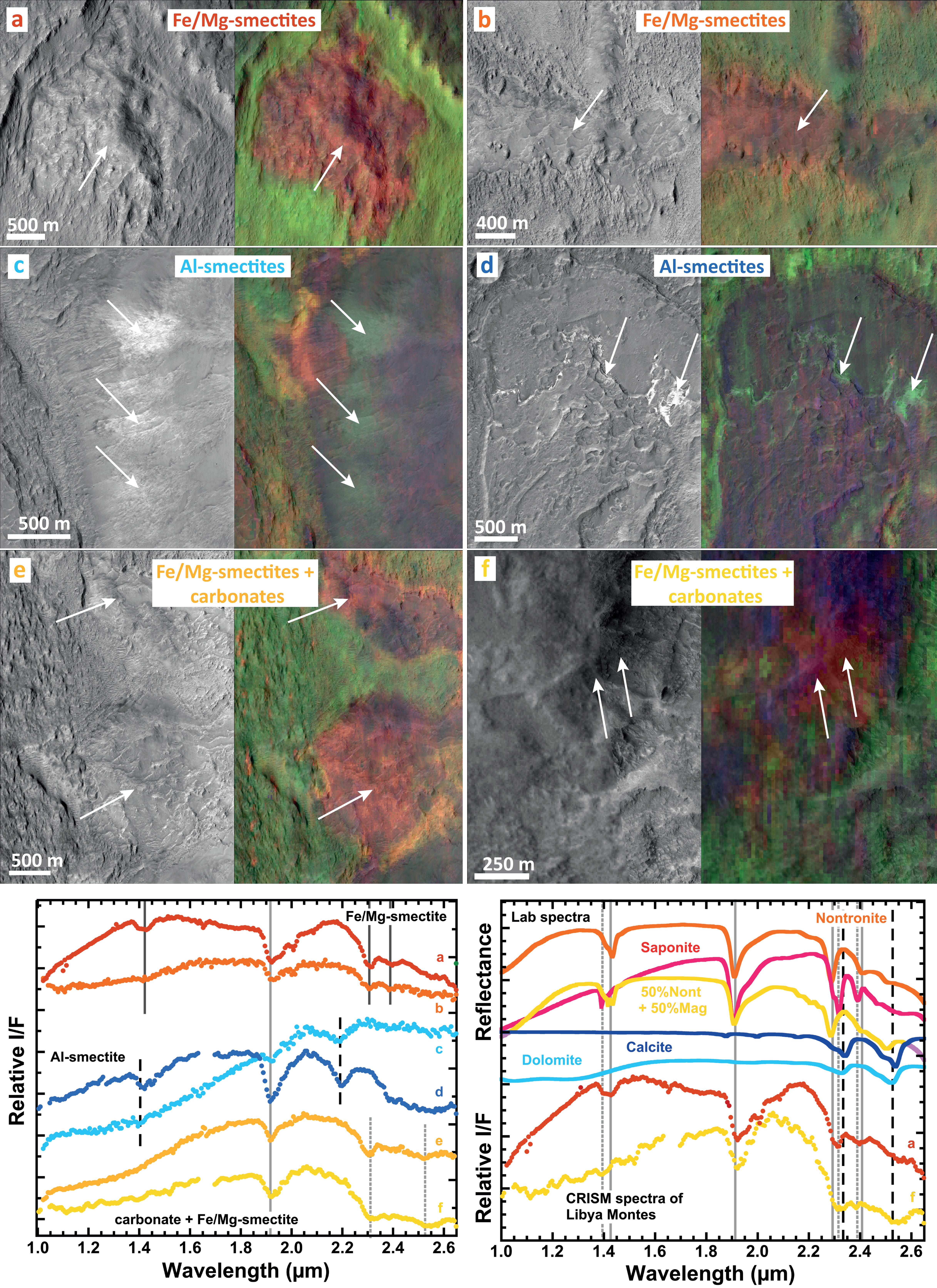

a
Fe/Mg-smectites
500 m
b
Fe/Mg-smectites
400 m
c
Al-smectites
500 m
d
Al-smectites
500 m
e
Fe/Mg-smectites + carbonates
500 m
f
Fe/Mg-smectites + carbonates
250 m
Fe/Mg-smectite
Al-smectite
carbonate + Fe/Mg-smectite
Relative I/F
Wavelength (µm)
Lab spectra
Nontronite
Saponite
50%Nont + 50%Mag
Calcite
Dolomite
CRISM spectra of Libya Montes
Reflectance
Relative I/F
Wavelength (µm)

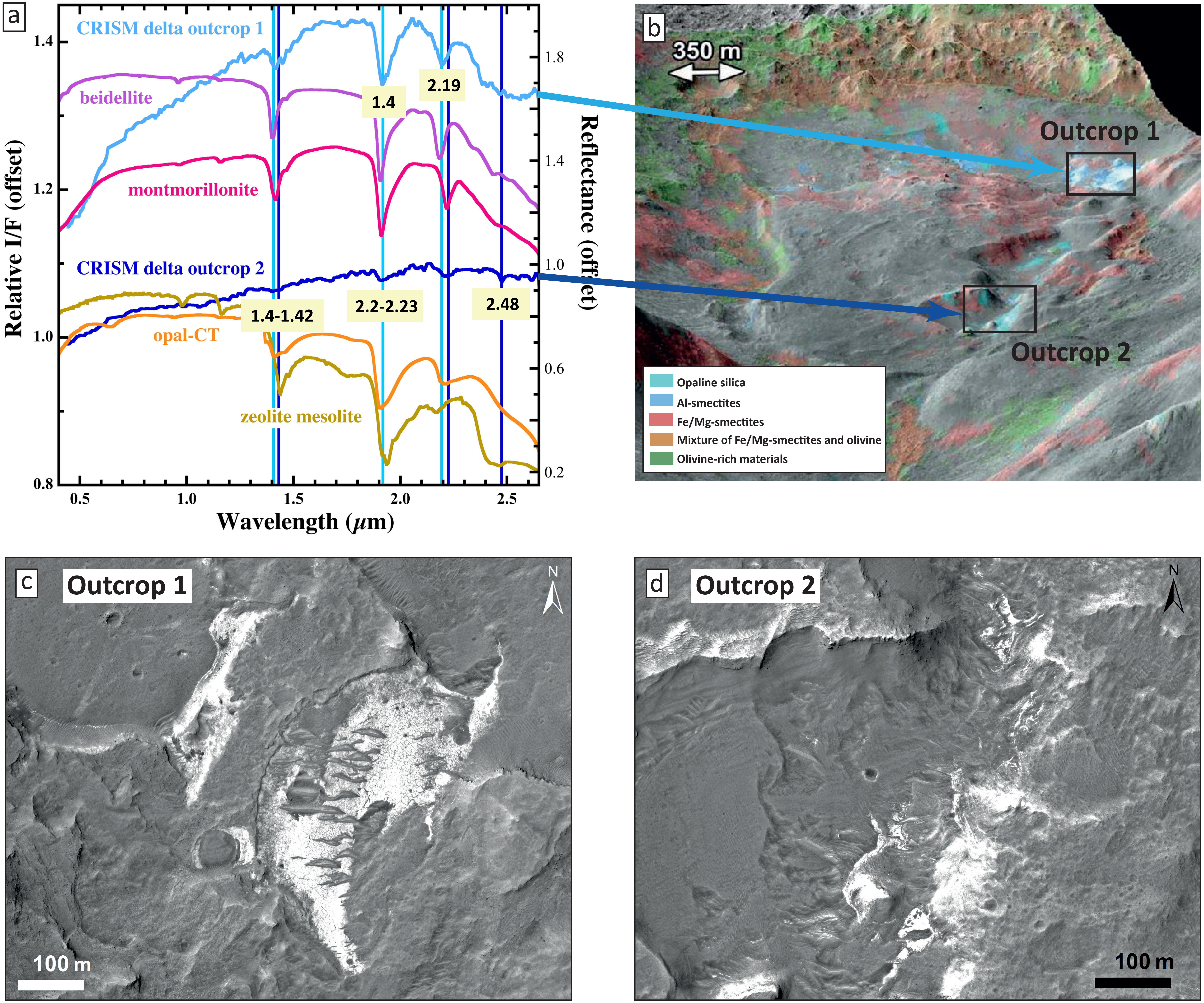
a
CRISM delta outcrop 1
beidellite
montmorillonite
CRISM delta outcrop 2
opal-CT
zeolite mesolite
1.4
2.19
1.4-1.42
2.2-2.23
2.48
Relative I/F (offset)
Reflectance (offset)
Wavelength (μm)
b
350 m
Outcrop 1
Outcrop 2
Opaline silica
Al-smectites
Fe/Mg-smectites
Mixture of Fe/Mg-smectites and olivine
Olivine-rich materials
c
Outcrop 1
N
100 m
d
Outcrop 2
N
100 m

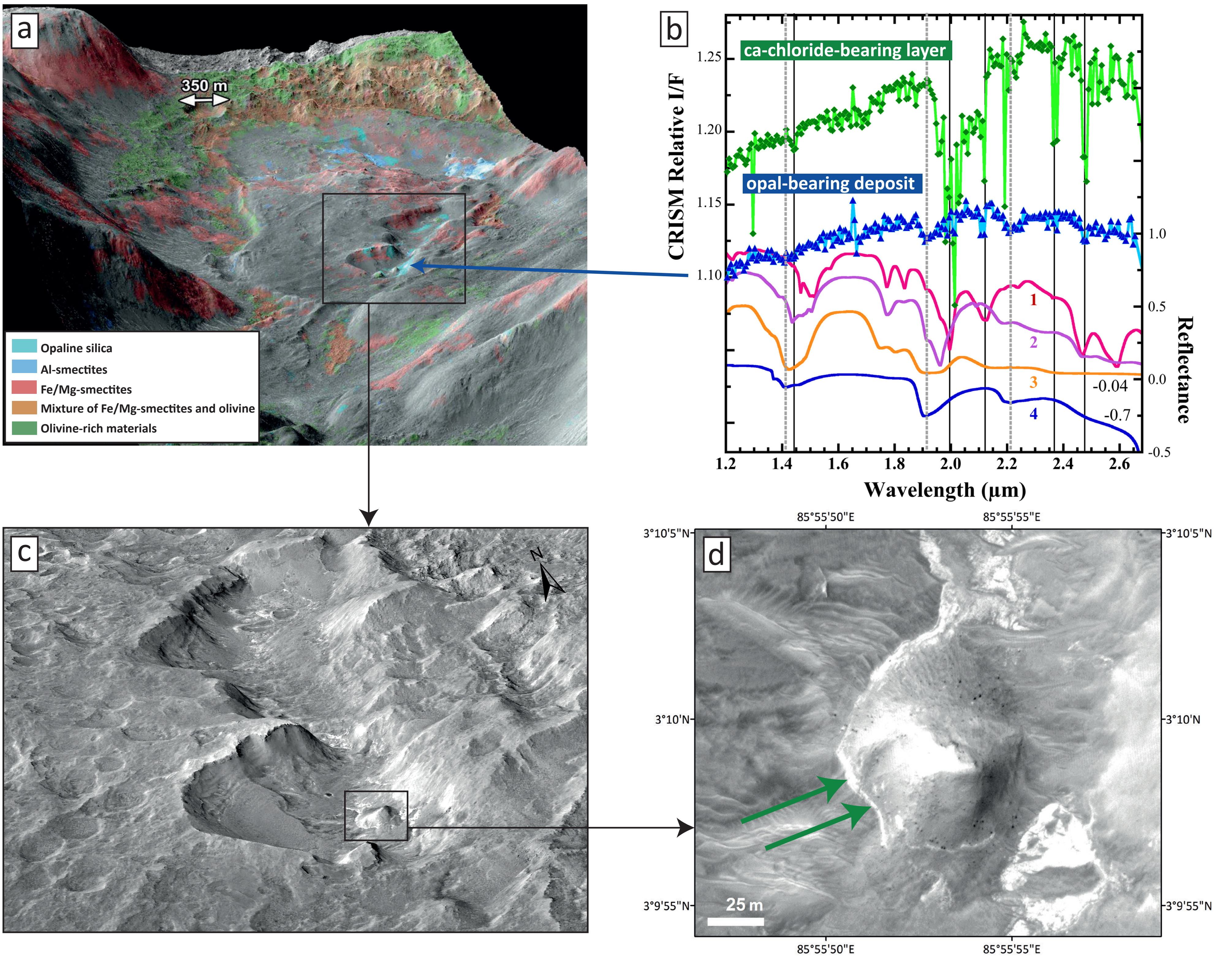

a
350 m
Opaline silica
Al-smectites
Fe/Mg-smectites
Mixture of Fe/Mg-smectites and olivine
Olivine-rich materials
b
ca-chloride-bearing layer
opal-bearing deposit
CRISM Relative I/F
Reflectance
Wavelength (μm)
1
2
3
4
-0.04
-0.7
c
N
d
85°55'50"E
85°55'55"E
3°10'5"N
3°10'N
3°9'55"N
25 m

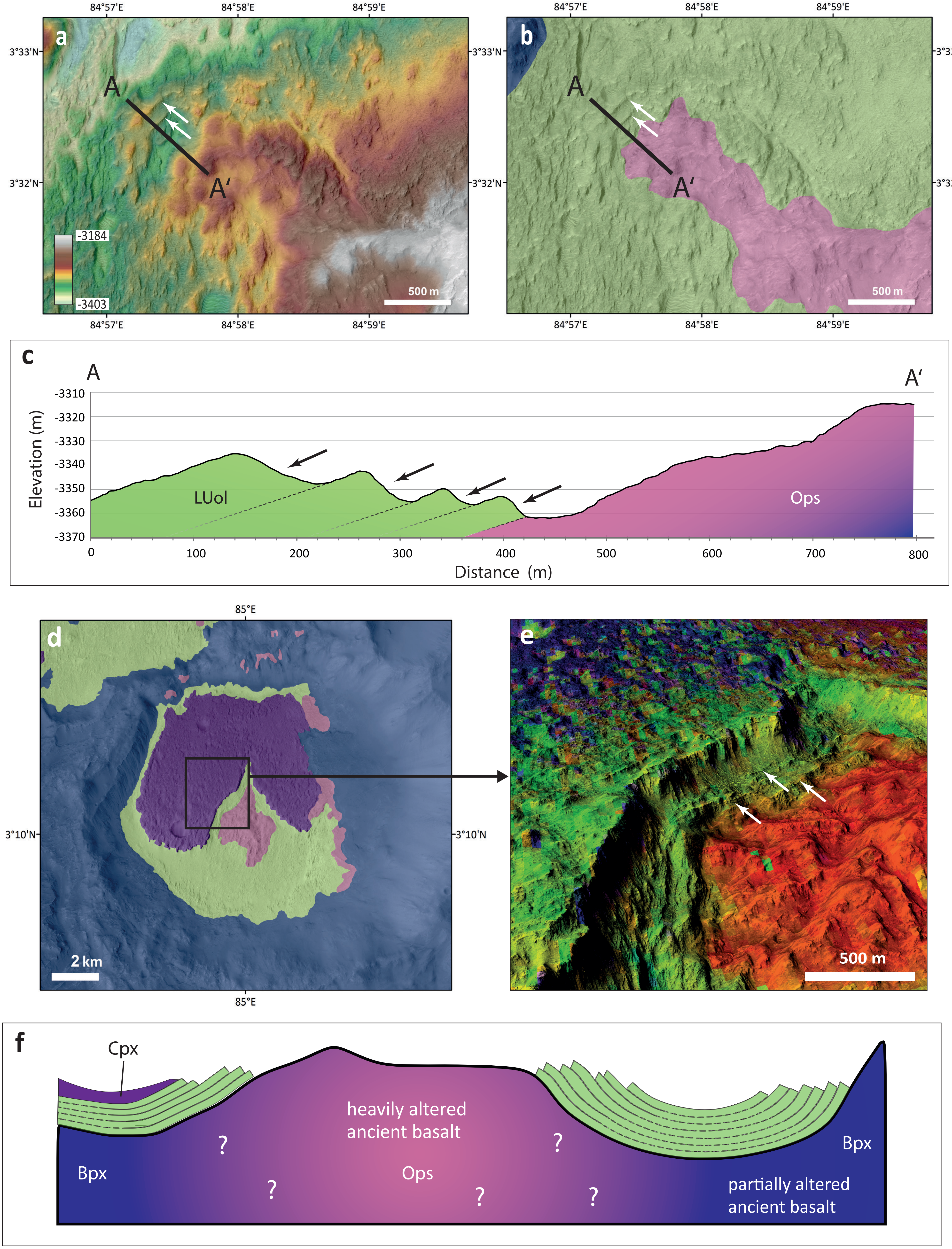
a
b
c
d
e
f
84°57'E
84°58'E
84°59'E
3°33'N
3°32'N
A
A′
-3184
-3403
500 m
Elevation (m)
Distance (m)
LUol
Ops
85°E
3°10'N
2 km
Cpx
heavily altered
ancient basalt
Bpx
partially altered
ancient basalt

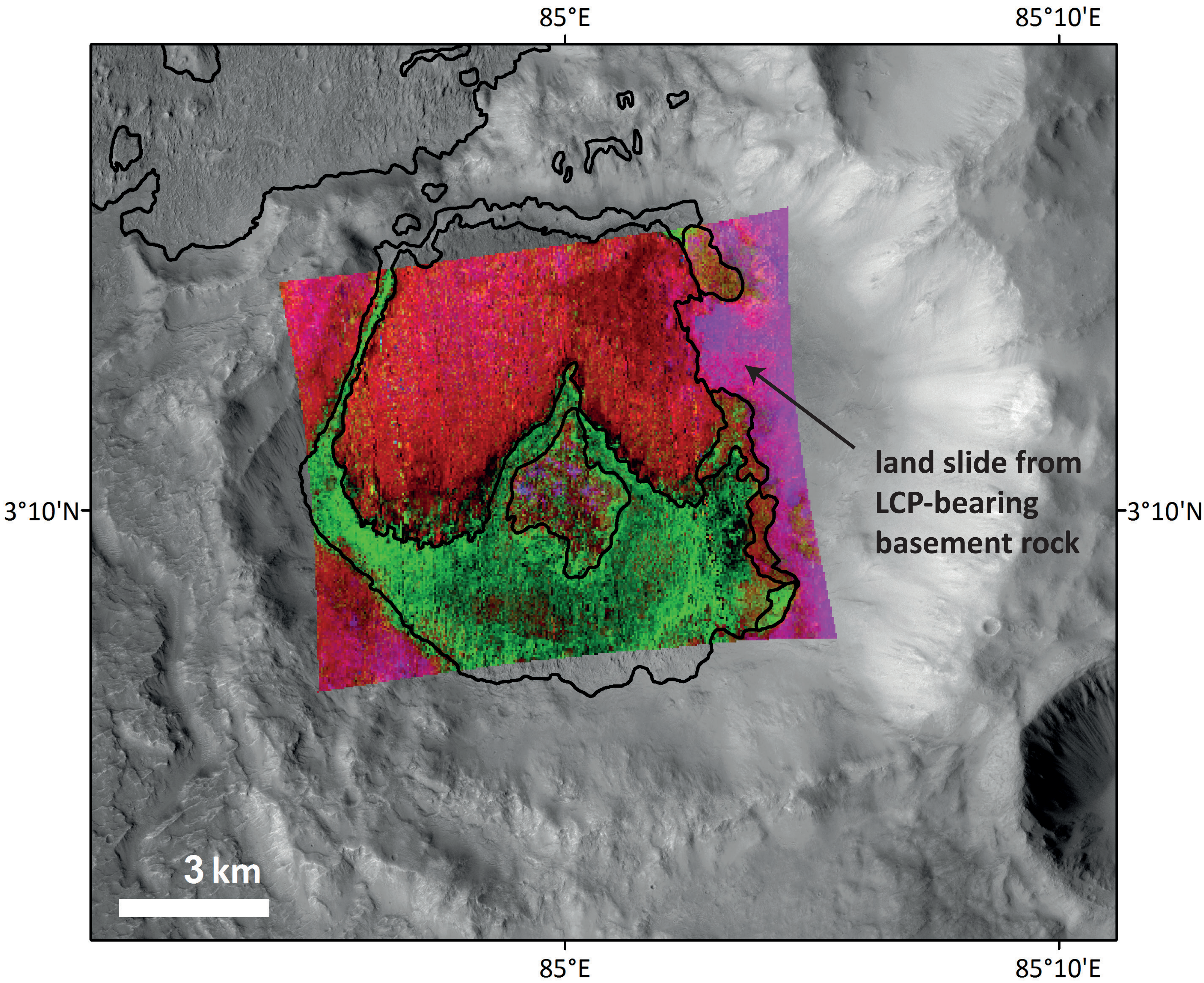
85°E
85°10'E
3°10'N
3°10'N
land slide from
LCP-bearing
basement rock
3 km
85°E
85°10'E

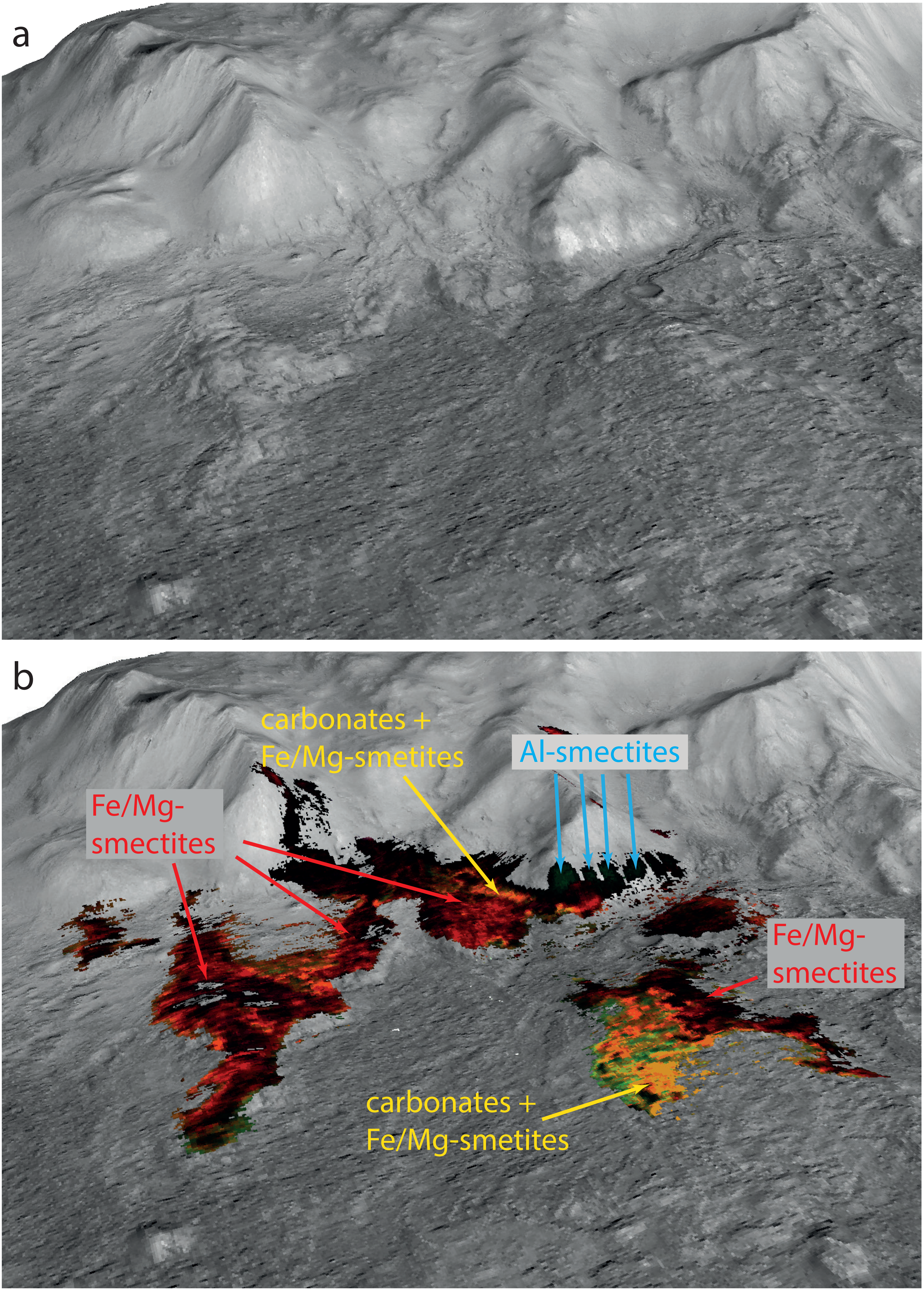
a
b
carbonates +
Fe/Mg-smetites
Al-smectites
Fe/Mg-
smectites
Fe/Mg-
smectites
carbonates +
Fe/Mg-smetites

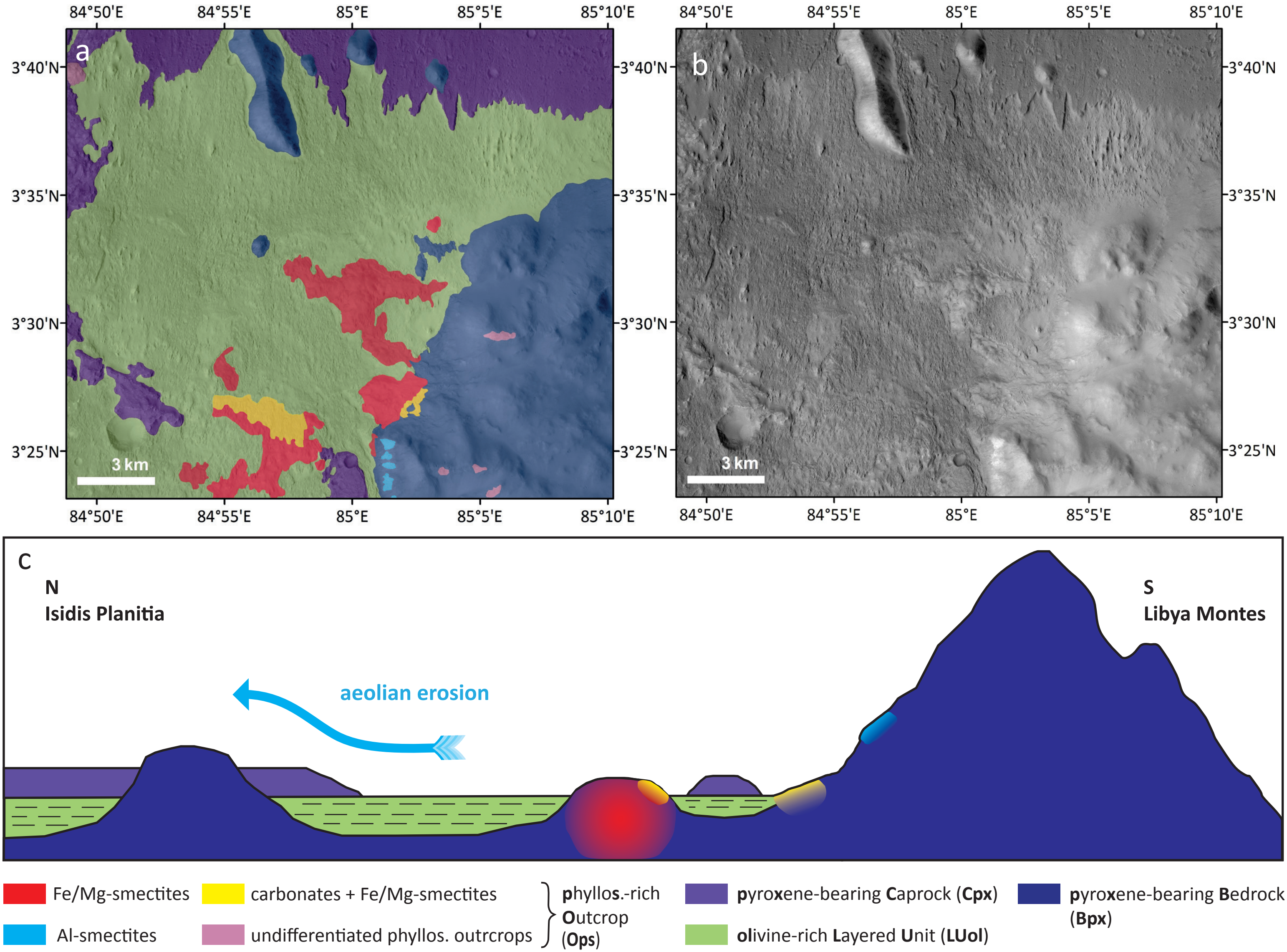

a
b
c
84°50'E
84°55'E
85°E
85°5'E
85°10'E
3°40'N
3°35'N
3°30'N
3°25'N
3 km
N
Isidis Planitia
S
Libya Montes
aeolian erosion
Fe/Mg-smectites
carbonates + Fe/Mg-smectites
Al-smectites
undifferentiated phyllos. outrcrops
phyllos.-rich Outcrop (Ops)
pyroxene-bearing Caprock (Cpx)
olivine-rich Layered Unit (LUol)
pyroxene-bearing Bedrock (Bpx)

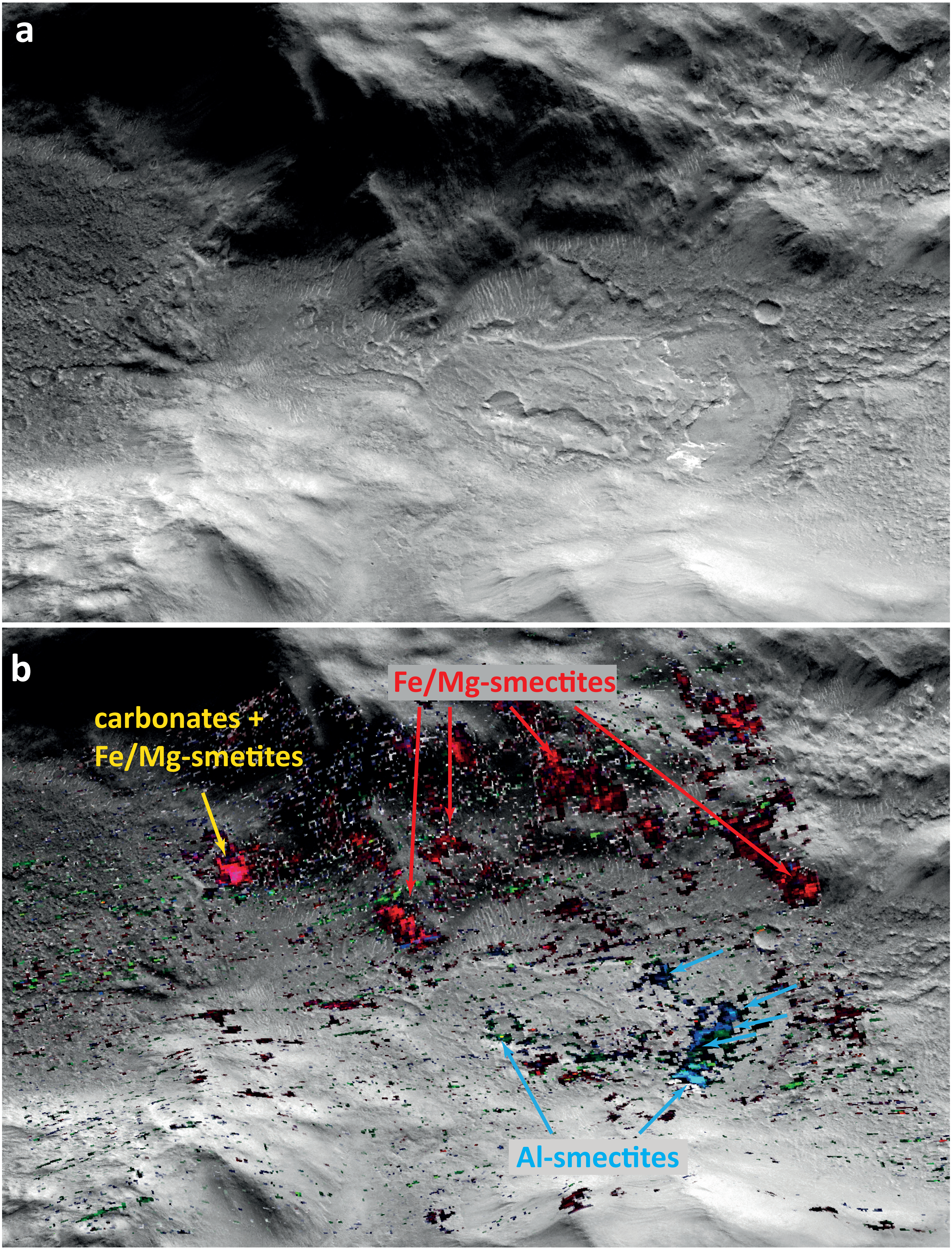
a
b
carbonates +
Fe/Mg-smetites
Fe/Mg-smectites
Al-smectites

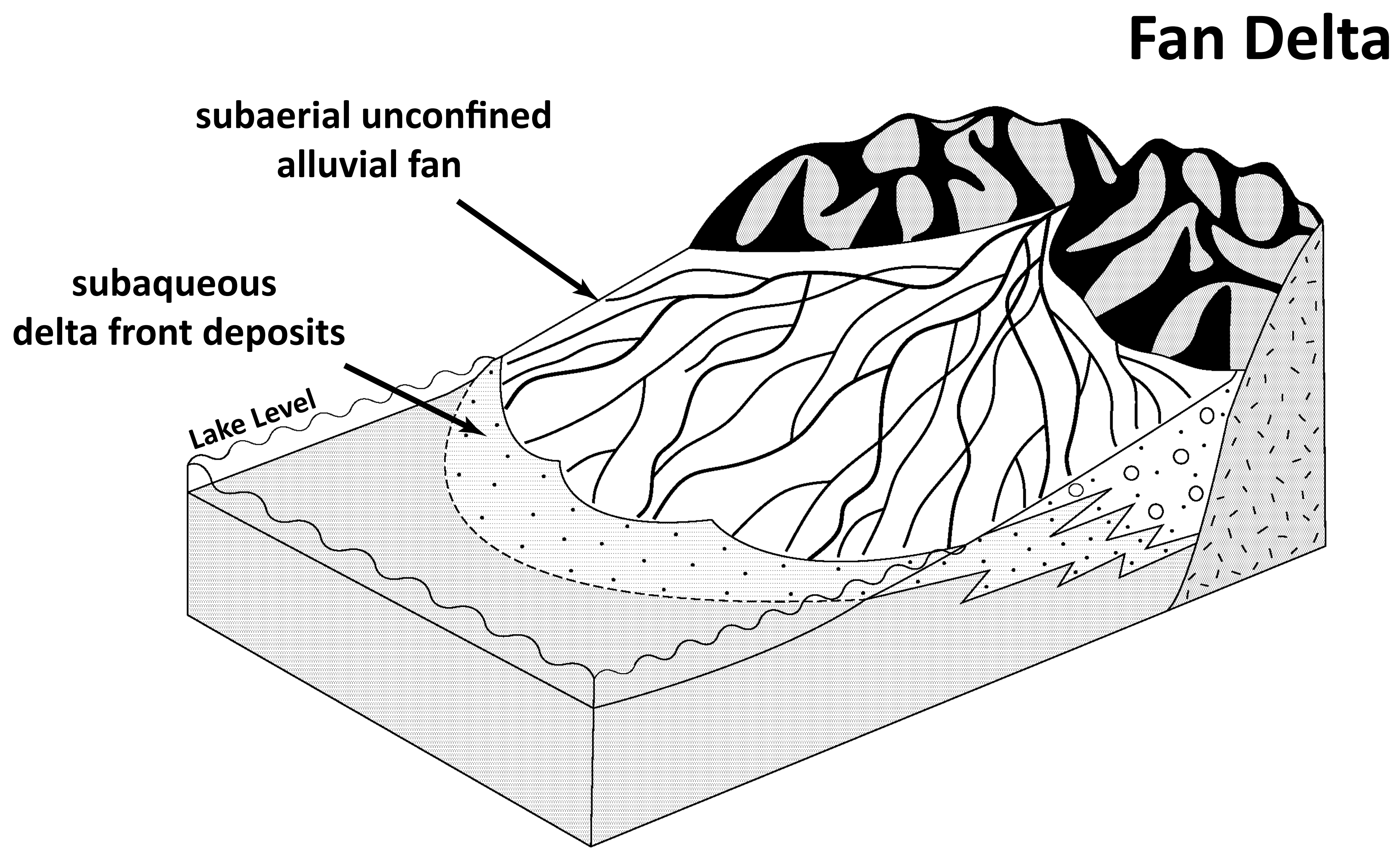
Fan Delta
subaerial unconfined alluvial fan
subaqueous delta front deposits
Lake Level

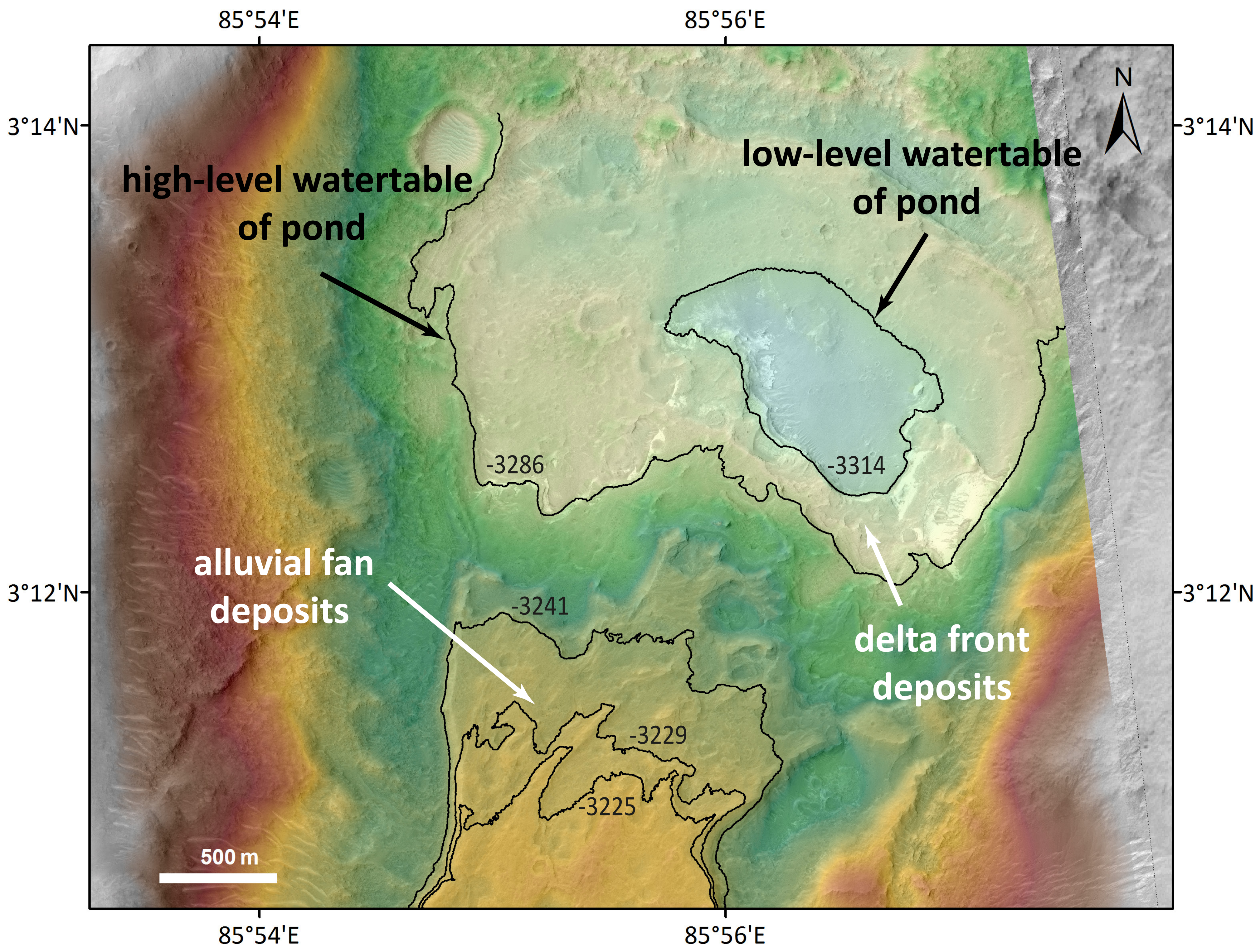
85°54'E
85°56'E
3°14'N
3°12'N
N
high-level watertable of pond
low-level watertable of pond
-3286
-3314
alluvial fan deposits
-3241
delta front deposits
-3229
-3225
500 m

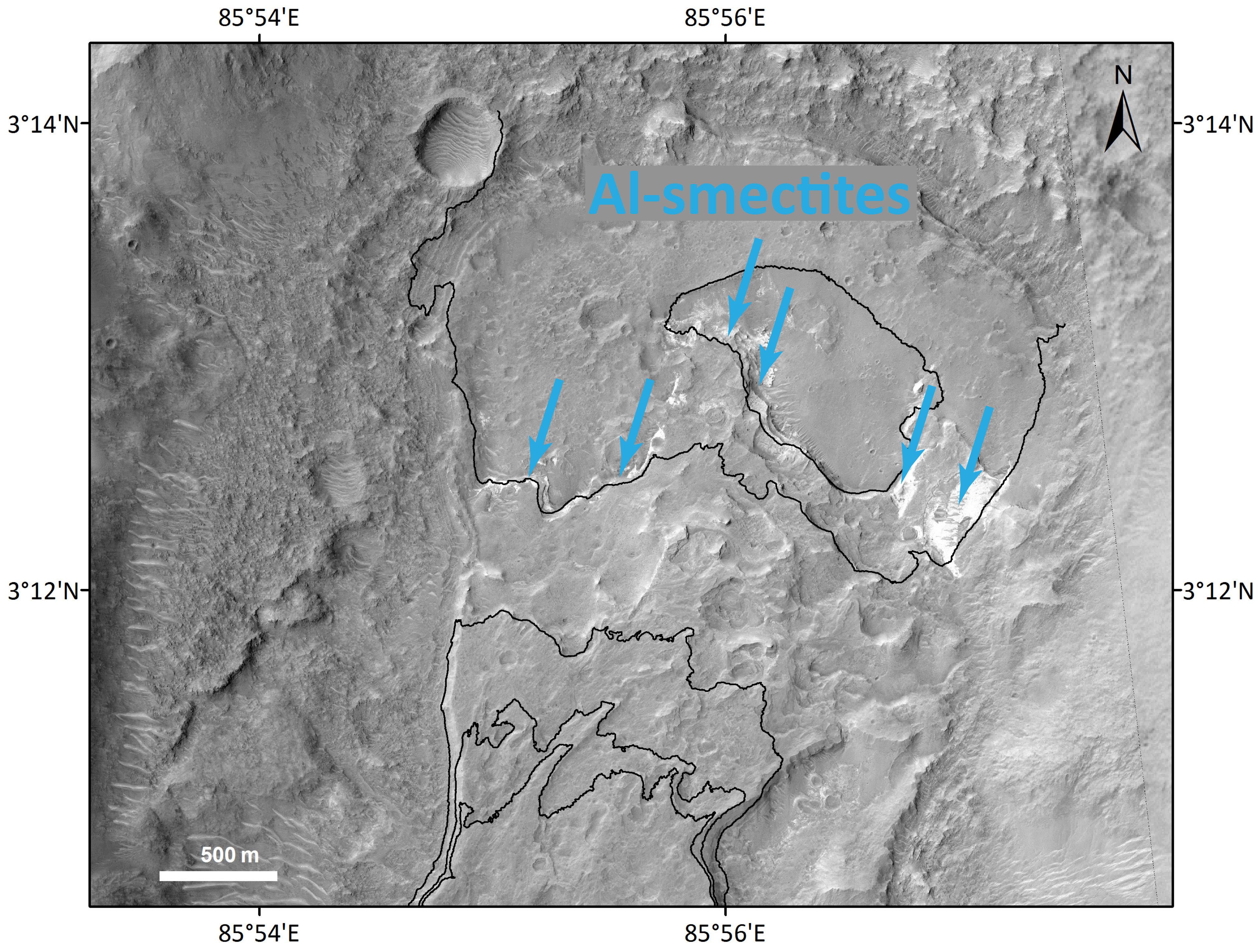
85°54'E
85°56'E
3°14'N
3°12'N
N
Al-smectites
500 m

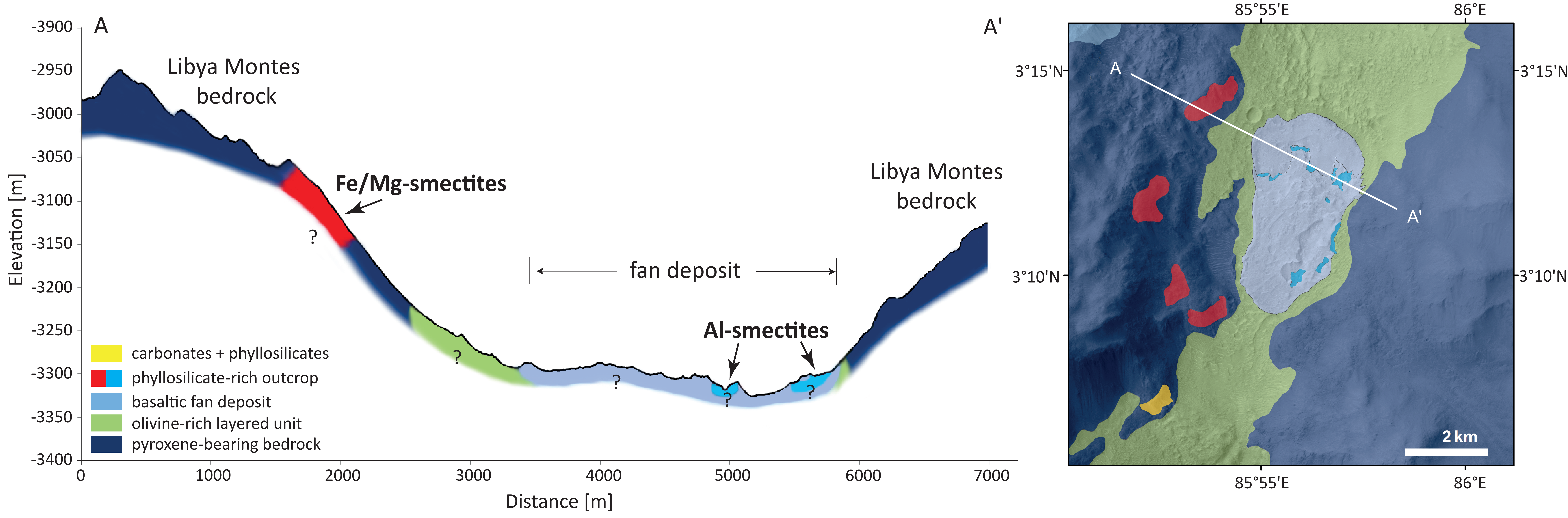

A
A'
Libya Montes bedrock
Fe/Mg-smectites
fan deposit
Al-smectites
Libya Montes bedrock
carbonates + phyllosilicates
phyllosilicate-rich outcrop
basaltic fan deposit
olivine-rich layered unit
pyroxene-bearing bedrock
Elevation [m]
Distance [m]
-3900
-2950
-3000
-3050
-3100
-3150
-3200
-3250
-3300
-3350
-3400
0
1000
2000
3000
4000
5000
6000
7000
85°55'E
86°E
3°15'N
3°10'N
2 km

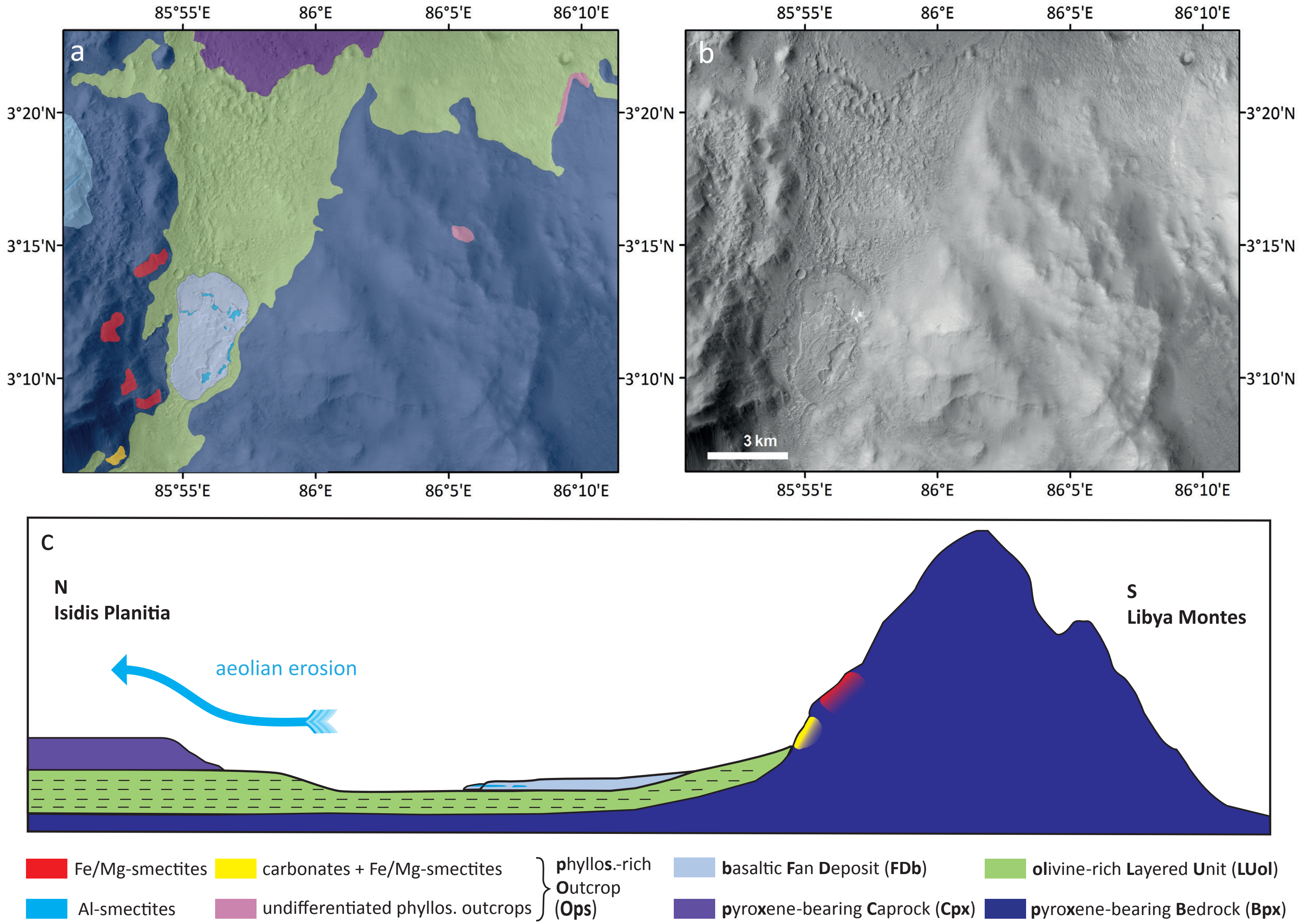
a
b
c
85°55'E
86°E
86°5'E
86°10'E
3°20'N
3°15'N
3°10'N
3 km
N
Isidis Planitia
S
Libya Montes
aeolian erosion
Fe/Mg-smectites
carbonates + Fe/Mg-smectites
Al-smectites
undifferentiated phyllos. outcrops
phyllos.-rich Outcrop (Ops)
basaltic Fan Deposit (FDb)
pyroxene-bearing Caprock (Cpx)
olivine-rich Layered Unit (LUol)
pyroxene-bearing Bedrock (Bpx)

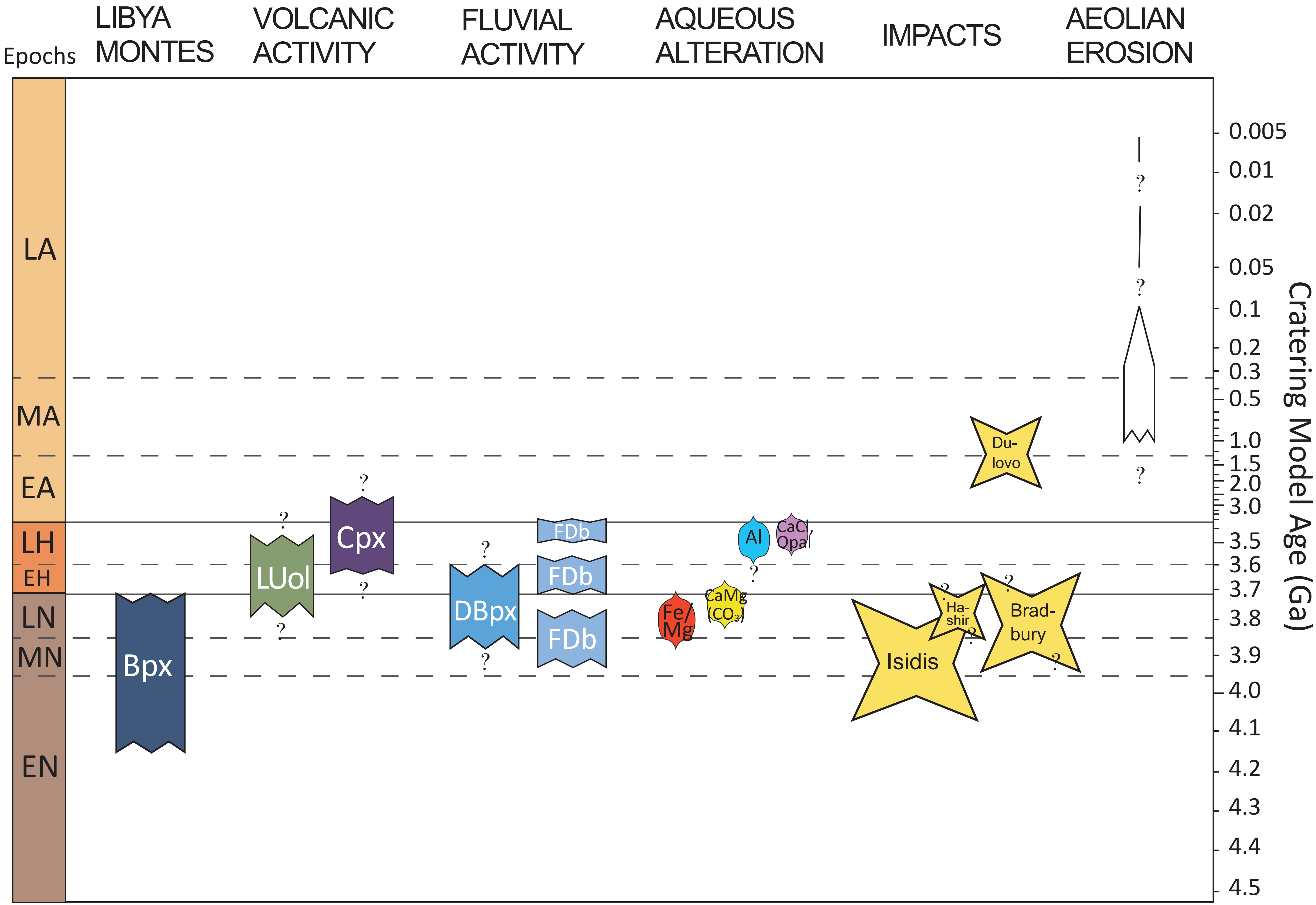

Epochs
LIBYA MONTES
VOLCANIC ACTIVITY
FLUVIAL ACTIVITY
AQUEOUS ALTERATION
IMPACTS
AEOLIAN EROSION
LA
MA
EA
LH
EH
LN
MN
EN
Bpx
LUol
Cpx
DBpx
FDb
FDb
FDb
Al
CaCl, Opal
Fe/Mg
CaMg (CO3)
Du-lovo
Ha-shir
Brad-bury
Isidis
0.005
0.01
0.02
0.05
0.1
0.2
0.3
0.5
1.0
1.5
2.0
3.0
3.5
3.6
3.7
3.8
3.9
4.0
4.1
4.2
4.3
4.4
4.5
Cratering Model Age (Ga)

Sensor	Image ID	Image type	Acquisition Date	Latitude	Longitude
HRSC	h0047_0000	nd + dtm	2004-01-24	-10.0826	81.9993
HRSC	h0922_0000	nd + dtm	2004-10-07	2.16756	81.3282
HRSC	h0933_0000	nd + dtm	2004-10-11	2.67795	80.2944
HRSC	h0944_0009	nd + dtm	2004-10-14	0.786927	79.2526
HRSC	h1226_0000	nd + dtm	2005-01-01	6.71835	89.681
HRSC	h2162_0002	nd + dtm	2005-09-20	2.02247	85.8429
HRSC	h2206_0002	nd + dtm	2005-10-02	1.69022	82.7402
HRSC	h3285_0000	nd + dtm	2006-07-31	-0.072572	84.4921
HRSC	h5072_0000	nd + dtm	2007-15-14	10.6031	85.3749
HRSC	h5144_0000	nd + dtm	2008-01-03	11.9235	84.7089
HRSC	h5162_0000	nd + dtm	2008-01-08	12.1713	83.7834
HRSC	h5180_0000	nd + dtm	2008-13-01	12.2356	82.849
HRSC	h7396_0001	nd + dtm	2009-10-08	-1.01902	87.7522
HRSC	h7421_0001	nd + dtm	2009-10-15	-856198	86.2331
HRSC	ha460_0000	nd + dtm	2012-03-17	-7.34795	89.5928
CRISM	FRT00003B63	S + L	2007-002	3.589735	84.11816
CRISM	FRT00007F47	S + L	2007-272	3.71798	84.89209
CRISM	FRT000085D7	S + L	2007-295	3.340555	86.168895
CRISM	FRT00008CA3	S + L	2007-351	3.51597	86.317135
CRISM	FRT00009657	S + L	2008-013	3.470215	86.118605
CRISM	FRT00009A01	S + L	2008-025	3.5397	86.455995
CRISM	FRT0000A542	S + L	2008-069	3.74187	84.85148
CRISM	FRT0000A819	S + L	2008-108	3.45631	85.013215
CRISM	FRT0000B0CB	S + L	2008-164	3.160725	85.935855
CRISM	FRT0000BC7D	S + L	2008-209	3.704	85.129355
CRISM	FRT0000CE72	S + L	2008-286	3.69723	84.65529
CRISM	FRT0001647D	S + L	2010-034	3.306055	85.01772
CRISM	FRT0001754F	S + L	2010-079	3.47304	85.074285
CRISM	FRT0001802B	S + L	2010-106	3.52736	84.701335
CRISM	FRT00018800	S + L	2010-123	3.227855	84.569695
CRISM	FRT00019568	S + L	2010-167	2.73913	84.71896
CRISM	FRT0001E2F2	S + L	2011-139	2.84276	85.767195
CRISM	FRT0001EB06	S + L	2011-172	3.57387	84.446425
CRISM	FRT0001ECEC	S + L	2011-183	2.77942	85.595785
CRISM	FRT0001FDD7	S + L	2011-239	3.455755	85.96124
CRISM	FRT00020397	S + L	2011-255	3.540045	86.009395
CRISM	FRT00020BC6	S + L	2011-288	3.697325	85.63859
CRISM	FRT00021CD0	S + L	2011-343	3.658455	85.9515

CRISM	FRT000235CA	S + L	2011-061	3.805415	84.974545
CRISM	FRT000240DF	S + L	2012-008	2.967615	85.87767
CRISM	FRT00024284	S + L	2012-094	3.541745	84.8743
CRISM	FRT0002459B	S + L	2012-105	3.84613	85.91712
CRISM	FRT00024AE2	S + L	2012-121	3.612025	84.920365
CRISM	HRS000047D8 (TRR3 and MTRDR)	S + L	2007-058	3.187655	85.007905
CRISM	HRS00011AD0	S + L	2009-080	3.635415	85.333595
CRISM	HRS0001EC08	S + L	2011-178	3.628915	85.91098
CTX	B22_018368_1824_XN_02N275W		2010-06-27	2.48	84.75
CTX	G11_022548_1828_XN_02N274W		2011-05-19	2.84	85.76
CTX	G14_023682_1827_XN_02N274W		2011-08-15	2.79	85.91
CTX	P02_001833_1827_XN_02N275W		2006-12-17	2.77	84.46
CTX	P04_002545_1839_XI_03N274W		2007-02-10	3.95	85.40
CTX	P04_002756_1826_XI_02N275W		2007-02-27	2.60	85.07
CTX	P05_002822_1822_XI_02N275W		2007-03-04	2.40	85.07
CTX	P12_005802_1819_XN_01N273W		2007-10-22	1.99	86.33
CTX	P13_006158_1821_XN_02N273W		2007-11-19	2.16	86.48
CTX	P14_006580_1822_XN_02N275W		2007-12-22	2.26	84.39
CTX	P16_007226_1809_XN_00N274W		2008-02-10	0.90	85.69
CTX	P17_007727_1814_XN_01N273W		2008-03-20	1.53	86.12
CTX	P20_008874_1822_XN_02N276W		2008-06-17	2.25	84.09
CTX	P20_009019_1829_XN_02N275W		2008-06-29	2.98	84.70
HiRISE	DTEEC_002756_1830_002800_1830_A01	DTM		see input images	
HiRISE	DTEEC_007727_1830_008808_1830_A01	DTM		see input images	
HiRISE	DTEEC_016034_1835_017089_1835_A01	DTM		see input images	
HiRISE	DTEED_043264_1835_042763_1835_A01	DTM		see input images	
HiRISE	PSP_002822_1830	red + color	2007-03-04	2.9746	83.3671
HiRISE	ESP_017089_1835	red + color	2007-03-20	3.4124	84.6476
HiRISE	ESP_022337_1830	red + color	2011-05-03	2.8146	85.8892
HiRISE	ESP_022548_1830	red + color	2011-05-19	2.7989	85.5075
HiRISE	PSP_002756_1830	red + color	2007-02-27	3.2064	85.2318
HiRISE	PSP_007727_1830	red + color	2008-03-20	3.0933	85.4498
HIRSIE	ESP_016522_1835	red + color	2010-02-03	3.2208	84.3871
HIRISE	ESP_016034_1835	red + color	2009-12-27	3.7173	87.1385

Symbol	Unit Name	Description	Interpretation
Bpx	**p**yro**x**ene-bearing **B**edrock	sharp mountain ridges with high topography differences and steep and rugged slopes	high mountainous massif, remnants of Isidis impact rim
DBpx	**p**yro**x**ene-bearing **D**issected **B**edrock	surfaces that are dissected by narrow parallel valleys that are partially degraded and incise deeply into the rocks	fluvially eroded highland terrains; part of Bpx
LUol	**ol**ivine-rich **L**ayered **U**nit	strongly eroded, layered unit featuring grooves; superposed onto Bpx and below Cpx	volcanic origin; probably from Syrtis Major (lava flows or air fall deposits)
Cpx	**p**yro**x**ene-bearing **C**aprock	surface smoother than LUol but with numerous small craters; widespread capping unit superposing LUol, patchy to the south	volcanic origin; probably from later stages of Syrtis Major activity
FDb	**b**asaltic **F**an **D**eposit	sedimentary fan-shaped deposits at the Bradbury region	two alluvial fans and one fan delta
Ops	**p**hyllo**s**ilicate-rich **O**utcrop	Fe/Mg-smectites, Al-smectites and carbonates at various locations	aqueously altered basements rocks
Solpx	**ol**ivine- and **p**yro**x**ene-rich **S**and	sand piles on the floor of Dulovo crater and a dark linear feature cropping out at the crater wall; high olivine- and pyroxene signature	dark aeolian sediments accumulated as sand dunes and its local sediment source exposed at the crater wall